Characterization of Abrasive Wear by Mass Loss and Acoustic Emission using the Ball-on-Plate Testing

by

Haroldo Kawakami

A thesis submitted in partial fulfillment of the requirements for the degree of

Master of Science

Department of Mechanical Engineering

University of Alberta

ABSTRACT

The present work developed an automated ball-on-plate abrasive wear tester and examined the material abrasion wear resistance by volume loss and their acoustic emission characteristics. The performance of three types of materials with varying material properties, including aluminum, polyurethane-coated aluminum and stainless steel, were investigated. Friction and wear testing were carried out under different experimental conditions. To test the effect of normal load, three levels of normal load at approximately 20, 15 and 10 N and three types of lubrication conditions using water, silicone oil and no lubricant were tested. An average sliding velocity of 0.418 m/s and a test duration of 120 s were employed, achieving a total sliding distance of 50.2 m. Two types of acoustic emission data were acquired, including continuous data at 50 Hz and bursts data at 10 MHz. The investigations found that the volume loss due to sliding abrasion for aluminum and stainless steel was inversely proportional to the hardness and proportional to the normal load, which is consistent with the Archard's equation. Polyurethane, when used as a protective film on aluminum, reduced volume loss due to its high elastic deformability. Overall, stainless steel showed the least volume loss and, thus, the highest abrasion wear resistance, with polyurethane being less and aluminum the least wear resistant. This was likely due to stainless steel having greater hardness than the other two types of materials examined. In addition, AE RMS analysis, FFT transformation and correlation with friction force was performed for 50 Hz continuous data, showing a positive correlation between kinetic friction and delayed onset of AE. For the 10 MHz burst data, FFT power spectra in dB scale was obtained and compared for different test conditions. Variance, skewness, and kurtosis were calculated on an assumed β distribution and plotted against time. Furthermore, the Hilbert-Huang transform was applied to the burst data acquired at 40 s,

demonstrating patterns in the Hilbert spectra characteristic of material type, normal load and lubrication conditions, and also showing a correlation between volume wear and instantaneous energy. These AE characteristics can potentially be used for abrasion wear monitoring.

This thesis is dedicated to my wife Jie whose unwavering support has made it all possible, and to my children, Lisa and Finn, whom I wish to inspire.

ACKNOWLEDGMENTS

First and foremost, I would like to thank my supervisor Dr. Michael Lipsett for his patience and understanding, and for his guidance through the scientific research and writing process.

I am grateful to all of those whom I had the pleasure to work with during all these years as a graduate student from whom I have learned a great deal both academically and personally.

I would also like to acknowledge my in-laws whose help I am gratefully indebted to.

Finally, I would like to thank my parents who have taught me a great deal.

Table of Contents

List of Tables

List of Figures

I. Introduction

i. Motivation and Thesis Outline

Hydrotransport is the transportation of solid particles in a liquid carrier stream in either open channel or closed conduits [Gulliver et al., 2010]. This transportation method is used in a number of industrial sectors, including mining, energy, chemical production, and agriculture. In the oil sands industry, hydrotransport serves two purposes: to transport oil sands from the wet ore preparation plant to the primary separation cells, and to break down oil sands ore via the application of mechanical shear [Suvarna et al., 2019].

Although hydrotransport is a fast and cost-efficient method to transport granular solid materials over long distances, the constant operation causes wear to pipes. One of the most pronounced wear mechanisms is abrasive wear which occurs in mixed phase fluid systems with solids impinge onto surfaces. Excessive pipe wear can lead to pipe failure resulting in costly repairs, stop in operation, and environmental damage. Understanding wear mechanisms in slurry pipeline systems is crucial to structural health monitoring and to reduce the risk of catastrophic failure.

Evolving pipeline design, varying operating conditions and diverse material selection continuously add to the complexity of the wear mechanisms of slurry pipelines, making it a challenging task to assess pipeline wear. According to a study conducted by Suncor Energy Inc. on their existing oil sands hydrotransport lines in Fort McMurray, on a 3-kilometer line, wear at the top was 20 mm/year at the front of the line and 2 mm/year at the end, whereas wear at the bottom was 7 mm/year at the front and 3 mm/year at the end [Parent et al., 2013]. This example demonstrates variation in wear rate dependent on pipeline location, but many other parameters are involved. It illustrates need in developing effective wear models for predicting wear behavior. Currently, the practices in oil sands industry either replace a partially worn pipe to prevent leakage, which wastes useful pipe life or wait until a leakage occurs and then replace

the pipe, which pollutes the environments and often results in unwanted project deferrals. To the best knowledge of the author, no real time monitoring methods or devices exists.

The objective of this thesis is to examine the feasibility of utilizing acoustic emission sensors to monitor real-time abrasive wear on pipelines through the development of a novel device and accompanying software. Specifically, a simplified single particle abrasion model was designed to simulate the inner pipe wall and slurry particle interactions and characterize wear under similar conditions as during the oil sands hydrotransportation. The novel device was comprised of a variable frequency drive (VFD), a gear box, a crank wheel and an abrasion apparatus and a test plate. This device was tested by oscillating a stainless-steel ball under a normal force across the surface of a test plate via the control of a VFD. Such a setup simplified a complex system with multidirectional movement to a linear, two-directional particle movement. The resultant material wear was characterized by mass loss measurement and acoustic emission analysis. A series of experimental conditions were studied, including the normal force applied on the ball, the plate material (aluminum, polyurethane-coated aluminum and stainless steel), and lubrication.

Mass loss measurement was carried out by weighing the plate before and after an experiment. Acoustic emission analysis was achieved utilizing sensors. More specifically, three types of sensors, potentiometer, strain gauge and acoustic emission sensors, were incorporated to measure the displacement of the stainless-steel ball, to measure the forces applied and to acquire acoustic emissions from the frictions between the ball and the plate, respectively. Furthermore, data acquisition was achieved by the development of an in-house LabWindows software.

Following the scope of the study, Chapter II provides backgrounds on slurry pipeline system, wear mechanisms, sensing techniques, and laboratory wear testers. The goal of the first chapter is to shine some light on the significance of the work, discusses the underlying physics related to the research as well as present lab-scale testers developed to characterize wear. Chapter III delves into the experimental design and test methods, listing the principal assumptions, defining variables and the experimental equipment and instrumentation required to capture those

variables, test material selection, control, and data analysis software. Results are discussed in Chapter IV, characterization of abrasive wear by mass loss, coefficient of friction and acoustic emission. Chapter V summarizes the work, its limitations, and offers recommendations for future work.

II.   Literature Review

i.   Slurry Pipeline System

1. Hydrotransport Technology

The Canadian province of Alberta is home to the largest reserves of oil sands existing in the world. These reserves boosted the development of the oil sands industries in northeastern Canada in the early 1990s. In 2011, Canada exported on average 1.25 million barrels of crude oil per day to the United States (Crosbya, et al., 2013). Oil sands are unconventional hydrocarbon deposits that consist of clay, sand, ice and viscous petroleum product know as bitumen. Typically, the composition is 3-18 % (weight percentage) bitumen, 50-75% sand, 10-30 % clay, and 2-10 % water (Yang, Tsai, Serate, & Wu, 2018).

In order to efficiently break down the lumps of oil sands and extract the valuable bitumen fraction from the uneconomic fraction, hydrotransport technology was applied to oil sands processing in the early 1990s (n.d.). Hydrotransportation is defined as the transportation of solids in a liquid carrier stream. Depending on the carriage being an open or closed conduit, the flow can be categorized either as open channel conduit flow (where the flow is driven by gravity), or closed conduit flow (where the flow is driven by pressure). A typical hydrotransport facility comprises large diameter slurry pipelines that connect slurry preparation equipment to the main extraction plant. The lumpy oil sands slurry, which is amixture of oil sands and hot water, travels down the pipeline at 3 to 5 m/s. The high pressure applied through pumps and the high turbulent flow impart a significant amount of shear mechanical force onto the slurry, breaking apart the lumps and liberating the bitumen. During this process, the freed fraction of

bitumen particles moves into the water; and these particles are suspended along with air bubbles and mineral solids in the slurry mixture. The coarse sand and heavy lumps drag along the bottom of the pipeline, causing erosion of the pipelines, whereas the dissolved oxygen and carbon dioxide in the process water contribute to corrosion.

Due to the high degree of erosion and corrosion, hydrotransport lines are some of the most maintenance-intensive components in the oil sands industry. There is an ongoing effort in the scientific community to understand the wear mechanisms in the slurry pipelines. Through research and development, wear models can be developed to characterize the behavior of slurry particles and understand their interactions with the pipeline walls, providing important information to guide design, operating, and maintenance practices to improve the overall reliability of the pipeline system.

2. Slurry Properties

Slurry is a heterogeneous mixture of liquid and solid particles that can be transported by pumping (Ojala, et al., 2016). The slurry rheological property is affected by many properties of the solid particles and carrier fluid. For instance, solid particle size and density determine if the slurry is settling or non-settling. Slurry with coarser particles and particle density higher than that of the fluid tend to have settling particles accumulating at the bottom of the channel (Peker, Helvaci, Yener, Ikizler, & Alparslan, 2008), whereas non-settling slurry is composed of smaller particles with a density lower or equal to that of the fluid.

The flow behavior of slurries can be classified into the following conditions (Peker, Helvaci, Yener, Ikizler, & Alparslan, 2008):

a) Homogeneous flow. In homogeneous flow, all solid particles are suspended uniformly across the pipeline cross section and throughout the flow direction. The particles settle very slow and remain in suspension. This flow behavior is typically encountered when

particle sizes are below 75 mm (Curtis, 2008). Homogenous slurries are also referred to as non-settling slurries.

b) Heterogeneous flow. In heterogeneous flow, the solid particles distribute across the pipeline cross section in a concentration gradient. Slurries in heterogenous flow can cause particles either to suspend fully with marked concentration gradients as a single-phase flow, or to settle to the bottom of the pipe forming a two-layer flow.

c) Saltation regime. In this flow regime, a three-layer formation manifests at the pipeline cross section. A stationary bed of particles may accumulate at the lower wall due to low flow rate. There is a moving layer of solid particles on top of the stationery bed and then, further atop this moving layer is a heterogeneous liquid flow layer.

In a hydrotransport system, it is ideal to avoid settling of solids by maintaining the fluid velocities of the pipelines above certain levels. This is understandable as the settling solids drag along the bottom and cause a higher degree of wear on a pipeline. As a result, selection of appropriate pipe diameters and pump pressures is of prime concern to engineers. A hydraulic characteristics curve (Figure 1) can be graphed by correlating the log of pressure gradient to the log of superficial velocity (calculated as volumetric flow rate divided by the cross-section area of the pipe), which can be used to determine acceptable operating conditions to prevent solid particles from settling out. In Figure 1 below, critical deposition velocity delineates bed-forming and fully suspended flows of liquid-solid mixtures, such as slurries (Rice, Peakall, Fairweather, & Hunter, 2020). When slurries are pumped at a velocity above this threshold, solid particles will theoretically stay suspended in solution.

Non-settling, homogenous slurries can be pumped through a pipeline in either laminar or turbulent flow. As shown in the figure below, as the superficial velocity increases, non-settling slurries display a more abrupt increase in slope as it transitions from laminar flow to turbulent flow than settling slurries. Like liquids, homogeneous slurries may exhibit either Newtonian or non-Newtonian flow behaviors. At low particle concentrations, slurries are Newtonian, while at high particle concentrations, slurries are non-Newtonian.

In Newtonian fluids, a linear relationship exists between the shear stress and the shear rate in laminar flow

$$\tau = \eta\dot{\gamma} \tag{1}$$

where τ is the shear stress, $\dot{\gamma}$ is the shear rate (force per unit area) or velocity gradient (units of inverse time, for example, s-1) and η is the liquid viscosity. It can be deduced from this equation that the slope in Figure 1 represents the viscosity of a slurry. When slurries behave like non-Newtonian liquids, the relationship between shear stress and shear rate becomes non-linear and can be modeled using power-law as:

$$\tau = k\dot{\gamma}^n \tag{2}$$

where k and n are constants that represent consistency index and dimensionless flow behavior index, respectively.
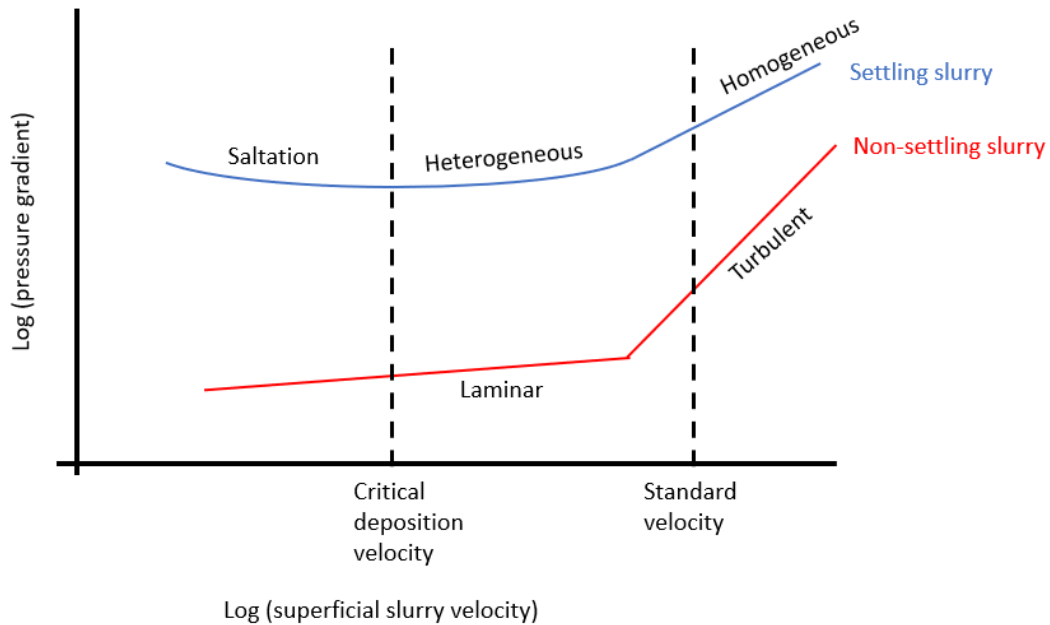
Figure 1. Examples of hydraulic characteristics for settling and non-settling slurries (Curtis, 2008).

ii.　Wear Mechanisms

Wear in hydrotransport lines in the oil sands industry has been an ongoing issue since the industry was established over 50 years ago. Material performance is highly dependent on the specific conditions along the pipeline, which makes the material selection for optimal wear performance a challenging task. Despite the technical importance of wear, the multitude of physical mechanisms contributing to wear makes it difficult to develop a simple and universal model that represents and characterizes it. The purpose of this section is to illustrate the three dominant degradation mechanisms encountered in the pipeline systems: namely, abrasive wear, erosive wear, and corrosive wear.

1.　Friction-wear relationship

Friction and wear are closely but distinct phenomena. Friction manifests as the force required to initiate or sustain motion between two contacting bodies (Jiménez & Bermúdez, 2 - Friction and wear, 2011). Friction can be separated into two regimes as static friction, the forced needed to overcome the potential energy between two surfaces and initiate motion, and kinetic friction, the mechanisms describing the gradual loss of energy during relative motion. In contrast, wear is the damage to a solid surface, produced by friction. In another word, a portion (estimated to be less than 10%) the energy dissipated by friction produces wear. The remaining portion contributes to heat loss, acoustic emission and changes in surface roughness etc. (Bogdanovich & Tkachuk, 2009).

Three laws derived from empirical observations have been used to describe friction:
The first two laws were asserted by French physicist Guillaume Amontons (1663-1705) (Amontons, 1706). The first law states that the friction force F between a pair of loaded sliding surfaces is proportional to the normal load W (Figure 2) and can be calculated using the coefficient of friction, μ, as expressed:

$$F = \mu W \tag{3}$$

The second law of friction states that the friction force is independent of the apparent area of contact. The third law, also known as the Coulomb's law of friction, asserts that the kinetic friction is independent of the sliding velocity. Under sliding conditions, there is no general relationship between friction coefficient and wear rates. It is a function of the various mechanisms of kinetic energy conversion and dissipation, such as adhesion, surface fatigue, chemical reaction, and abrasion.
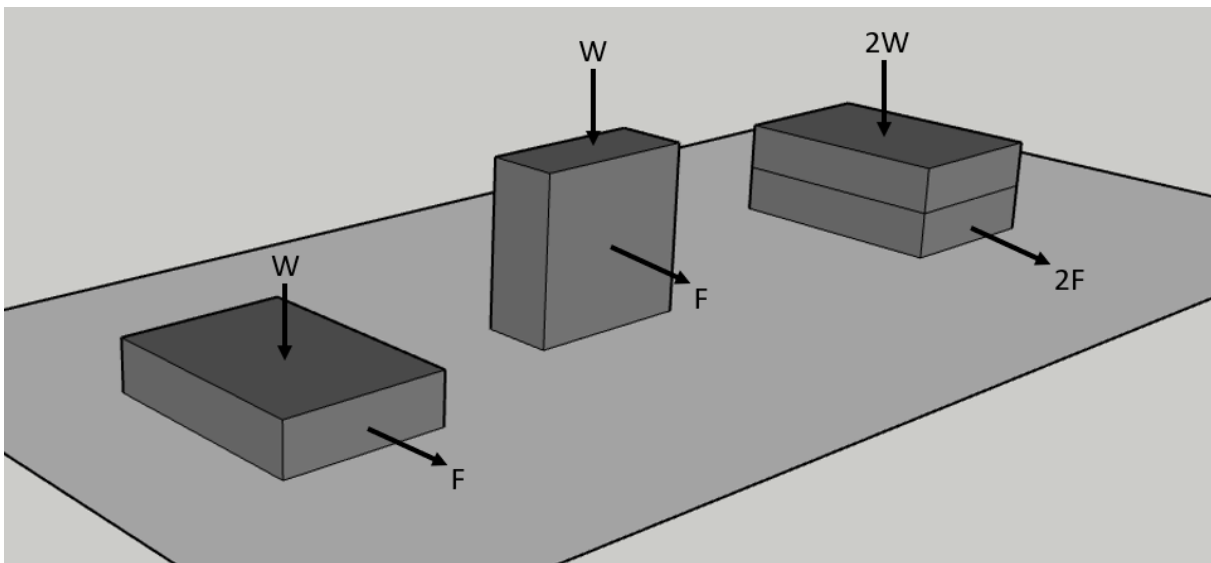
Figure 2. Schematic representing two contacting bodies and the correlation between friction force, F and normal load, W (Jiménez & Bermúdez, 2 - Friction and wear, 2011).

2. Abrasive and Adhesive Wear

Abrasive wear is caused by the sliding of particles against a solid material. It is often accompanied by the removal or displacement of the material from that surface (Hokkirigawa & Kato, 1988) and produces parallel grooves inside the wear track (Figure 3) without plastic deformation. For it to occur, the sliding particle hardness must be greater or equal to the surface being abraded (at least 1.3 times harder) (Jiménez & Bermúdez, 2 - Friction and wear, 2011).
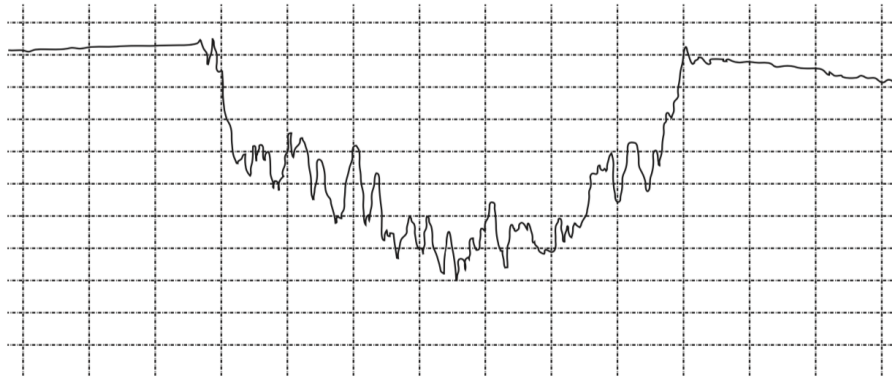
Figure 3. Abrasive wear scar profile obtained by contact profilometry, showing abrasion grooves inside the scar and the absence of plastic deformation at the edges (Jiménez & Bermúdez, 2011).

The mechanism of abrasive wear includes micro cutting, fracture, fatigue and grain pull-out (Stachowiak & Batchelor, Engineering Tribology, 2014). Micro cutting describes the effect that particle geometry has on abrasive wear. Particles containing more micro-cutting edges can remove more material than unfractured particles of spheroidal shape (Stachowiak & Batchelor, Engineering Tribology, 2014). Fracture describes the possibility of crack propagation on brittle materials when the particle is loaded onto the surface. Repeated strain from the sideways displacement of sliding particle could produce repeated deformation leading to metal fatigue. Grain pull-out happens when a sliding particle pulls out an entire chunk of grain from the solid surface due to a failed inter-grain bond.

The two general types of abrasive wear are: two-body abrasion and three-body abrasion. Two-body abrasion constitutes of a hard particle rubbing against a softer surface, while in three-body abrasion hard particles are trapped between two sliding surfaces (Arnell, 2010). Specific wear rate, k , is used to quantify abrasive wear. It is defined as the volume of material worn away by a unit load and unit sliding distance:

$$k = V/(WL), \ L = vt \qquad\qquad (4)$$

$$L = vt \qquad\qquad (5)$$

where V is the volume of the removed material in cubic meter, W is the normal applied load in newton and L is the total sliding distance in meter, v is the particle sliding speed and t is the total time.

In general, abrasive, and adhesive wear tend to coexist. Adhesive wear occurs when direct contact between solid surfaces results in welding and material transfer between the two surfaces. It is not as prevalent as abrasive wear and is normally involved in the wear process when like materials slide against each other with no lubrication.

3. Erosive Wear

Erosive wear happens when solid particles, which move through pipelines at a certain angle and velocity, impact the material surface and create scars; this phenomenon is called "slurry erosion wear" (Zhang, Kang, Fan, & Gao, 2016). Variables that influence the rate of wear include angle of impingement, particle velocity, particle size, particle hardness, and physical properties of the surface materials. The equation below correlated the erosion wear with the impact angle, impact velocity and the materials and incident particles:

$$E = cv^n f(a) \qquad\qquad (6)$$

where v is the particle velocity, a is the impact angle with respect to the material surface and the coefficient n varies based on the material (Divakar, Agarwal, & Singh, 2005).

The different combinations of these variables result in various mechanisms of erosive wear, such as abrasion, fatigue, plastic deformation, melting. Abrasion happens when the angle of impingement is small. Plastic deformation happens when the impingement angle is normal to the surface and metals slide at low speed. Additionally, the particle hardness must be higher than the surface material hardness, otherwise the striking particle suffers particle degradation

(Affatato & Brando, 2013). Plastic deformation leads to various of surface damages. One of these damage forms is fatigue, where particles repeatedly strike a surface.

Roco and Addie described an energy approach to determine the erosion wear in slurry pumps and pipes from the particle (d ≤ 0.5 mm) velocity and concentration distribution in the vicinity of the exposed walls (Roco & Addie, 1987). The correlation between the energy dissipated by particle-wall interactions and the erosion wear rate was verified combining computational and experimental steps. Three wear mechanisms differentiated by the particle dynamics pattern close to the wall were discussed and studied separately using small-scale devices. The three mechanisms are: directional impact, random impingement and Coulombic friction (sliding and rolling), as shown in Figure 4 below. The total wear rate was estimated using correlations between thickness loss (the amount of material removed) and interaction energy. The authors pointed out that the erosion mechanisms have a stochastic character, due to the random size and shape of the particles, the random velocities under various impingement angles and used probability density distribution functions to describe the particle-wall interaction.
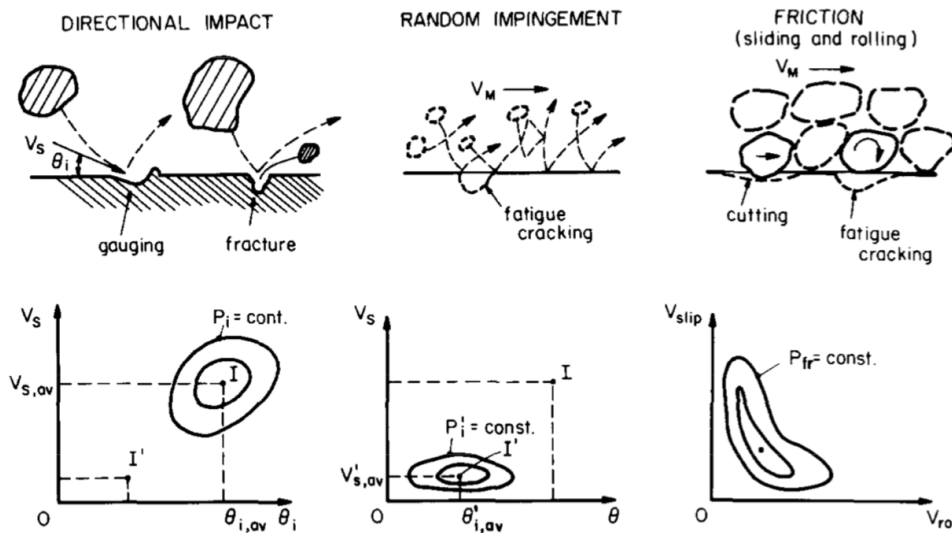
Figure 4. Erosion wear mechanisms based on particle-wall interaction (Roco & Addie, 1987). V_s is impact particle velocity; θ_i is the impact angle of the particle on the solid wall; P_i, P'_i and P_{fr} denote the probability density distribution functions for directional impact, random impingement and Coulombic friction, respectively. Subscripts M, av, rol and slip denote mixture, average, by rolling and by slipping, respectively.

A number of other empirical wear models have been developed that include a range of particle, material, and flow properties.

4. Corrosive Wear

Protective films and passivating oxide layers can be removed by wear and the resultant loss of material is often associated with corrosion (Jiménez & Bermúdez, 2 - Friction and wear, 2011). Corrosive wear occurs when there is a chemical or electrochemical reaction between the surface and the environment. This complex reaction varies dependent on the corrosive medium in contact with the surface. Carbon dioxide corrosion plays a big role in the degradation of carbon steel pipelines (Yu, Li, & Grondin, 2013). The corrosion rate by carbon dioxide is influenced by the level of dissolved oxygen contained in the slurry. In pipeline operation term, it is dependent on the pressure. This is because pressure affects the amount of oxygen dissolved in the water. The higher the operating pressure, the more oxygen from the excess air inside the pipe gets dissolved in the water, which promotes a higher degree of corrosion at the inlets of the pipelines. As the slurry travels down the pipeline, oxygen get consumed by oxidation of substance in the slurry and results in less severe corrosive wear at the end of the line than at the inlets (Parent & Li, 2013). Additionally, it has been demonstrated that the water containing both dissolved oxygen and carbon dioxide is more corrosive than water containing only dissolved oxygen or carbon dioxide (Kermani & Smith, 1997).

Dissolved oxygen can considerably accelerate the erosion of pipeline steel because of the involvement of corrosion. The effect is known as the synergistic attack of erosion and corrosion (Neville, Reza, Chiovelli, & Revega, 2005). More specifically, during the erosion-corrosion processes: carbon dioxide corrodes iron to produce ferrous carbonate, which forms a porous, protective scale over the steel. The solid particle impingement destroys the corrosion product scale and thus, accelerates corrosion with continuous exposure of fresh metal surface to the environment. The particle impingement can also cause local plastic deformation, which renders the steel more susceptible to corrosion.

Pipeline failure by the synergistic combination of erosion and corrosion were classified as erosion-enhanced corrosion (EEC), when the damaged region is confined within the oxide layer and corrosion-affected erosion (CAE), in which the damaged zone includes both oxide scale and the metal substrate underneath (A.S.M. Handbook vol. 18, 1992).

In summary, the exact wear mechanism in the hydrotransport pipelines is highly circumstantial and requires careful analysis. The material degradation rate has been proven to be affected by pressure, size of the transported material, density, temperature of the mixture, velocity, distance pumped, pipe geometry, and the water chemistry.

iii.   Sensing Techniques

Characterization of wear mechanisms or wear rates can be achieved using a plethora of techniques. It can be quantified after the wear events using techniques such as profilometry, mass loss or linear dimension loss due to long-term geometry change. Even though these types of techniques are straightforward, they do not provide insight into the dynamics of the wear process. In contrast, wear can be monitored in real time through direct or indirect methods. Real-time monitoring has the advantage of identifying the onset of severe wear and enables timing intervention. It has significant implications in industrial applications such as oil pipeline maintenance (Dyskin, et al., 2018). In the case of direct methods, wear is measured by electrical, optical or radioactive resistance sensors. Examples include strain gauges and fiber optic sensors. Indirect methods of real-time monitoring include ultrasonic testing, acoustic emission and electrostatic sensing. The discussion below focuses on a few commonly used sensing techniques.

1. Strain Gauges

Strain gauges are sensors whose resistance varies with the applied force. They are one of the most common strain measurement techniques used to monitor long-term pipeline wear. Strain gauges are cemented to the surface of a pipeline. As a pipeline deforms, strain is directly transferred to deform strain gauges, which respond with a change in certain measurable properties of the strain gauge.

To understand how strain gauges can monitor pipeline wear, it is essential to understand the relationship between stress and strain. Stress is never the quantity measured in wear monitoring because stress (σ) is the applied force (F) over a surface area (A) and can only be measured in the process of its application

$$\sigma = F/A \tag{7}$$

What is invariably measured to determine stress is strain, defined as the amount of deformation experienced by a material due to the applied force. Mathematically, it is expressed as the ratio of the change in length of a material to its original length

$$\epsilon = \Delta L/L \tag{8}$$

By convention, strain is represented in dimensionless units of 10^{-6} m/m, which is also called microstrain ($\mu\epsilon$). Strain due to elongation of a material is called tensile (positive) strain, whereas strain due to contraction of material is called compressive (negative) strain. Axial strain is when a material elongates or compresses due to linear force in the same direction. Bending strain is when a material is under the action of bending. And shear strain occurs when a material is under a shear force.

Various methods can be used to measure strain, including mechanical gauges, electrical-resistance gauges, optical gauges, Birefringent methods, diffraction methods (x-ray and neutron), ultrasonic methods, and magnetic methods (Ruud, 2002). The most commonly used gauges for monitoring pipeline wear are electrical-resistant gauges, which are made from either metallic or semiconductor materials.

a. Metallic strain gauges

When the force applied on an electrical-resistance strain gauge changes, a corresponding change in the electrical resistivity of the material takes place. This concept was founded by physicist Lord Kelvin (William Thomson). According to the theory, the electrical resistance of an object increases or decreases with increasing or decreasing strain experienced by the object. Consider a metallic strain gauge with a uniform cross-sectional area S , electrical resistivity ρ and length L, its electrical resistance can be calculated using the equation below (Figliola & Beasley, 2011)

$$R = \frac{\rho L}{S} \tag{9}$$

Based on this given relationship, it can be deduced that electrical resistance R is the combined effect of changes in cross-sectional area and length. The total change in R can be differentiated as the following (Figliola & Beasley, 2011)

$$dR = \frac{(\rho \cdot dL + L \cdot d\rho) \cdot S - \rho \cdot L \cdot dS}{S^2} \tag{10}$$

which can be expressed in terms of Poisson's ratio v as

15

$$\frac{dR}{R} = \frac{dL}{L} \cdot (1 + 2v) + \frac{d\rho}{\rho} \tag{11}$$

Hence, change in electrical resistance is contributed by change in cross-sectional area, length and electrical resistivity. E is the Young's modulus or modulus of elasticity? The dependence of electrical resistivity on mechanical strain is called piezoresistance. It can be expressed in terms of a piezoresistance coefficient λ, expressed as

$$\lambda = \frac{1}{E} \cdot \frac{d\rho/\rho}{dL/L} \tag{12}$$

Therefore, electrical resistance change per unit resistance can also be written as (Figliola & Beasley, 2011)

$$\frac{dR}{R} = \epsilon \cdot (1 + 2v + \lambda \cdot E) \tag{13}$$

The correlation between electrical resistivity change and strain can be determined empirically and this is known as the gauge factor or electrical resistivity sensitivity coefficient k_σ, defined as

$$k_\sigma = \frac{\Delta\rho/\rho}{\Delta L/L} \tag{14}$$

Maričić *et. al.* (A.Maričić, et al., 2012) characterized the k_σ of an amorphous metallic alloy. Figure 5 demonstrates the dependence of gauge factor on the applied stress under a certain temperature. The gauge factor varies from material to material. Additionally, as changes in temperature tend to cause an apparent strain, temperature is often needed a correction for.
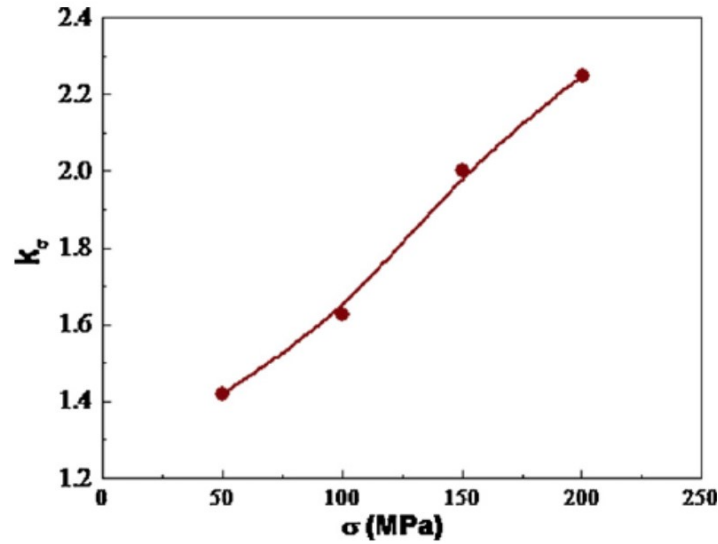
Figure 5. Relationship between applied stress and the electrical resistivity sensitivity coefficient k_σ of a metal alloy (A.Maričić, et al., 2012).

b. Electrical Wheatstone bridge circuits of strain gauges

Electrical-resistance strain gauges are available in a variety of sizes, shapes and configurations. Sizes as small as 1 mm attribute to the good spatial resolution. Configurations affect the sensitivity of a gauge to strain and temperature changes. In practice, the changes in strain on a pipeline are usually small. To ensure the accuracy and sensitivity of detection, the concepts of Wheatstone bridge were developed, which is illustrated in Figure 6. The output of the circuit under the illustrated setup is given by the following equation (Figliola & Beasley, 2011)

$$E_0 + \delta E_0 = E_i \frac{(R_i + \delta R)R_4 - R_3 R_2}{(R_1 + \delta R + R_2)(R_3 + R_4)} \tag{15}$$

where E_0 is the voltage output of the bridge at initial state, R_1, R_2, R_3, R_4 are the resistances in the strain gauges, δR is change in the strain gauge resistance, and δE_0 is bridge deflection according to change in resistance. When $R_1 = R_2 = R_3 = R_4$, the setup is referred to as a balanced

17

bridge; however, if at least one of the strain gauges has a resistance different from the rest, the bridge becomes unbalanced and produces an electrical output as a function of strain. Three types of Wheatstone bridge configurations are widely used, including quarter-, half-, and full-bridge, and these determine the number of active elements in the Wheatstone bridge.
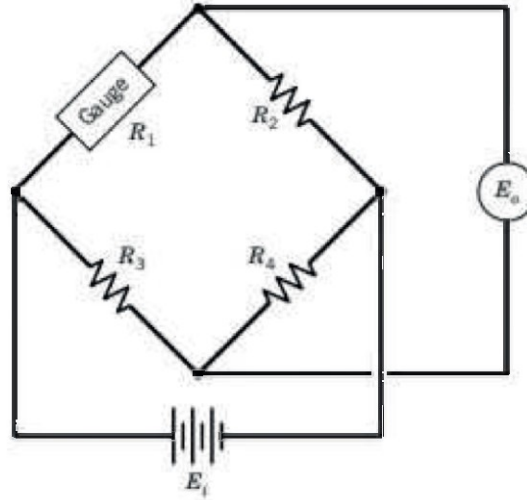
Figure 6. General Wheatstone bridge circuits of strain gauge (Figliola & Beasley, 2011).

In slurry hydrotransportation, strain gauges have been used to monitor external stresses on polyethylene pipeline. External loads caused by an influence of unstable area result in longitudinal strain, circumferential strain, and torsional strain [Gawedzki et al., 2015]. Strain gauges work by measuring the electrical resistance change of the metal grid pattern in the sensor due to the strain experienced by the carrier plate. The key to the success of a long-term measurement of pipeline wear is ensuring the integrity of the installed gauges over time. Different types of gauges are attached to the pipe using different methods and provide a range of durability. Foil gauges are commonly attached using adhesive, such as epoxy glue. Wire gauges can be attached via welding, but the specific methods approach need to be selected based on the pipe materials.

As any sensing techniques, the utilization of strain gauges has limitations. Apart from the need for temperature correction, strain gauge measurement requires electrical wires to run the length of the system, making them prone to electromagnetic interference. Additionally, electrical signal transmission losses limit the range of application for strain gauges.

2. Fiber Optic Sensors

For many reasons, fiber optic sensors (FOSs) are considered as ideal transducers for long-term health monitoring: they are durable, stable and insensitive to external perturbations.
A great variety of FOSs exist, and the four main types are illustrated in Figure 7 (Peters & Inaudi, 2014):

- Point sensors. Have a single measurement point at the end of the fiber optic connection cable.
- Multiplexed sensors. Enable multi-point measurement along a single fiber line.
- Long-base sensor. Also known as long-gauge sensors. Integrate the measurement over a long measurement base.
- Distributed sensors. Can measure any point along a single fiber line. Suitable for pipelines that are many kilometers of length.

Point sensor:
Fabry–Pérot

Quasi distributed (multiplexed):
fiber Bragg gratings

Long base:
SOFO

Distributed sensor:
Brillouin and Raman scattering
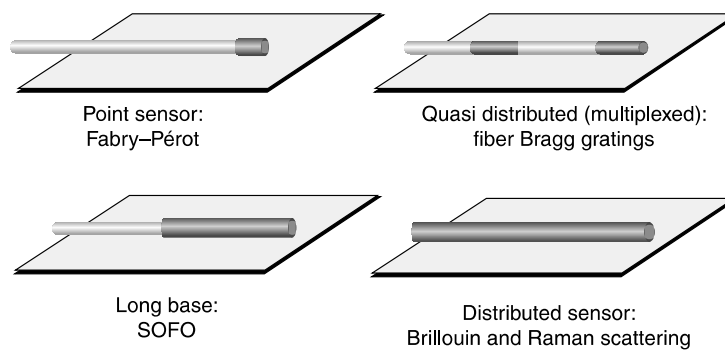
5.1 Fiber optic sensor types. (SOFO - surveillance d'ouvrages par senseurs à fibres optiques (structural monitoring by fiber optic sensors).)

Figure 7. Fiber optic sensor types (Peters & Inaudi, 2014).

FOSs can also be divided into extrinsic and intrinsic sensors. Extrinsic sensors use the fiber to guide light to a sensing region where the optical signal exits the cable and is modulated in another medium. In contrast, in intrinsic sensors, light remains inside the waveguide, measuring the effects of optical signal change (intensity, phase, polarization, wavelength, and transit time) as it moves down the fiber (Culshaw, 2006).

Optical fibers generally consist of a fused silica core and cladding. This basic structure determines their advantages over conventional sensors that use electrical cable:

- Chemical resistance: since glass is an inert material and is resistant to almost all chemicals, it is an ideal material for long-term structural monitoring even in harsh environments.
- Immunity to electromagnetic interference: light is confined in the core of the optical fibers used for sensing. Hence, they do not interact with any surrounding electromagnetic field.
- Long-range monitoring and multiplexity: ability to offer long range distributed sensing capabilities or large networks of multiplexed sensor.

The structural strain can be transferred to a properly attached fiber optic, which act as filters transmitting only certain wavelengths and reflecting the rest. Changes in strain due to pipeline wear are therefore converted into a wavelength shift of the transmitted or reflected spectrum of the sensor. Two common optical fiber sensors that utilize this particular sensing mechanism are fiber Bragg gratings (FBG) and Fabry-Perot interferometers.

a. Fabry-Perot interferometers

Fabry-Perot interferometers are a typical example of point sensors and have a single measurement point at the end of the fiber optic connection cable. As shown in Figure 8, an extrinsic Fabry-Perot interferometer (EFPI) consists of a capillary glass tube containing two partially mirrored optical fibers facing each other but leaving an air cavity of a few microns between them. The two fibers are attached to the capillary at their extremities. A change in the distance between them (typically 10 mm) will correspond to the strain variation between these two contact points.
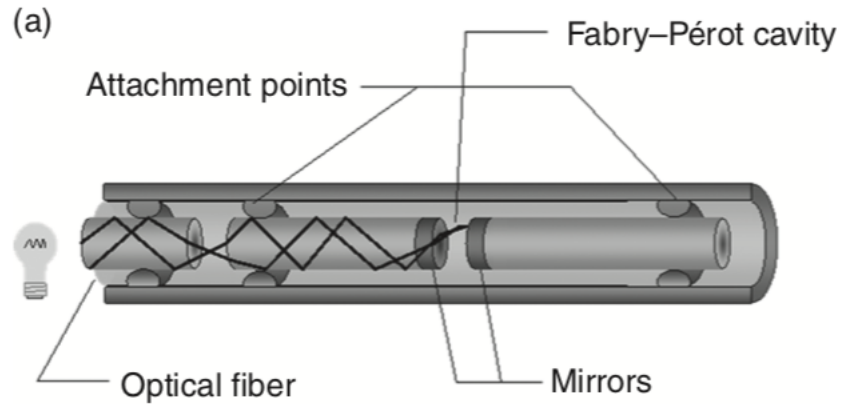
Figure 8. Schematic of a Fabry-Perot strain sensor (Peters & Inaudi, 2014).

b. Fiber Bragg gratings

Fiber Bragg grating (FBG) sensors have many advantages for strain sensing, including the ability to measure localized strain and the potential to multiplex hundreds of sensors. The FBG, as shown in Figure 9 below, is a permanent, periodical perturbation in the index of refraction of the optical fiber core. When a broad spectrum of wavelengths is passed through the FBG, a narrow bandwidth is reflected, while all others are transmitted. The wavelength at maximum reflectivity is referred to as the Bragg wavelength, λ_B, and is determined by the condition (Peters & Inaudi, 2014)

$$\lambda_B = 2n_{eff}\Lambda \tag{16}$$

$$n_{eff} = \frac{\beta\lambda}{2\pi} \tag{17}$$

where n_{eff} is the efficient index of refraction and is determined by the propagation constant β and the wavelength of the light wave in vacuum λ, and Λ is the period of the index of refraction variation.

When an axial strain, ϵ, is applied to the FBG, the Bragg wavelength shifts to lower wavelengths under compression or higher wavelengths under tension. The applied strain therefore can be calculated from the wavelength shift. For pure axial loading the following formula (Peters & Inaudi, 2014)

$$\frac{\Delta\lambda_B}{\lambda_B} = (1 - p_e)\epsilon \tag{18}$$

where p_e is the effective photo-elastic constant for axial strain. A typical value of p_e for silica optical fibers is 0.22-0.25 (Kersey, et al., 1997). The shift in Bragg wavelength is linearly proportional to the applied axial strain. However, FBG sensors are also sensitive to temperature changes,

$$\frac{\Delta\lambda_B}{\lambda_B} = (\alpha + \zeta)\Delta T \tag{19}$$

where α is the thermal expansion coefficient and ζ is the thermos-optic coefficient of the optical fiber material. A typical value for fused silica $(\alpha + \zeta)$ is 6.67 x 10^{-6} °C^{-1} (Kersey, et al., 1997). Since the measured shift in wavelength is contributed from change in both strain and temperature, thermal compensation must be considered for pipeline wear monitoring using FBG sensors.
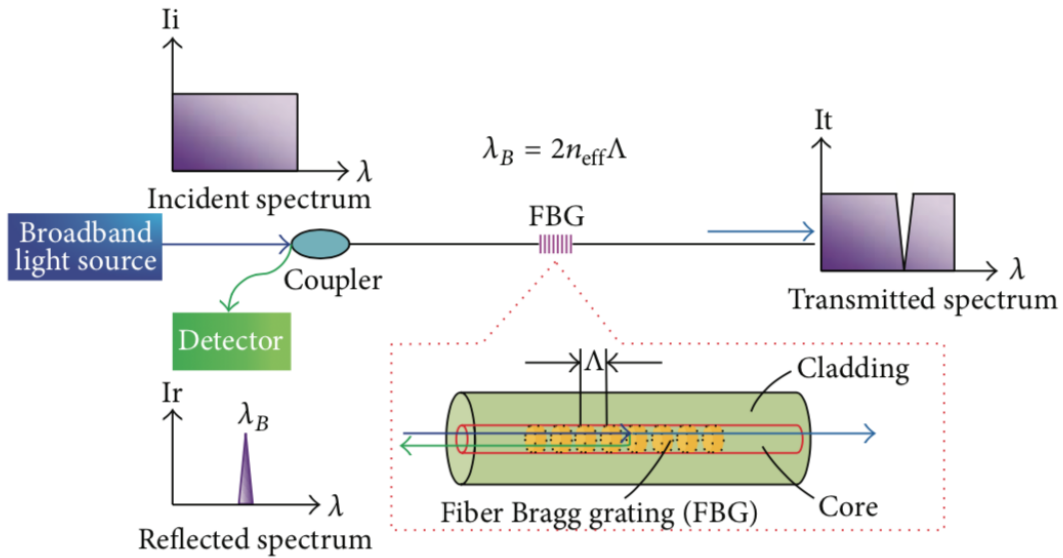
Figure 9. Mechanism of a Fiber Bragg grating (FBG) sensor (Ye, Su, & Han, 2014).

c. Brillouin and Raman scattering distributed sensors

Unlike localized FOSs such as Fabry-Perot interferometers and FBG sensors, a distributed fiber optic sensor has the ability to measure strains and temperatures at thousands of points along its entire length (up to 30 km at every meter) (Peters & Inaudi, 2014). The detection method of distributed sensors relies on a nonlinear optical effect known as Raman (Dakin, Pratt, Biddy, & Ross, 1988) and Brillouin scattering (Horiguchi, Kurashima, & Tateda, 1990) (Niklès, Briffod, Burke, & Lyons, 2005). When a laser is shone into a fiber, it generates scattered light at wavelengths higher and lower than the original wavelength at every section of the fiber. The original light wave is known as the Rayleigh component whereas the scattered lights are known as the Raman and Brillouin components, whose wavelengths respond to changes in temperature and strain.

As demonstrated in Figure 10 below, the two Raman peaks are centered around the Rayleigh peak. Their position on the wavelength scale is fixed. The amplitude of the peak at higher wavelengths is unaffected by any changes, but the amplitude of the peak at lower wavelengths

is dependent on temperature. Similarly, the two Brillouin peaks are also located symmetrically to the Rayleigh peak. Their peak intensity is fixed, but their position relative to the central peak is proportional to the local temperature and strain changes. More specifically, the Brillouin wavelength shift is correlated to the acoustic velocity in the fiber, which is determined by its density. Since the fiber density responds linearly to temperature and strain changes, Brillouin and Raman scattering can be used for measuring these changes. In the case of pipeline wearing monitor, the cross-sensitivity to temperature variations must be considered. It is typically achieved with the installation of a reference fiber along the strain sensor (Peters & Inaudi, 2014).
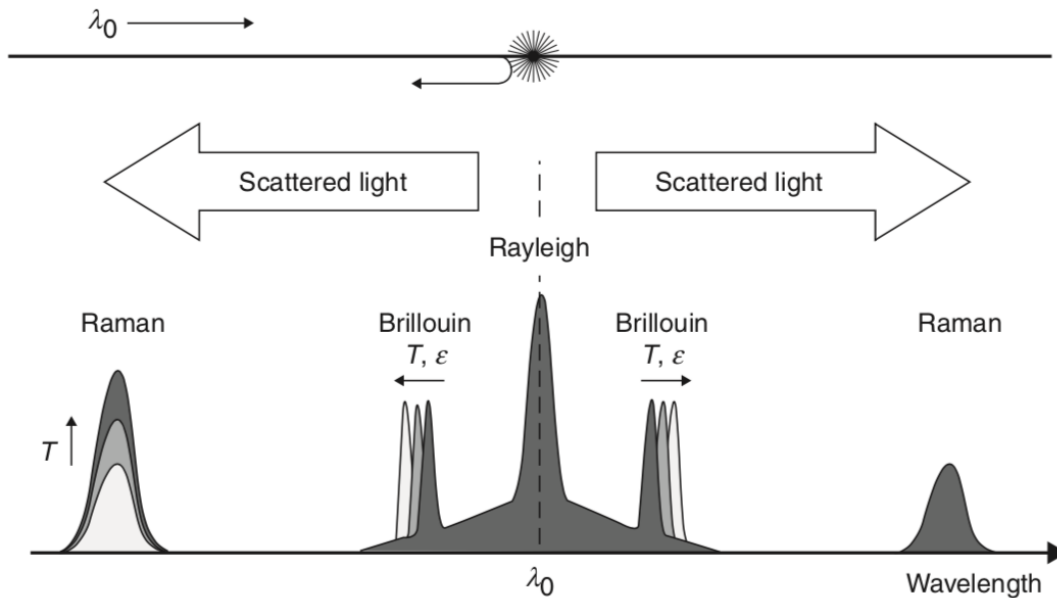
Figure 10. Raman and Brillouin scattering in optical fibers and its use for strain and temperature sensing (Peters & Inaudi, 2014). λ_0 is the wavelength of original light source, T is temperature and ε is strain.

Although optical sensors display extremely high bandwidth and are able to cover long distances, they do have certain limitations. First, they are more fragile and costly to install than electrical wires. Second, fiber cable installation is difficult because they are highly susceptible to damages. And last, as transmission distance increases, light will be attenuated and dispersed, extra optical components such as Erbium-Doped Fiber Amplifiers (EDFA) are needed to compensate signal attenuation.

3. Acoustic Emission Testing

Acoustic emission (AE) is the emission of elastic stress waves resulting from deformation and fracture of materials (Hase A. , 2015). It is commonly used for identifying wear based on frequency signature from different materials. Experimental data suggest that AE method is more sensitive to the process of friction surface damage than the measurements of friction force/coefficient or vibration (Rastegaev, Merson, Rastegaeva, & Vinogradov, 2020). As a result, it is the preferred method for characterizing abrasive and adhesive wear.

Specifically, AE method aims at detecting the transient, acoustic stress waves generated by the rapid release of strain energy from localized micro-structural changes (MEO, 2014). Stress waves travel from its origin to the surface of a material and become surface waves, which are detectable by sensors if the waves are of sufficient amplitude. AE is a function of the applied stress. One main advantage of AE methods is that, since acoustic waves propagate through the structure, they can be used to monitor inaccessible areas, such as the inner wall of a slurry pipeline. AE testing is also a nondestructive detection technique, which means materials are examined in ways that do not impair their future usefulness (Chong & Carino, Health monitoring of civil infra- structures, 2003).

Generally speaking, AE testing consists of the following steps:
a) Structure under loads produce stress
b) Elastic energy is released
c) Acoustic waves propagate from the source to the sensors
d) AE transducers convers acoustic waves into electrical signals
e) Electrical signals are acquired and filtered
f) Signal processing and interpretation

In pipeline wear monitoring, AE testing can be used to analyze pure erosion. It is theorized that particle impacts transfer energy from erosive wear events through acoustic waves that can be picked up by acoustic sensors fixed to the outside of the pipe [Jonathan et.al., 2013]. The

electrical signal converted from acoustic waves by the transducers can then be compared with test samples to estimate pipe wear. The accuracy of this method relies on the accuracy of the test sample performed. This method is prone to outside acoustic interference that could cause errors in the data acquired. As a result, there is a need to employ careful and efficient filtering technique in the signal processing step.

Adhesive wear and abrasive wear mechanisms tend to coexist. The individual wear mechanism can be identified by frequency analysis of AE signal waveforms. Studies found that for abrasive wear, AE frequency peaks occurred at lower frequency region than adhesive wear. For instance, Hase (Hase A. , 2015) noted, for a pin-on-disk sliding test, a primary peak at 0.1 MHz or lower for pure sliding friction. In adhesive wear, frequency peak appeared at a higher frequency region around 1.0 MHz and in abrasive wear, frequency peaks occur at a low frequency region around 0.5 MHz. This trend was observed for both two-body and three-body abrasive wear (defined in section iv. 1 below). In a study to detect onset of seizure in journal bearing (Hase, Mishina, & Wada, 2016), the authors observed that by detecting AE signals at more than 1 MHz, early detection was possible at about 90% of the lifetime of the bearing before seizure.

AE analysis can also be used to identify corrosion. Ramadan et. al. (Ramadan, Gaillet, Tessier, & Idrissi, 2008) utilized principal component analysis to discriminate localized corrosion from stress corrosion cracking in prestressed concrete structures. Acoustic emissions originating from secondary effects such as peeling and breaking of corrosion products during pressurization has also been used to monitor corrosion under insulation of a pressure vessel (Tscheliesnig, Lackner, & Jagenbrein, 2016).

There were three main types of acoustic emission data, including bursts, continuous and mixed data types (Holroyd, 2000). Bursts are transient signals that are acquired when the acoustic emission surpasses a set threshold. Continuous signals are acquired when the transients overlap. Mixed data types contain both continuous and burst signals. As shown in Figure 11 below, a typical burst AE signal contains the stress waves as a function of time. Such a signal is also called ring-down counting or event counting. The defining parameters include amplitude or

peak height (in volts), threshold (an AE event is only recorded when it exceeds a certain amplitude), rise time (the distance between the rising edge of a wave/peak and the apex), and the AE count (the number of waves above the threshold). Clearly, the number of 'counts' is determined by the threshold employed and the frequency of data acquisition. The duration of an AE event is defined as the period between the rising edge of the first peak and the falling edge of the last peak. Additionally, the area under a single burst can be used to quantify the amount of energy released.
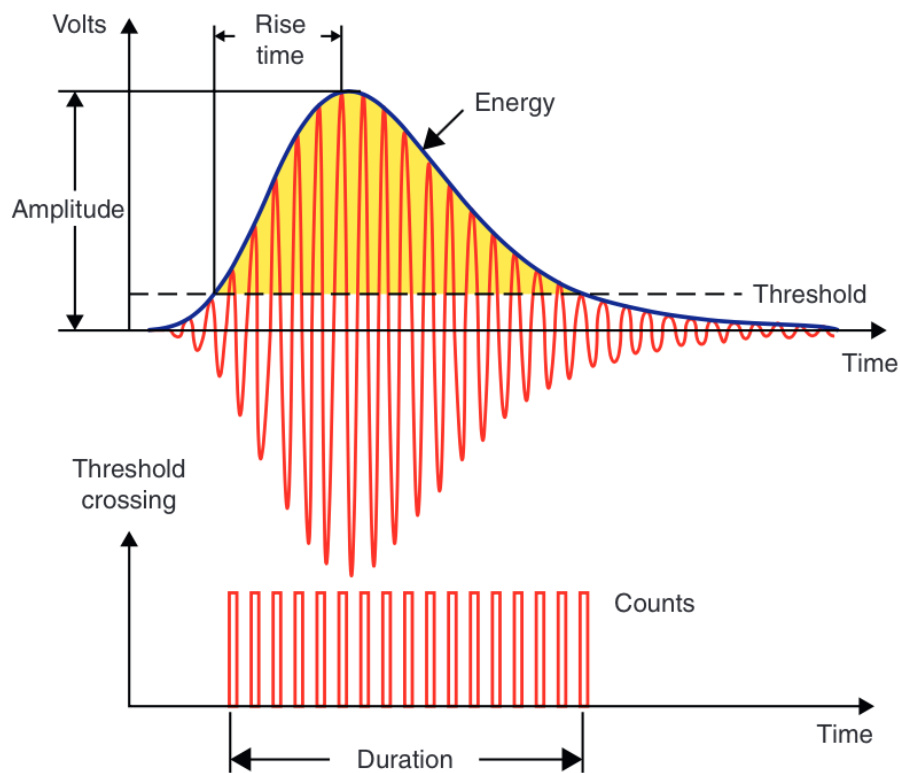
Figure 11. A typical ring-down counting of an acoustic emission signal and its associated parameters (Nair & Cai, 2010).

Since the AE signals generated from any wear process are generally stochastic (having a random probability distribution or pattern that can be analyzed statistically) in nature, statistical methods are often applied for their analysis (Mukhopadhyay, Jayakumar, Baldev, & Venugopal, 2012). Commonly, a distribution is described by its mean and variance which are the first and

second moments, respectively. The third standardized moment, skewness, is a measure of the asymmetry of the probability distribution assuming a unimodal distribution. In another word, it indicates how much a distribution deviates from the normal distribution, which has a skewness of 0. The fourth moment, kurtosis, describes the shape of a distribution. A high kurtosis distribution has a sharper peak and longer fatter tails, and a low kurtosis distribution has a more rounded peak and thinner tails.

Kannatey-Asibu Jr. and Dornfield carried out the pioneering work on applying a β distribution to the analysis of AE data obtained from tool wear monitoring and observed that skewness and kurtosis correlated with the process (Kannatey-Asibu Jr & Dornfield, 1982). In the present work, AE burst data generated during the abrasive wear tests were evaluated by applying distribution moments based on an assumed β distribution.

The probability density function of AE RMS can be expressed as (Whitehouse, 1978):

$$\beta(m.n) = \int_0^1 x^{m-1}(1-x)^{n-1}dx \tag{20}$$

where m and n are parameters of the β distribution and the variable x represents AE energy, which is proportional to the integral of the square of the transducer output voltage (Wadley, Scruby, & Speak, 1980). The values of mean and variance are calculated first and then the values of skewness (S) and kurtosis (K) are calculated based on the moments of assumed β distribution of the measured AE signals (Mukhopadhyay, Jayakumar, Baldev, & Venugopal, 2012). Variance (σ^2) and the standard deviation (std) are given by the following equations, respectively:

$$\sigma^2 = \frac{1}{n-1} \cdot \sum_{i=1}^{n}(x_i - \mu)^2 \tag{21}$$

$$std = \sqrt{\sigma^2} \tag{22}$$

where x_i is the instantaneous AE energy, μ is the mean, and n is the sample size. Parameters m and n of the β distribution can be calculated from the mean and the variance:

$$m = \mu \cdot \frac{(\mu - \mu^2 - \sigma^2)}{\sigma^2} \tag{23}$$

$$n = (1 - \mu) \cdot \frac{(\mu - \mu^2 - \sigma^2)}{\sigma^2} \tag{24}$$

Furthermore, the values of skewness, and kurtosis, can be calculated from m and n by:

$$S = \frac{2(n - m)\sqrt{(m + n + 1)}}{(m + n + 2)\sqrt{mn}} \tag{25}$$

$$K = \frac{6[(m - n)^2(m + n + 1) - mn(m + n + 2)]}{mn(m + n + 2)(m + n + 3)} \tag{26}$$

The mean of the AE RMS distribution is used to describe the location of a distribution and the variance indicates its spread. As previously mentioned, the skewness is a measure of symmetry around the mean, whereas the kurtosis indicates the sharpness of a peak. A positive S value generally indicates a shift in the bulk of the distribution to the right of the mean, whereas a negative S indicates a shift to the left.

4. Corrosion Sensing

The most commonly used techniques for monitoring pipeline corrosion are mass loss coupons, electrical resistance probes, linear polarization probes, and ultrasonics (Powell, 2015).

Corrosion consists of electrochemical reactions at the interface between a metal and an electrolyte solution. An electrochemical reaction can be considered as two half reactions taking place at the anode and the cathode, respectively: at the anode, a metal releases electrons and is oxidized; at the cathode, a counter electrode is reduced by gaining electrons. Two parameters can be measured in such a reaction: the corrosion current, I_{corr}, which defines the corrosion rate and the open circuit potential, and E_{corr}, which defines the probability of corrosion. In electrochemical measurements, a cell is comprised of a working electrode (the corroding metal), a counter electrode, a reference electrode, and electrolyte. All electrodes are connected to a potentiostat, which controls the potentials being applied onto the electrodes and measures the resultant current as a function of potential. The process of changing the potential is known as 'polarization' (Poursaee, 2014).

Linear polarization resistance (LPR) measurements are performed by applying a potential in the range of ±10 mV about the E_{corr} as either a constant pulse(potentiostatic) or a potential sweep (potentiodynamic) and measuring the current response (Poursaee, 2014). Alternatively, a current pulse (galvanostatic) or a current sweep (galvanodynamic) can be applied, and potential response is measured. The measurand in LPR technique is the polarization resistance, R_p, defined as the resistance of the material to oxidation while an external potential is applied. R_p represents the slope in the plot of the relationship between potential and current in the open circuit (Figure 12). It is calculated as

$$R_p = \frac{\Delta E}{\Delta I} \qquad (27)$$

where ΔE is change in potential and ΔI is the change in current. The Stern-Geary equation correlates corrosion current to R_p (Stern & Geary, 1957)

$$I_{corr} = \frac{B}{R_p} \qquad (28)$$

30

$$B = \frac{\beta_a \beta_c}{2.3(\beta_a + \beta_c)} \tag{29}$$

B is the Stern-Geary constant, and β_a and β_c are the anodic and cathodic Tafel constants, respectively. The value of B is determined empirically. The corrosion current density, i_{corr}, can be calculated by dividing i_{corr} by the surface area of the polarized area.

$$i_{corr} = \frac{B}{R_p A} \tag{30}$$
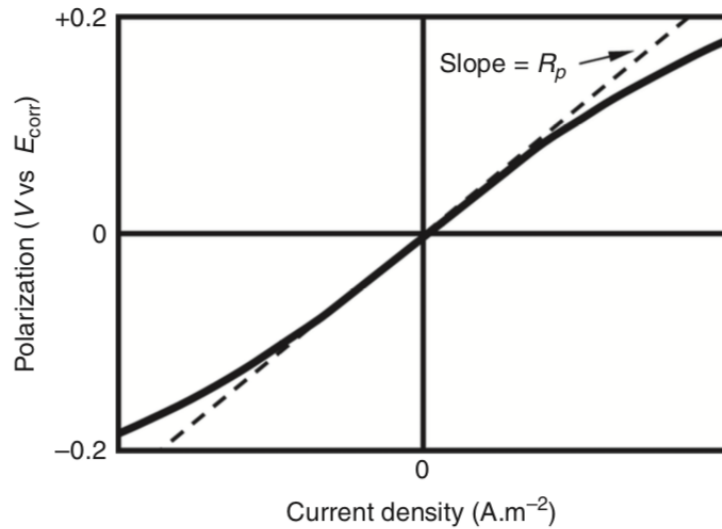
Figure 12. Schematic illustration of the linear polarization curve (Poursaee, 2014).

In summary, LPR is a nondestructive way to test corrosion rate in a material. The system measures the polarization resistance of the material which is inversely proportional to the corrosion rate (Scully, 2000). This technology was successfully used by Huang et. all. in 2016 to measure localized corrosion caused by under deposit in API X65 carbon steel pipeline. This

method can be a good corrosion wear monitoring tool for the beginning of the pipeline where high rate of corrosion is expected.

LPR uses direct current (DC) to perturb the equilibrium of the interface between the metal and electrolyte solution, where the ohmic drop due to the uncompensated resistance (Ru) of the solution and the connecting cables are ignored. The effects of Ru can cause severe distortions of the linear polarization curve, leading to erroneous estimation of corrosion rates (Hernández, et al., 2019). Given this limitation, electrochemical impedance spectroscopy (EIS) that uses a small amplitude of alternating current (AC) in a certain frequency domain has become a more popular corrosion sensing technique in the past decade. Typically, EIS data are collected through a potentiostat/galvanostat apparatus and fitted to an equivalent electrical circuit model for interpretation and analysis (Figure 13). The experimental EIS responses are then used to characterize corrosion mechanisms using Nyquist or Bode plots. Dues to its high measurement sensitivity, EIS can be used to evaluate the properties of thin oxide films formed on metals.
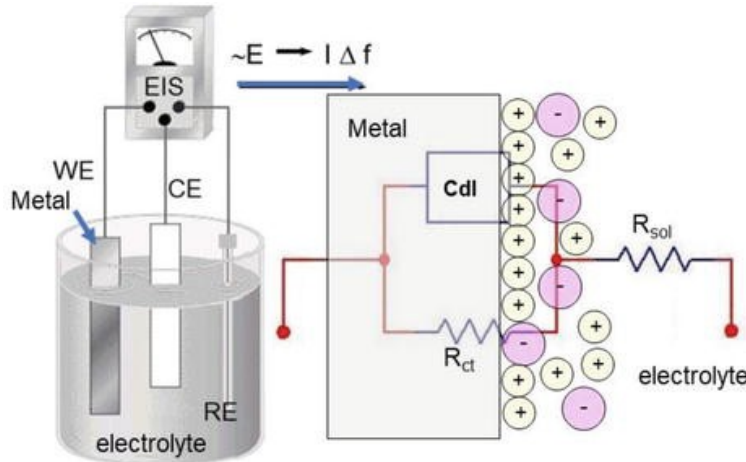
Figure 13 Representation of a corrosion cell and its equivalent electrical circuit (EEC). WE - working electrode, CE - counter electrode; RE - reference electrode (Hernández, et al., 2019).

Since all of the pipeline is affected by both erosion and corrosion, a system to monitor the combined effect of both erosion and corrosion is desired. Erosion-corrosion wear measurement techniques measure the overall wear of the pipe, without discerning the effect of either events. It is usual to use corrosion inhibiters when using these methods to study only the erosion

component of wear. Currently, two common pipe wear measurement techniques are: mass loss and ultrasound thickness measurement (Sadighian, 2016).

The first technique calculates pipe wear by measuring pipe mass loss during the course of testing or operation. Pipe weight is recorded before and after operation/test. The weight difference between the two measurements is taken as the overall mass loss due to wear from the sample pipe. This method is easy to implement in a laboratory setting since no specialized equipment is necessary. On the other hand, for real life applications it requires the pipes to be offline and often proves to be inconvenient even impractical.

Ultrasound thickness measurement is a widely used nondestructive test technique that utilizes high frequency sound waves in the range between 500 kHz and 20 MHz to measure the time a sound pulse takes to travel through the test piece and reflect back from the inside surface of the material [Nelligan, 2016]. Such a method is also known as the pulse-echo measurement. Specifically, a piezoelectric transducer is used to generate a sound wave and detect the reflected waveform by generating an electrical signal proportional to the magnitude of the pressure wave (Brunskill, Harper, & Lewis, 2015). Since the speed of a sound wave in a material is dependent on their acoustic impedance, which is affected by the density, wear can be detected by measuring the change in travel time of the reflected waveforms over time corresponding to the change in material thickness. The relationship between the thickness of the material, d, the speed of sound in a medium, v, and the transit time, t, can be expressed by the following equation:

$$d = {vt}/{2} \qquad (31)$$

And wear is characterized as:

$$\Delta d = {v\Delta t}/{2} \qquad (32)$$

The accuracy of wear measurement, Δd, is dependent on the accuracy of the measurement of change in transit time Δt. It was reported that Δt can be measured with an accuracy of 1 nanosecond, which is equivalent to a wear of 3 nm (Birring & Kwun, 1989).

This technique has the advantage of allowing online thickness characterization. However, environmental factors, such as curved pipe surface and changes in temperature which causes thermal expansion and compression, can generate inconsistencies in the readings. Additionally, the two types of existing ultrasonic thickness measurement devices, including portable gauges and permanently or semi-permanently installed ultrasonic transducers, each have their own limitations (O'Keefe, Maron, Fernald, Bailey, & Van der Spek, 2009). Portable ultrasonic devices can reliably measure pits with an error of ±0.25 mm and is capable of detecting the location of a defect or pit (Papavinasam, Doiron, Attard, & Demoz, 2012). It serves as an excellent tool for assessing the integrity of pipelines. However, it cannot offer the precision over a short period of time and requires site access to the pipes, resulting in inevitable labor costs. As permanently or semi-permanently installed ultrasonic transducers are mounted around the perimeter of a pipe, they eliminate the labor cost associated with portable gauges and enable remote monitoring of pipe wear (O'Keefe, Maron, Fernald, Bailey, & Van der Spek, 2009). However, each transducer requires an ultrasonic pulse receiver paired with an ultrasonic transducer for signal transmission and only allows for localized wear measurements. Resultantly, they are far from ideal to be used on long and complex pipeline systems.

Electronic calipers can be used to measure change in thickness of the pipe due to wear at specified locations. There are two main types of calipers, outside calipers and inside calipers. Outside calipers can be used to measure the thickness of the pipe wall by touching one leg of the caliper to the inside of the pipe and the other on the outside of the pipe. Inside calipers can be used to measure the inner diameter by touching both legs to opposing ends of the inside of the pipe. These measurements are easy to perform in a laboratory test setting and produce accurate localized wear measurements.

5. Particle Image Velocimetry

Particle Image Velocimetry (PIV) is a non-intrusive, optical visualization measurement technique used for studying fluid flows. PIV measures the velocity field of an entire region within the flow simultaneously (Atkins, 2016).

In order to use particle image velocimetry (PIV), a section of the slurry pipe has to be replaced by a clear acrylic pipe to allow for visual acquisition of slurry flow. PIV equipment is set up consisting of a high-speed camera, camera lens, synchronizer, and light source. The synchronizer times the light source flash and camera shutter to match to minimize blurring of the image.

The camera captures high resolution imagery which is then processed using PIV software. PIV software is used to compare changes between frames and vectorize particles based on their previous and current position. These vectors are used to understand the general flow within the pipe and can also be used to calculate the particle strike and sliding rate against the wall. The particle strike rate and sliding rate are then used to estimate the impact wear and the sliding wear, respectively.

The downside of this technique is that it can only be applied to flows with low concentration of particles which allows light to get through. Capture of high flow rates is limited by the shutter speed of the camera. The camera resolution limits the size of the particle that the equipment can recognize.

This technique is used to estimate wear instead of actual wear measurement. Proper equipment setup is costly and requires advanced knowledge of image processing. The benefit of this technique is that it allows a better understanding of the flow of particles within the pipe and assists the optimization of flow to minimize wear. In addition, particle image velocimetry can be used to estimate the damage to pipes by finding out the average velocity, direction and size of particles striking the wall of the pipe.

iv.   Laboratory Wear Testers

The wear rate of slurry pipeline depends upon factors such as slurry properties, slurry particle properties, flow properties, and pipeline wall properties. An all-inclusive engineering approach, where all factors involved in the wear process are studied, is too complicated to be solved analytically. Instead, most of the existing models evaluate only the effects of a few parameters.

This chapter review some of the laboratory testers developed to study abrasive wear, erosion and erosion-corrosion, respectively.

1. Abrasive Wear Testing

As defined previously, when coarse particles slide along the bottom of a pipeline, it causes abrasion. The American Society for Testing and Materials (ASTM) categorized this form of abrasive wear as 'low-stress abrasion', where the applied load is not sufficient to crush the abrasive. Low-stress abrasion if probably the most prevalent form of abrasive wear. A few examples are given below (Budinski, Abrasive Wear Testing, 2011).

a. Dry sand/rubber wheel tester

In this test setup, coarse sand is rubbed against the test material using a rubber wheel, which produces scratches on the specimens and removes chips of materials. Mass loss of the test material is test specimen is converted to a wear volume and used to characterize wear. Some concerns in using this test are:

- Obtaining the proper sand flow rate is challenging;
- The diameter and the hardness of the rubber wheel changes over time; and
- The mass loss may be too small to be measured accurately and correlated to wear behavior.

b. Loop abrasion test

To address the challenge faced with a harder specimen than sand, aluminum oxide abrasive looped around drive spindles is used to rub against a flat sample continuously for one-hour test time. Wear is calculated based on volume loss. Compared to the dry sand drum wheel tester, the loop tester results in less mass loss (considering the test material is likely to be harder). However, material ranking correlates.

Low-stress abrasion is characterized by scratching of a surface by hard particles or sharp protuberances. Depending on the hardness and size of the test specimens, harder abrasives then

aluminum oxide or sand (for instance, diamond indenters) and different setups apart from two testers mentioned above have been developed. There are literally hundreds of tests reported. However, the purpose of this review is not to create an exhaustive list of existing devices, but to illustrate the general mechanical engineering design principles. To summarize, an abrasive wear test generally falls into one of the following categories (Figure 14):

- Three-body abrasion tests (hard particles trapped between two sliding surfaces), such as disk vs. disk and dry sand/rubber wheel

- Two body abrasion tests (hard particles run against a softer surface), such as bonded abrasive test and taber
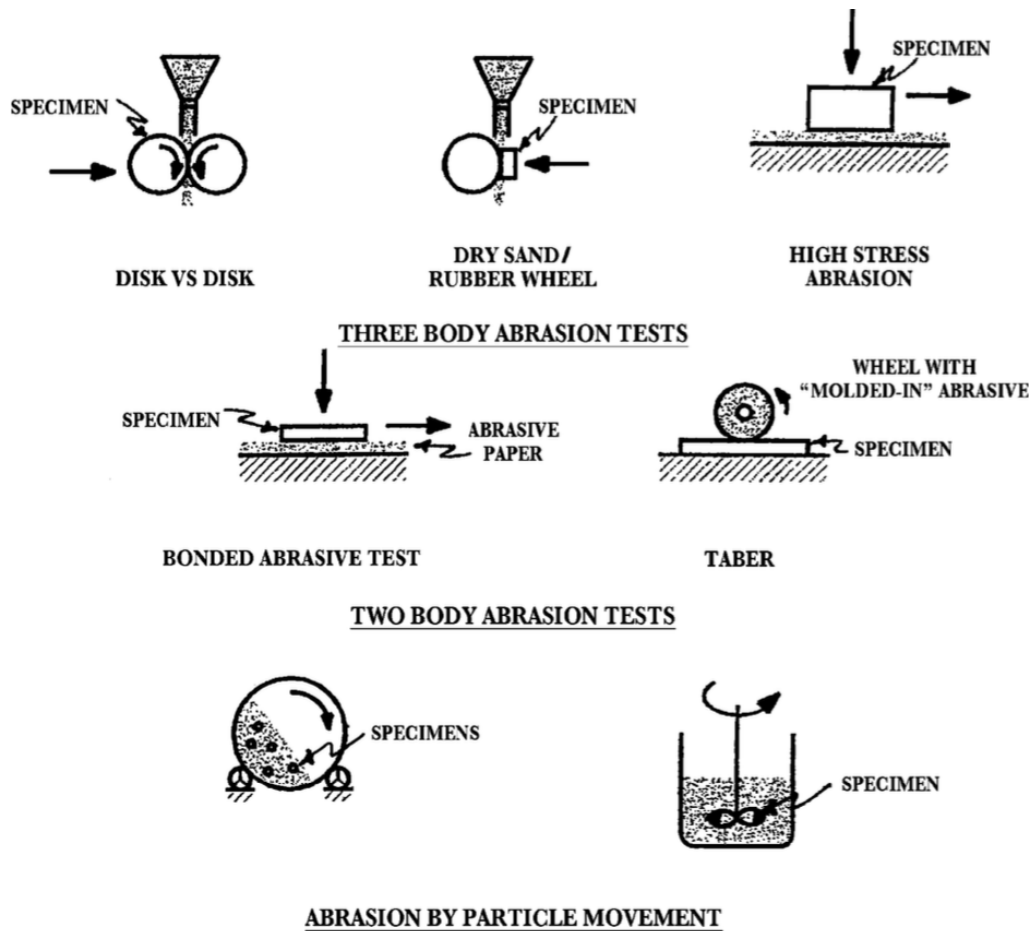
- Abrasion by particle movement

Figure 14. Common abrasion tests (Budinski, Abrasive Wear Testing, 2011).

2. Erosion Wear Testing

Merriam-webster defines 'erode' as to wear away by the action of water, wind or glacial ice (Merriam-Webster, n.d.). The difference between abrasion and erosion is that there is a fluid component involved in the mechanical action that produces wear. In other words, 'wet abrasion' is really erosion and often times, there is a chemical component (dissolution) to the material removal mechanism. Furthermore, if the fluid is corrosive to the material being eroded, then there will a contribution from corrosion. The effect is known collectively as erosion-corrosion. Slurries erode by the action of abrasive particles in the liquid that come into contact with pumps and pipeline systems. A variety of standard ASTM slurry erosion tests (Budinski, Erosion Testing, 2011) are illustrated in Figure 15 below. Namely, they include:

- **Miller number test** (Miller & Schmidt, 1987). This test simulates erosion in a reciprocating pump. A flat test specimen reciprocates on a rubber lap immersed in a slurry. Two parameters, including slurry abrasivity (Miller number) and slurry abrasion response (SAR number) are determined for different slurries and materials. A combination of mass loss measurement, profilometry and scanning electron microscopy can be used to analyze the wear mechanism.

- **Wet sand test**. Similar to the dry sand/rubber wheel test mentioned in the previous section, except here the sand is wet. More specifically, test specimens are forced against a rubber wheel, with a force of 50 lbs for 1000 revolutions in a slurry of 50 to 70 mesh silica and water. Wear is measured as a function of volume loss and rubber hardness (Budinski, Erosion Testing, 2011).

- **Propeller test**. This test simulates erosion that would occur on an impeller in a rotary pump or pump casing. A test specimen is affixed to the tip of a propeller and rotated while immersed in a slurry. Due to the velocity gradient towards the centerline, the microscopic nature of particle strikes at different angles and velocities can be investigated. Additionally,

synergism between wear and corrosion can be studied using potentiodynamic polarization techniques.

- **Ball cratering test**. A rotating steel ball (approximately one inch in diameter) is rotated against a flat test specimen and a slurry is fed through the contact region. Volume loss is used to characterize wear. The results depend on the sphericity and surface texture of the ball and the properties of the slurry.

- **Slurry pot test**. Originally designed by Tsai et.al. to test erosion on steel alloys by coal and silicon carbide suspension in kerosene (Tsai, Humphrey, Cornet, & Levy, 1981). The slurry pot tester is used to conduct accelerated erosion condition testing. This tester consists of an enclosed container with a rotating mixer that excites the slurry fluid and suspends abrasive particles, clamps to hold the test specimen so that the flow is perpendicular to the axis of specimen, and a rotating shaft to turn the specimen in the slurry. Temperature is kept constant by using both electric blanket heating and cooling coil with coolant flow. To inhibit the corrosion effect of air and humidity, nitrogen gas was injected into the tester. Particle concentration, mean particle size, speed of rotation, and temperature can be varied to study the erosive effect on different types of metal through weight loss measurements. This type of tester does not allow the constant replacement of slurry, making it susceptible to possible wear particle degradation.

- **Orifice enlargement**. This simple test measures the resistance of a material to wear by pumping slurry through an orifice made from the candidate material. The method is not widely used, limited by the cost of a slurry pump and the availability of orifices made of the specific materials of interest.
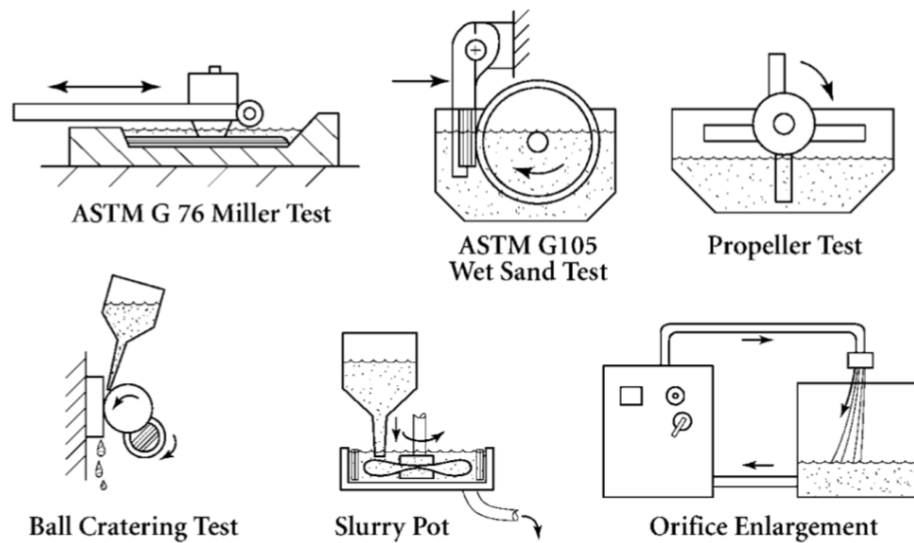
Figure 15. ASTM standard slurry erosion tests (Budinski, Erosion Testing, 2011).

Apart from the standard ASTM testing methods, other lab-scale slurry erosive wear has been developed, the most popular ones include:

- **Jet erosion tester**. A jet erosion tester ejects fluid on a testing surface using a pump. The slurry can then be circulated and reused, or a set amount of new fluid can be set to eject instead. The recirculation of fluid can lead to decreased particle size over the run time. The angle of the jet can be adjusted to match the expected wear angle at different location of the pipe by changing the angle that the test surface is held. These different wear angles can be caused by curves and elbows in the pipes that would change the direction of the slurry fluid. The expected angle of wear can be estimated by running computational fluid dynamics (CFD) analysis. Particle size and concentration can be varied to match the slurry flow conditions at different locations of the pipe. Locations closer to the start of the pipeline will have bigger particles, while locations closer to the end of pipeline will have smaller particles. The velocity of the fluid can also vary inside the pipeline due to changes in the dimension of the pipe and changes in flow rate. This change in velocity can also be replicated in a slurry jet erosion tester by increasing or decreasing the speed of the pump. Testing can be done either to test piece failure or a set time. Testing to failure helps determine the estimated time to failure, while tests based on time help determine the average rate of wear. Testing

to failure is not recommended due to the difficulty of determining exact time of failure, and the longer duration of testing. Testing using specific testing durations when combined with mass loss measurements converted to volume loss are a good estimate of wear rate and can help estimate time to failure.

- **Coriolis slurry erosion tester**. This approach has been developed and increasingly used since the 1980s (Tian, Addie, & Barsh, 2007). It was originally developed by Tuzson et al. (Tuzson & Scheibe-Powell, 1984) (Tuzson J. , 1984), designed primarily for sliding erosive wear with some effect of low angle impact. A typical Coriolis slurry erosion tester consists of slurry feed or feed-circulation system and center rotation unit equipped with specimen holders that are built into each slurry flow channel. During a wear test, slurry flows and slides against the test specimen surface under centrifugal and Coriolis effect, generating wear on the surface. Erosive wear is measured by mass loss and/or profilometry of the surface. Flow rate, particle size and test duration vary significantly among the developed Coriolis testers, depending on the specific design and the properties of the test materials (Pagalthivarthi & Helmly, 1992).

3. Erosion-Corrosion Testing

Most of the abrasive wear testing and erosion testing are short-termed, often a few hours in duration (Budinski, Erosion Testing, 2011). Since corrosion takes time, erosion-corrosion testing normally requires longer time. In one erosion-corrosion test, test specimens are mounted on a plastic disk, immersed in a slurry, and rubbed against a dead weighted rider. The rubbed portion of the materials will develop a scar over a period of 30 days. A comparison is made between the rubbed and unrubbed area.

Although temperature or electrical resistance of interfaces as well as surface composition changes can be measured by the sensing techniques discussed in this chapter, difficulty in interpretation of the experimental results and the limited resolution in measurements can hinder the local description of material behavior. In addition, many of the existing abrasive wear testers

rely on either volume loss, mass loss or surface roughness characterization to characterize wear processes. Compared to these tools that measure solely the integrated outcome of different wear modes, acoustic emission studies continuously monitor wear and, thus, are an attractive possibility for understanding fundamental wear behaviors and discovering critical transitions to help identify failure. There is a need for controlled wear testing conditions to investigate how AE features might manifest during damage events. Based on the hypothesis that the AE signal patterns are uniquely correlated to material properties, this study aimed to develop a tester and utilize mass/volume loss and AE measurements to characterize the wear behavior of three types of materials.

III.   Experimental Method

This section discusses the design and development of the apparatus and method of measurement to evaluate acoustic emissions for measuring damage due to abrasive wear under laboratory conditions.
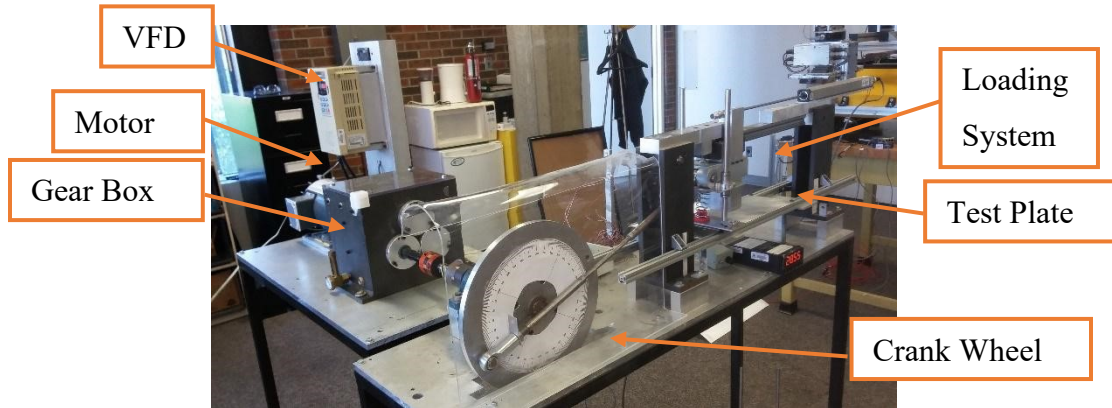

Figure 16. Photograph of the wear testing apparatus.

i.   Design of Experiments and Test Methods

This study was designed to evaluate the effect on observability of wear using acoustic emission techniques due to variation of three main parameters that can affect slurry erosion on inner pipeline walls: 1) material properties, 2) normal force; and 3) lubrication conditions. Materials with different hardness, elasticity and densities were chosen, including aluminum, austenitic stainless steel, and polyurethane-coated aluminum. Among these three types of materials, aluminum represents a common soft metal; steel has the highest hardness and tensile stiffness among common metals and polyurethane, have been reported to provide erosion insurance to a wide range of structures including pipeline (Aravind, Jacob, & Mohamed, 2017).   Flat specimens (rectangular plates) of the above-mentioned materials were utilized, instead of other geometries such as tubular shapes, to maintain the application of consistent normal forces during the experiments. The dimensions (43.18 cm x 13.97 cm) of the flat specimens were selected so that the full range of motion of the apparatus (described in the next section) can be

accommodated. Additionally, the thicknesses of the specimens were limited by the weighing capacity of the analytical balance (American Weigh SC-501) used to determine mass loss due to wear.

The test method was designed to simulate the rubbing of inner pipeline wall by slurry particles, simplified by omitting the corrosive environments. It specifically determined single-particle abrasive wear of three types of materials using a linear, reciprocating ball-on-flat test specimen setup. The direction of the relative motion between sliding surfaces reversed in a periodic fashion such that a ball slid on a test plate back and forth and in a straight line. A normal load was applied vertically downward through the ball against the horizontally mounted test plates, selected from one of three levels (low, high, medium). The test method encompassed both unlubricated and lubricated testing conditions. During an experiment, signals of acoustic emission due to friction were acquired. In addition, test specimens were weighted before and after an experiment and mass loss was determined from the measurements and further converted to volume loss. Both acoustic emission and mass loss were used to characterize different conditions.

ii.   Apparatus

General description. The single-particle abrasive wear tester was set up in an enclosed lab space with regulated temperature (23.3 °C) and humidity (42.5%). Figure 16 displays the major components of the apparatus: a variable frequency motor drive unit (VFD), a motor, a gear box, a crank wheel, a loading system, and a test plate. The VFD supplied power to the system and controls the motor. The motor (frequency 5 Hz) was connected to a gearbox with a 1: 3.33 ratio to increase the torque output. The gearbox output shaft was connected to the input shaft of a crank wheel. The crank wheel arm connected to the loading system, converting angular motion to reciprocating, linear motion shown in Figure 16. A spherical, stainless steel (austenitic 304) ball was rigidly mounted on the loading system and moved back and forth across the surface of a fixed test plate. A load was applied to the contact between the ball and the plate. The plate

was tested dry, immersed in a water bath, or sprayed with a thin film of lubricant (heavy duty silicone lubricant, CRC Industries)

Figure 17. Illustration of stroke length.
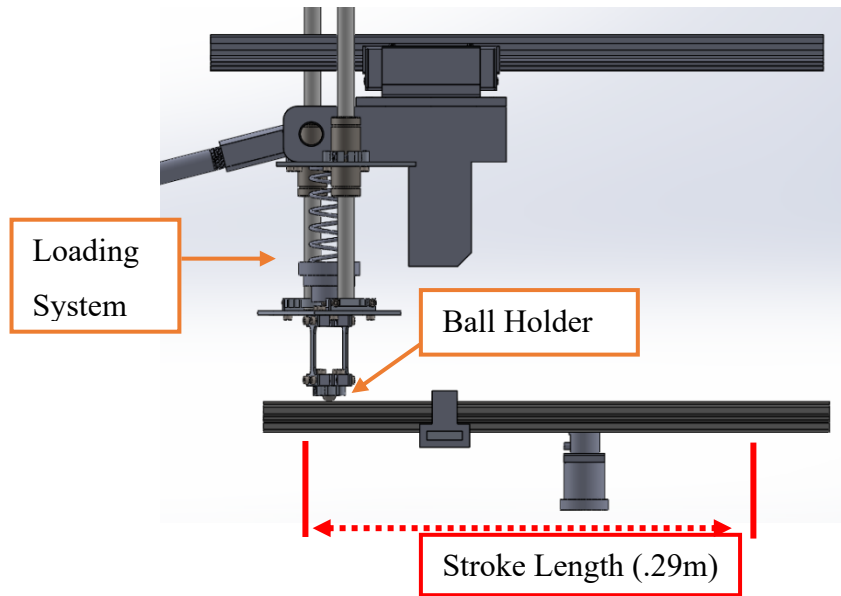
Motion drive. One full rotation of the crank wheel resulted in one cycle of linear, reciprocating sliding of the ball (2 × stroke length, see Figure 17). The frequency of oscillation and the total distance traveled by the ball across a test specimen was monitored using a potentiometer during each test. Uncertainties in set-up and measurements will be discussed in chapter IV.
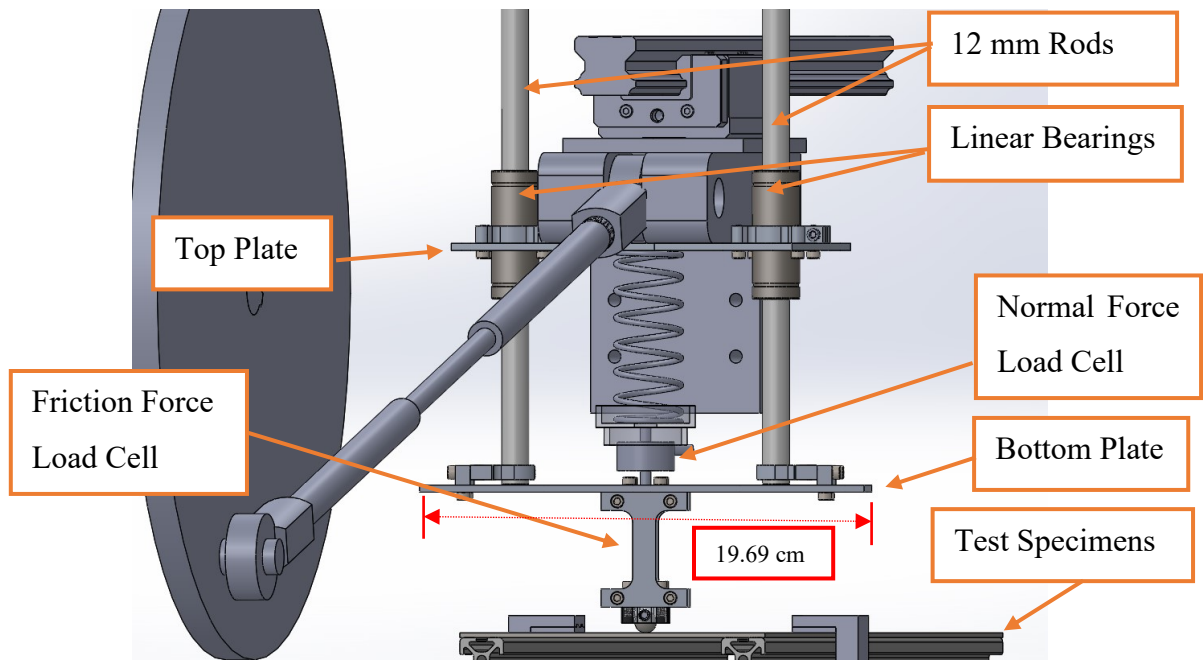
Figure 18. Illustration of the loading system components.

Loading system. As shown in Figure 18 above, the loading system assembly was held in place by two 12-mm steel rods, which were affixed to the bottom plate by clamps and placed inside two linear bearings clamped to the top plate. The provision of linear ball bearings ensured the normal load to be transferred vertically from the spring load to the bottom plate and then to the contact between the ball and the test plate. The spring selected was 7.62 cm long with a spring rate of 100 kPa and a maximum load of 14.52 kg. The spring holder holds the spring in place on top of the tension-compression load cell (for normal force measurement) attached to the bottom plate. Beneath the bottom plate, the friction force load cell was utilized to capture longitudinal strains as the ball moved back and forth on a test plate. The bottom of the friction load cell was connected to the ball bearing clamp, which holds a stainless-steel ball (.95 cm in diameter) tightly in place and prevents slippage during the test. The strain gauges in both load cells were arranged in a Wheatstone bridge configuration (not illustrated).
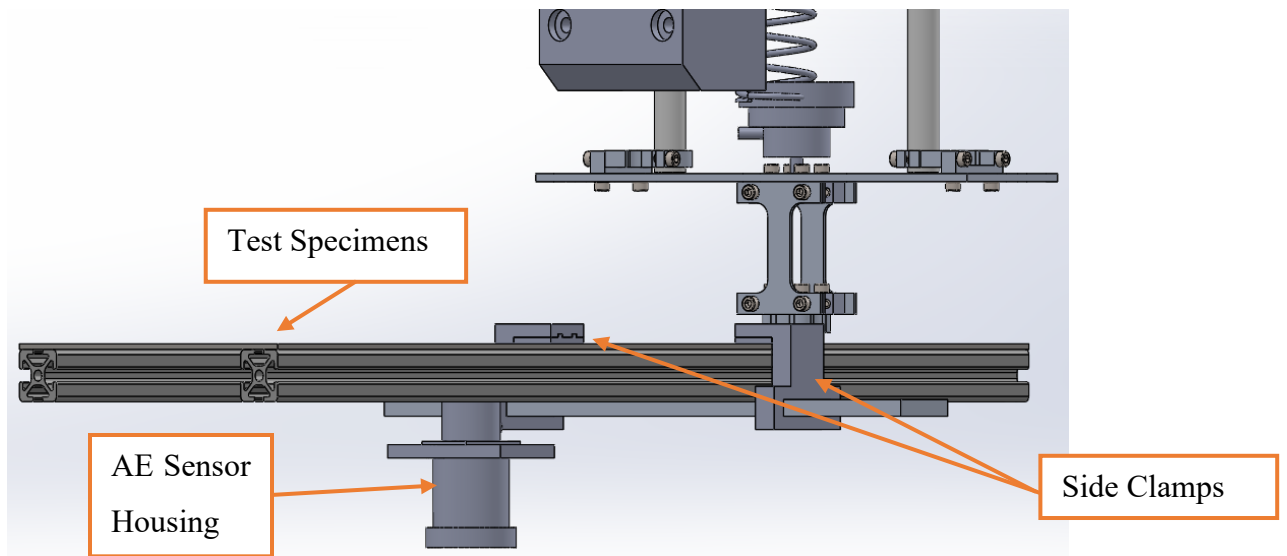
Figure 19. Illustration of the test specimen holder.

Test specimen holder. Under loading system, a test plate specimen was supported by two aluminum t-slotted rails on two parallel sides and secured with two side clamps. The height of the t-slotted rails was adjusted using two height adjustment platforms (not shown) placed below, which allowed replacement of both the ball and the plate. An acoustic emission sensor was attached directly to the bottom of the test plates using a custom designed spring-loaded AE sensor housing. The AE sensor housing was placed in the middle of the test plate in line with the abrasive particle line of travel. The AE sensor housing and AE sensor are described below.
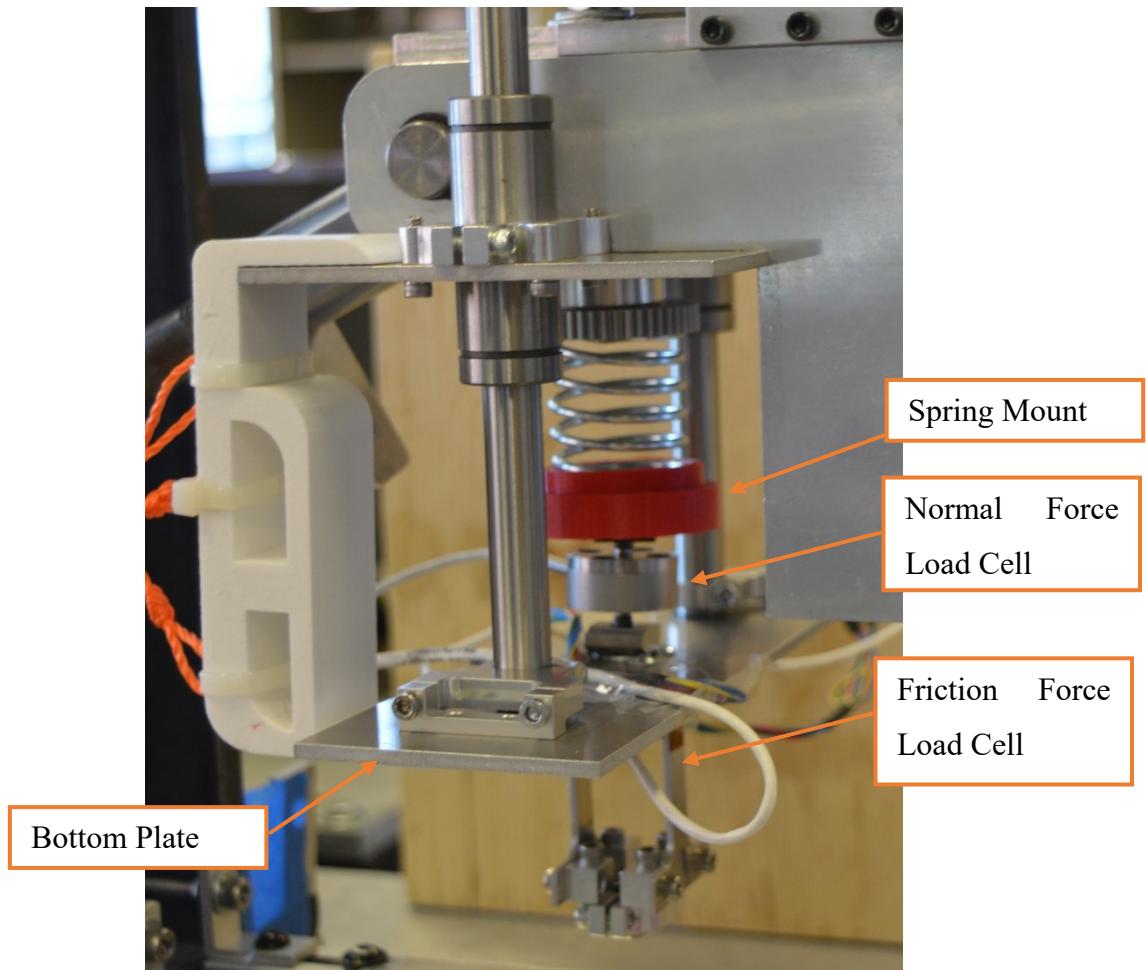
Figure 20. Photograph displaying the components and connections in the mechanical design.

Normal force load cell. An OMEGA LC202-300 load cell was used to measure normal forces. At the top, the compressive arm of the load cell was connected to a 3D-printed spring mount (red-colored part in Figure 20) via a flat surface nut attached to the bottom of the mount. There was a 4 mm space between the nut and the active side of the load cell. A second flat surface nut affixed the other end of compressive arm to the bottom plate of the bottom plate, leaving a 4 mm space between the inactive side of the load cell and the nut. The load cell wiring was carefully guided to the side in order to avoid interferences in the load application process and allow full movement of the loading system. The LC202-300 load cell had a maximum load capacity of 136 kg (1334 N) with 0.25 % accuracy.

Acoustic emission sensor. The acoustic emission sensor used was the Mistras R15a narrow band resonant sensor with peak sensitivity of 80 dB.

Acoustic emission sensor housing. Since secure AE sensor-plate contact was the key to accurate and reproducible AE signal acquisition, a sensor housing was designed. The housing was mounted to the t-slotted rails with the sensor at its center. A spring in the housing pushes the AE sensor gently upward. securing the sensor in contact with the test plate.

iii.   Instrumentation System

1. Sensing Techniques and Data Acquisition

Electrical sensors were used to measure displacement, force, and acoustic emissions. Displacement was measured using an Omega LP801-300 long-stroke linear potentiometer with the NI9219 acquisition module. Two sets of four strain gauges in Wheatstone Bridge arrangement with a NI 9236 acquisition module were used to measure applied normal forces and friction forces, respectively. One acoustic sensor, Mistras R15a, was used to acquire the acoustic emission generated by the ball-on-plate sliding. LabWindows and Mistras AEwin software was used for data acquisition and MATLAB was used for data analysis (see Figure 21 below).
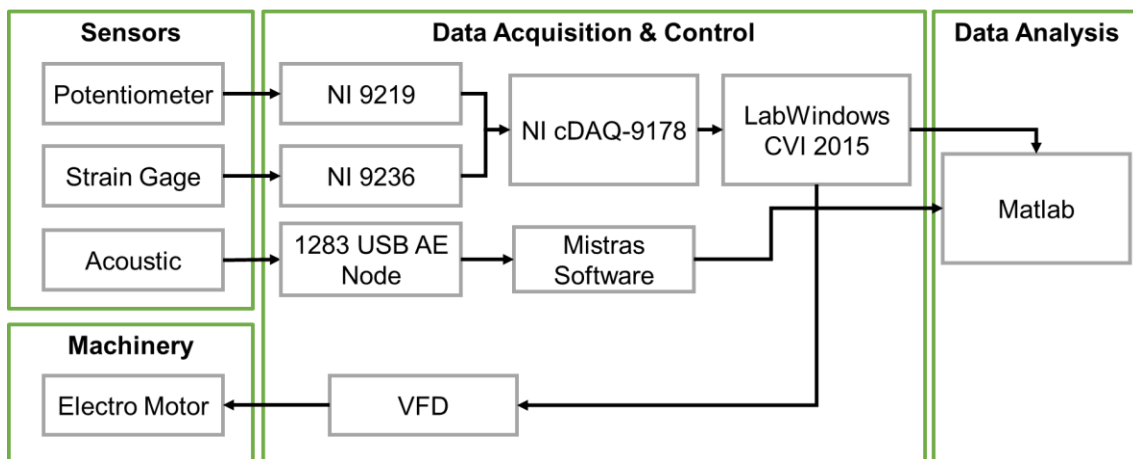
Figure 21. Diagram of sensors, data acquisition and data processing system.

As the ball moves back and forth on a test plate, the direction of the friction forces change rapidly. In order to follow these changes at high frequencies of reciprocation and accurately measure friction force, a sensitive and fast data acquisition system was designed capable of acquiring AE data at 10 MHz. The inclusion of a NI cDAQ-9178 module, with an input FIFO that can store 127 samples per slot, had the advantages of easy integration and synchronized sensing. In other words, the workflow design allowed the operator to control a multiplex of sensors (both potentiometer and strain gauges) and develop data acquisition programs with ease. For acoustic emission sensing, multiple acoustic sensors and software packages were considered. The final selection was based on consideration of their maximum acquisition rate, sensitivity, size and cost. Since the acoustic signature of ball-on-plate wear testing was unknown beforehand, the frequency range was estimated. Also, since testing is lab scale, the acoustic sensors needed to have a size and shape appropriate for attachment to the test specimens. All factors considered, MISTRAS USB AE node system was chosen due to high acquisition frequency, ease of use, and affordability. The R15a AE sensor was chosen for its peak sensitivity of 80-dB.

2. Measurements

(1) Friction force. Friction force was measured using strain gauges attached to a friction force load cell. The strain gauges were arranged in a full Wheatstone Bridge configuration to automatically compensate for changes in temperature.

(2) Test duration. The total sliding distance of a ball across a test plate was computed based on the voltage output of a potentiometer, using the following equation:

$$X = 2 \times L \times N \tag{33}$$

where

X = total sliding distance of the ball, m

L = stroke length. In this study, it remains constant at 0.29 m

N = peak count determined from a linear potentiometer output signal using MATLAB software

(3) Mass loss. Each test specimen was cleaned and weighed before and after a testing. (see Chapter III.vi.2. Test Material Preparation for details) Mass loss was calculated as:

$$Mass\ Loss = m_{before} - m_{after} \tag{34}$$

(4) Acoustic emission. Acoustic emission was captured at a frequency of 10 MHz using a single narrow band resonant piezoelectric transducer (R15a). The signal was pre-amplified via an internal low noise preamplifier as part of the Mistras 1283 USB AE node and then processed using Mistras AEwin software to output high frequency burst files at 10 MHz and root-mean-square (RMS) at 50 Hz. Data acquisition per cycle can be calculated using the motor frequency (5 Hz) and the gear ratio (3.33) resulting in acquisition of 33.3 samples per cycle.

iv.   Calibration

Two components of the apparatus were calibrated prior to use, including (1) the loading system and (2) the friction force sensor. The calibration results should ensure that both load cells were accurate and operating properly within the range of operation conditions. Data acquisition was performed using LabWindows software and data postprocessing using MATLAB.

1. Loading System Calibration

The load (normal force) applied on the specimen was checked periodically. Since the machine utilized a spring arrangement to apply the load, the calibration was done by disconnecting the normal force load cell from the assembly and checking its strain voltage output with reference weights placed on the top of the cell (where it connected with the spring).

The OMEGA LC202-300 load cell had a maximum load capacity of 135 kg (1334 N) with 0.25 % accuracy. In this study, three levels of normal force (or applied load): low (9.8 N), medium (14.7N) and high (19.6 N) were used to study wear. A four-point calibration at 0, 9.8, 14.7 and 19.6 N (using 0, 1, 1.5 and 2 kg reference weights, respectively) were performed with duplicate measurements at each point. One thousand-point moving averages were obtained for data smoothing to determine the average strain voltage, which was plotted against applied load using MATLAB and resulted in the following correlation:

$$Normal\ Force = \frac{Normal\ Strain + 7.085e^{-06}}{1.229e^{-06}} + 7.611 \tag{35}$$

It should be noted that, with the loading system assembled, the total applied load on the ball-plate contact was the sum of the weight of the loading system (775.83 g or 7.611 N) above the spring and the applied normal force via the spring and hence, the constant of 7.611 in the equation above.
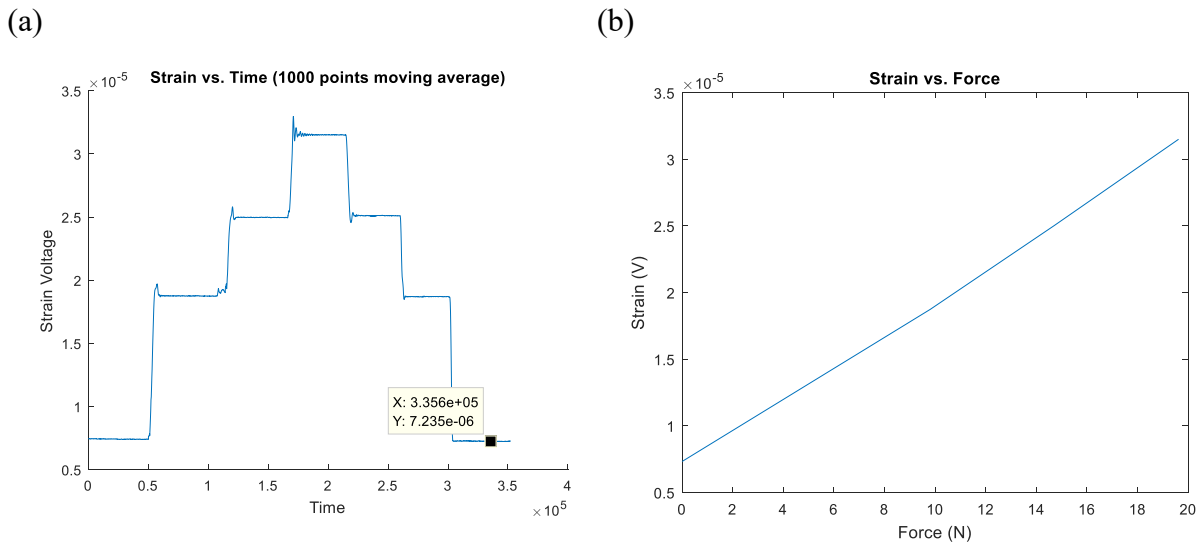
(a)

(b)

Figure 22. Normal force calibration. (a) Moving average curve for strain measurement; (b) Strain vs. Force plot.

2. Friction Force Sensor Calibration

The friction force sensor outputs shear strain measurement in volts. The relationship between shear strain and friction force was determined using a set of reference weights with known masses.

To calibrate both tension and compression forces, the load cell was disconnected from the assembly, placed on its side to rest on both arms and calibrated, respectively. More specifically, first, with the load cell lying on one arm, three reference weights at 909.9, 1909.9 and 2409.9 g were placed on the ball specimen holder, consecutively and the strain voltage readings were recorded. Then, the load cell was flipped and placed on the other arm and measurements were repeated using the same set of weights (909.9, 1909.9 and 2409.9 g) as above. This, in effect, resulted in a seven-point calibration at -23.64, -18.74, -8.93, 0, 8.93, 18.74 and 23.64 N.

The relationship between applied load and voltage output was examined by data analysis using MATLAB. More specifically, 200-point moving averages were obtained for data smoothing to determine the average strain voltages at each applied load. The polyfit function in MATLAB was used to compute the relationship between shear strain and friction force (simulated using reference weights). Linear regression predicted the strain-friction force relationship as below (see Figure 23).

$$Friction\ Force = \frac{Shear\ Strain - 6.369e^{-5}}{2.013e^{-5}} \tag{36}$$

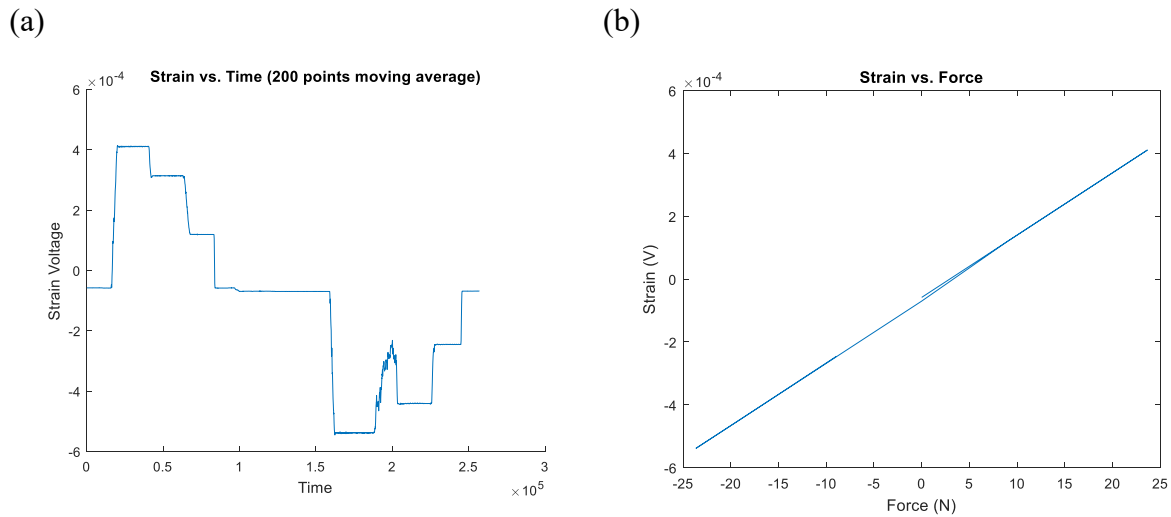(a)   (b)

Figure 23. Friction force calibration (a) Moving average curve for strain measurement; (b) Strain vs. Force plot.

v.   Control and Data Analysis Software

1. LabWindows

National Instrument cDAQ was used as the data acquisition system and LabWindows as the control software. A user interface was created in LabWindows to define sensor properties, specify acquisition frequency and control timing (Figure 24). It was expected that a large amount of high frequency sensor data would be generated during testing, and so significant effort was dedicated to improving data acquisition and storage speed. Four different data formats were considered, including American Standard Code for Information Interchange (ASCII), Binary files, Extensible Markup Language (XML) files and Technical Data Management Streaming (TDMS) files. Their advantages and disadvantages are explained as below.
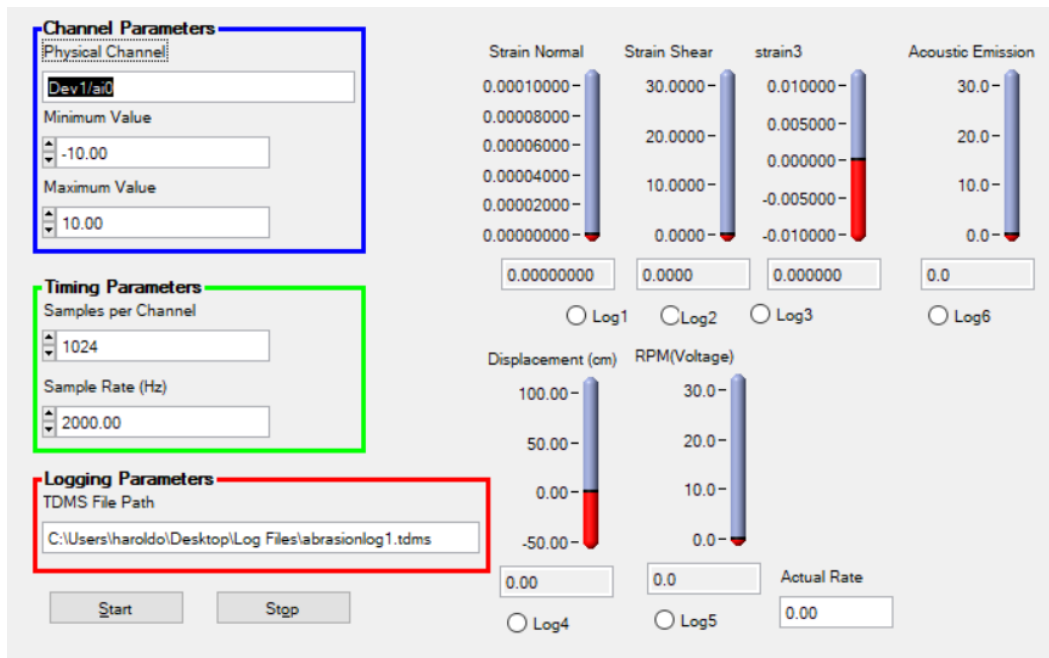
Figure 24. Designed user interface for software control.

Theoretically, ASCII can be opened in most common software applications without the need of specialized plug-ins, making it easy to work with across different platforms. However, this format requires a large memory allocation for saved data and is susceptible to data loss, due to limited writing speed which cannot keep up with the acquisition speed of the system (Comparing Common File I/O and Data Storage Approaches, 2019). Binary files are very efficient at writing data to disk with high writing speeds, allowing the data acquisition for high-frequency, high-channel count and real-time applications. The downside is that it is not human-readable and requires special applications for reading the data. XML data can be used to store data and their formatting. However, its large footprint and inability to write directly to disk makes it ineligible for the testing in this study. TDMS is binary based, allowing large files to be saved in small spaces while maintaining high data writing speeds. This file type contains descriptive header information within the files. A plug-in can be used to open the file format in common applications such as Microsoft Excel.

Empirically, due to the high acquisition frequency of the system, ASCII proved to be unsuccessful in acquiring uncorrupted data set at high frequency for all channels. The system

was re-programmed to acquire and save data in TDMS. The TDMS file format was successful in acquiring all channels at the desired acquisition frequency.

2. AEwin

Since the acoustic sensor was connected to a separate USB node, a different software was used to control it. Mistras AEwin software was adopted for its ease of communication with both the USB node and the acoustic emission sensor. The desired parameters, such as acquisition frequency, of acoustic emission acquisition were set within the software. Acoustic emission data summary data including time, root mean square (RMS), average signal level (ASL), threshold (THR), and absolute energy (ABS-ENERGY) was acquired, processed and saved in ASCII text-formatted data (.txt). High speed burst data was acquired and saved as comma separated value (.csv) format using hit-based triggering.

3. Data Analysis Software

Three software were used to process and analyze data: Microsoft Excel, RStudio Desktop and MathWorks MATLAB.

Microsoft Excel was used for data preprocessing, which involved 1) adding run information to files to enable identification following their import into a different environment and 2) converting files from .tpms format to .csv format to facilitate data import into more powerful data analysis software. For file conversion, the National Instruments TDM Excel add-in was installed. Furthermore, Rstudio scripts were developed to perform statistical analysis on mass loss data, whereas MATLAB scripts were developed to analyze continuous time and cross-sectional data and create graphs.

vi.   Procedure

1.   Principal Assumptions

(1) The testing materials used, including aluminum, stainless steel (austenitic 304) and polyurethane, were susceptible to thermal expansion and compression. Their thermal expansion coefficients were 24, 17.3 and 57.6 $\mu m \cdot m^{-1} \cdot {}^{\circ}C^{-1}$, respectively (The Engineering Toolbox, n.d.). This intrinsic property affected the interaction between wear particles and test plates as the hardness of both may vary as a response to temperature fluctuations. In this study, it was assumed that any temperature changes between measurements were negligible and did not affect the mass loss associated with abrasive wear.

(2) Change in humidity affected the lubrication state between test plates and wear particles. An increase in humidity would contaminate lubricant oil with water and alter its properties. It was assumed that the small changes in humidity levels did not have a significant effect on the properties of the lubricant used in the experiments.

(3) Non-linear movement of the wear particles would theoretically lead to different wear profiles. It was assumed that the motion of the wear particle is strictly linear along the wear grooves.

(4) There was no concentric rolling motion of the ball as it moved back and forth across the test plates.

(5) The compositions of the test materials were uniform across all specimens used in the experiments. It was also assumed that the test plates have uniform thickness across their entire surface area.

2. Test Material Preparation

The wear properties of three types of materials, including aluminum, stainless steel, and urethane-lined aluminum, were characterized using the ball-on-plate testing method. Except for urethane-lined aluminum, all test materials were obtained commercially.

a. Preparation of urethane-lined aluminum

Laboratory-scaled, urethane-coated aluminum was commercially unavailable. Therefore, it was prepared in house by casting polyurethane resin (Repro Light fast-cast) over aluminum sheets. Specifically, a 38.1 cm x 8.89 cm x 0.4 cm reusable cast was made using wood and hot glue. The cast was sprayed with silicone lubricant to prevent adhesion of urethane films to the surface and affixed to a sheet of aluminum using C-clamps. Then, under a fume hood, part A and B of a Repro Light fast-cast urethane was mixed at a 1:1 ratio for two minutes, poured into the cast and cured for two hours, after which the cast was removed.

b. Preparation of specimens

To ensure repeatability, test specimens were polished and cleaned before testing to produce consistent surface roughness and be as free as possible from preparation artifacts. Specifically, each specimen was wet sanded at 120, 380, 600, 1000 grit and finished with extra fine 000 grade steel wool. Following polishing, all specimens were cleaned with acetone and methanol and air dried at room temperature. Average arithmetic surface roughness (Ra) was measured

using a portable surface roughness gage (Mahr federal pocket surf iii) before and after sanding. Typical Ra was in the range of 0.10 μm for aluminum, 0.13 μm for stainless steel. No stable reading was available for urethane (Table 1).

Table 1. Arithmetic surface roughness (Ra) readings (n = 3).

Ra (μm)	Aluminum	Stainless Steel	Urethane
Before Sanding	0.31	0.17	NA
After Sanding	0.10	0.13	NA

In order to understand the instability in reading the Ra of urethane, a white light microscope was used to examine its surface at X160 magnification. Compared to microscopic scratches seen on the surface of aluminum and stainless steel, small bubbles were observed on the surface of urethane. The formation of bubbles was likely due to air trapped during the mixing and casting process. It was presumed that their varying diameters resulted in fluctuations in the reading. Due to limited resources and time constraints, the urethane photographed was used as the test specimens. Since multiple test specimens were cut from the same urethane cast, it can be reasonably assumed that all urethane test plates had the same surface roughness and the minor differences had minimum effect on their wear behavior.
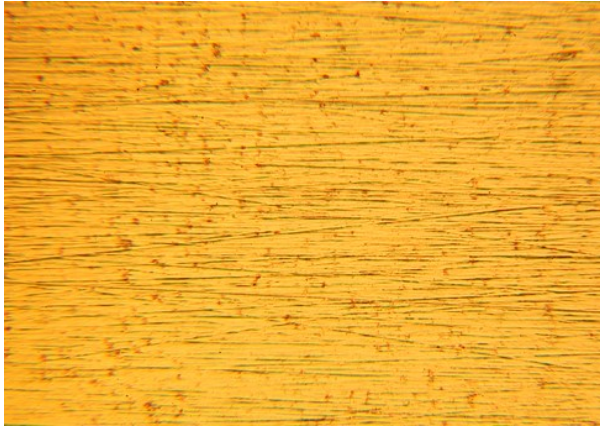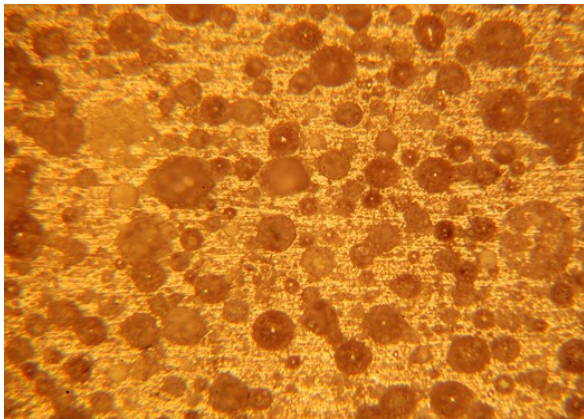
Figure 25. Microscopy images illustrating surface roughness of (a) aluminum, (b) stainless steel and (c) urethane at X160 magnification.

3. Testing Procedure

The following testing procedures were performed:

- Ensure the entire work area was uncluttered and safety shields were erected
- Lift and secure bottom plate with bottom plate holder
- Place acoustic sensor inside acoustic emission housing and apply a thin film of couplant to the sensor surface

- Weigh test specimens with a high precision balance before testing

- Mount test specimens on the t-slotted rails and secure with side clamps. Clean the specimens with isopropanol and allow to dry at room temperature for a minimum of one hour

- If needed, apply silicone or water lubrication (see note below)

- Place a new stainless-steel ball on the ball bearing holder, gently lowed the ball upon the test plate

- Adjust normal force to high, medium or low levels

- Switch on motion drive

- Start LabWindows and AEwin data logging

- Perform wear tests

- Stop data logging

- Switch off motion drive

- Remove test specimens, clean with isopropanol (if lubricant was applied, remove it with degreaser and then clean), air dry for one hour and then measure the mass.

Figure 26. Demonstration of a water lubrication setup.

Note: (1) Water lubrication was applied as shown in Figure 26. (2) No lubrication was tested with urethane-lined aluminum. This was because it was difficult to remove lubricant from the

surface of urethane, which would lead to large errors in the determination of mass loss. (3) Each testing condition was repeated three times.

4. Testing Conditions

The following variables were controlled during experiments;

- Temperature: 23.3 °C
- Relative humidity: 42.5%
- Ball diameter: 0.95 cm
- Stroke length: 0.29 m
- VFD motor speed: 6 Hz
- Test duration: 2 min (sliding distance calculated from potentiometer output)
- Material type: aluminum, stainless steel or urethan-aluminum
- Normal force: high (19.6 N), medium (14.7 N) or low (9.8 N)
- Lubrication: water bath, heavy duty silicone lubricant or no lubricant

Using the experimental setup described above, the next chapter explains in detail the results obtained, the data analysis and processing techniques applied, and the author's interpretation of the observations and underlying wear mechanisms.

IV. Results and Discussion

Abrasive wear occurs when a hard surface slides across a softer surface; in this case, wear is defined as a damage to a solid surface that generally involves progressive loss of material and is due to relative motion between that surface and a contacting substance (Affatato & Brando, 2013). When the contact is between a hard particle and a flat surface, the wear mechanism can be classified as: 1. two-body abrasion, where the particle rubs against a single surface; 2. three-body abrasion, where the particle is trapped between two sliding surfaces; and 3. erosion, where the hard particles are projected against the surface by a stream of fluid. The abrasive wear rate is directly proportional to the distance covered by the hard particle and inversely proportional to the hardness of the material subjected to wear (Affonso, 2006).

Abrasive wear in slurry pipeline is a major industrial problem. Furthering understanding of the effects of all system variables on the abrasive wear rate is essential in order to undertake the appropriate steps in the design of pipeline system and the choice of materials to reduce/control wear. Wear caused by abrasive slurry particles depends on their size, shape, hardness, impact energy they exert on the pipe wall, sliding velocity, etc. In this study, a ball-on-plate machine was developed to simulate and study the two-body abrasive wear in slurry pipelines. The research aimed to characterize the abrasive wear properties of aluminum, stainless steel and polyurethane using mass loss, friction force and acoustic emission. In addition to material type, the effects of applied load, sliding velocity and lubrication conditions were also investigated. All other operating variables, such test duration, temperature, and particle size, were maintained at the same values.

As previously discussed in the chapter on experimental methods, LabWindows was used to acquire ball displacement data from the potentiometer, normal strain data from the normal force load cell, and shear strain data from the friction force load cell at 2 kHz. Mistras AEwin was used to acquire acoustic emission signals at 10 MHz. Both Matlab and RStudio were used for calculating average velocity, total sliding distance, normal force and friction force and for generating plots.

i. Characterization of Wear by Mass Loss

Three types of materials, aluminum, stainless steel and polyurethane, were tested respectively. Since the stainless-steel ball had a hardness greater than that of aluminum and polyurethane, the ball material was more wear resistant than the test material (Table 2). It was presumed that measurable wear only occurred on test materials. Additionally, a new ball was placed on the apparatus at the beginning of each experiment to ensure the ball tip was not worn and, thus, ensure consistency and repeatability in test conditions. Three samples (13.97 cm x 43.18 cm x 0.16 mm for aluminum and polyurethane-lined aluminum flat specimens, 13.97 cm x 43.18 cm x 1.52 mm for stainless steel flat specimens) were tested for each material type. Each weight was measured three times and the difference between the average before and after masses was used to determine mass loss. Furthermore, mass loss was converted to volume loss using the following equation:

$$V = \frac{m}{\rho} \qquad (37)$$

where

V = volume (mm^3)

m = mass (g)

ρ = density (g/mm^3)

Table 2. Test material properties.

Material Type	Hardness	Young's Modulus (GPa)	Density (g/mm³)
Aluminum	107 (Vickers Hardness)	68.9	0.00272
304 Stainless steel	129 (Vickers Hardness)	193-200	0.00785
Polyurethane	68 (Shore D)	2.41 (Freeman Manufacturing)	0.00088

1. Unlubricated Condition

Three levels of normal load: high (19.6 N), medium (14.7 N) and low (9.8 N) were applied. As shown in Figure 27 below, under unlubricated condition, increased load resulted in larger volume loss and greater wear across all materials. Volume loss rate was highest for aluminum, lower for polyurethane and lowest for stainless steel. In other words, without lubrication and within the range of load applied, stainless steel proved to be the most resistant to abrasive wear, followed by polyurethane and then aluminum.

Based on the basic characteristics of sliding wear (also known as abrasive wear) of rough metal surfaces, Archard devised a mathematical model that correlated normal load and material hardness to the wear rate, defined as the amount of material removed per unit sliding distance. Archard's equation provided a mean to calculate the wear coefficient k of the material under test:

$$k = \frac{VH}{WL} \tag{38}$$

where
V = volume loss (mm^3)
H = material hardness (N/mm^2 or MPa)
L = total sliding distance (m)
W = normal load (N)

The concept of a wear coefficient can be used to compare the wearing properties of different material. However, since it is determined empirically by a standard test, it can be expected that the values will vary based on the test conditions even for the same material. Regardless, Archard's equation confirmed that the volume of the removed debris due to sliding wear is proportional to normal load and inversely proportional to harness of materials. Between the two types of metals tested in this study, the experimental observations were consistent with the

theory. As indicated in Figure 27, the volume loss of both Al and SS increased with increasing normal load and Al showed more significant volume loss than SS due to its reduced hardness. Thus, it can be concluded that the utilization of harder materials for building oil pipelines will reduce wear. In addition, abrasive wear rate has been correlated to particle hardness. The higher the ratio between the particle and the surface hardness, the higher the wear rate, which also explained why there was less wear for a steel-steel contact than a steel-aluminum or steel-polyurethane contact.

When Al was coated with a protective polyurethane film, wear rate decreased (Figure 27), attributable to the high elastic deformability or Young's modulus of elastomers (Ashrafizadeh, McDonald, & Mertiny, 2017). The data also showed that SS had higher abrasion resistance than polyurethane; however, in slurry hydrotransportation practice, high performance polyurethane is a popular choice of interior pipe lining. This choice is made because polyurethane does not suffer from corrosion in contact with oxygenated water as steel may do; and polyurethane is in many cases less expensive. Field data suggested that polyurethane-coated pipes last over five times longer than uncoated steel (Magerstädt, 2013). As well, compared to other types of common interior coating such as HDPE (high density polyethylene), polyurethane has higher abrasion resistance due to its viscoelasticity (Ashrafizadeh, McDonald, & Mertiny, 2017).

In summary, under unlubricated conditions, the ranking of abrasion wear resistance from high to low was stainless steel, polyurethane-coated aluminum, and aluminum.
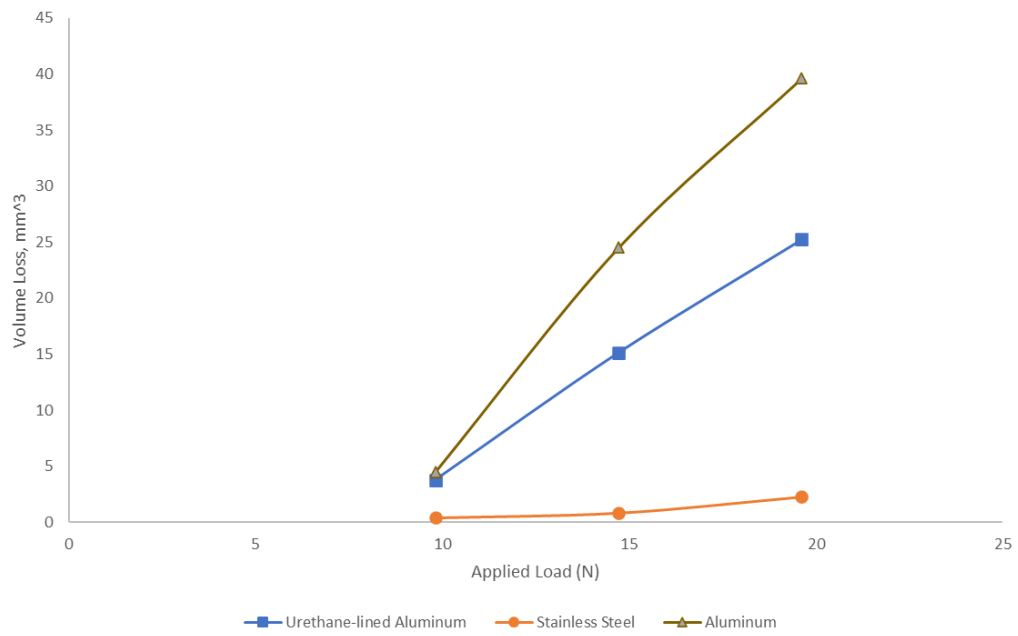
Figure 27. Volume loss – normal load correlation with no lubrication.

2. Lubricated Condition

The test specimens were also tested under lubricated conditions. Once again, each condition was tested on three specimens of the same material type and triplicate measurements of the weight were obtained. Two types of lubricants, water and heavy-duty silicone oil, were used. For water lubrication, a 3D printed container filled with water was placed on top of the flat test specimens, which in effect covered both the surface of the specimens and the stainless-steel ball. For silicone oil lubrication, a thin film of silicone was applied uniform across the contact surfaces between the ball and the test specimens.

With stainless steel, only silicone lubrication was applied. When using water as the lubricant, a 3D printed container was glued to the specimens first and the mass loss was determined based on the before and after masses of the total weight and the specimen and the water container. However, with the 3D part included, the total weight of stainless-steel samples exceeded the maximum capacity of the scale balance. As a result, water lubrication was not examined with stainless steel. With aluminum, both water and silicone oil were tested. For polyurethane-line aluminum, no lubrication was tested because it was difficult to remove the greasy lubricant from the surface of polyurethane, which would lead to large errors in the process of determining mass loss.

Figure 28 and Figure 29 compared volume loss in abrasive wear under unlubricated and lubricated conditions for aluminum and stainless steel, respectively. With aluminum, both oil and water lubrication reduced volume loss at all three load levels, with oil being more effective than water. The reason that lubrication is critical for minimizing friction and wear between moving mechanical components can be explained here by the mechanism of sliding wear, which is the result of the interaction of two mechanisms: 1. plasticity and adhesion and 2. oxidation. The energy dissipated by the friction during the wear process generates heat, even at low speeds. Since oxygen was present in the ambience of the laboratory, the temperature increase would have resulted in fast oxidation of the exposed metal. The oxide layer can have effects on wear rate (Affonso, 2006). However, for simplicity, the accelerated oxidation was assumed to have

minimal effects on wear behavior in the testing conducted in this study. In terms of plasticity and adhesion, the sliding of a metal ball across a metal surface generally results in plastic deformation, followed by adhesion and metal removal. With lubrication, ideally the contacting/sliding surfaces would become completely separated and thus, prevent abrasion. However, even when complete separation is not possible, especially when the contact load is high, lubrication can reduce wear by making adhesion more difficult and subsequently reducing mass loss (Stachowiak, Wear - Materials, Mechanisms and Practice, 2005).

On the other hand, with stainless steel, the effect of lubrication was surprising, as with the presence of a film of silicone lubricant, volume loss increased for medium (50%) and high load (18.7%). A few possibilities can be used to explain the observation: first, as demonstrated previously, there was significantly less volume loss associated with stainless steel compared to aluminum and polyurethane. The scale used to weigh the test specimens had a resolution of 0.01 g and calibrated to a tolerance of ±0.02g, close to the mass loss range for stainless steel. Small mass loss combined with insensitive measurement device consequentially entailed low accuracy in mass loss determination. Second, even though the test specimens were cleaned with isopropanol and air dried before weighing, possible complications may arise from entrapped debris and thermal expansion may occur due to frictional heating. Third, when the particle size was bigger than the lubricant film thickness, lubrication increased wear (Affonso, 2006). It is possible that, as friction between the particle and the surface was reduced, lateral movement and eventually mass loss become easier.
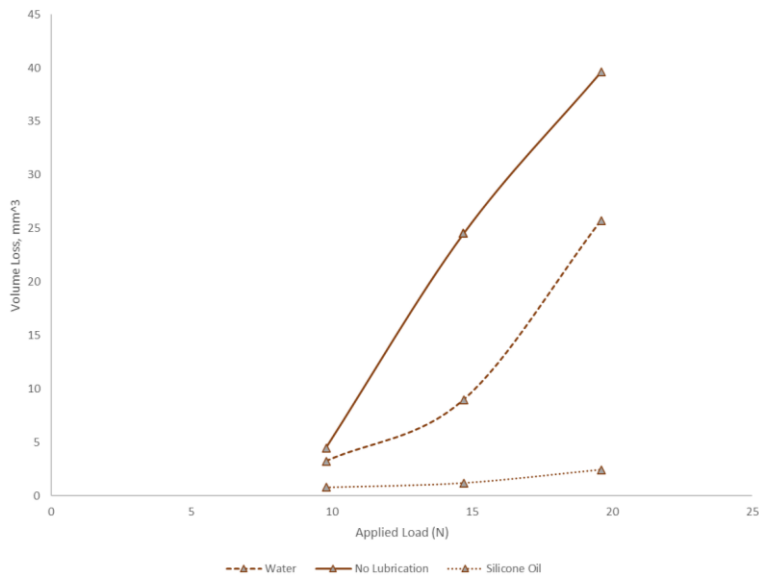
Figure 28. Comparison of volume loss under unlubricated and unlubricated conditions for aluminum.
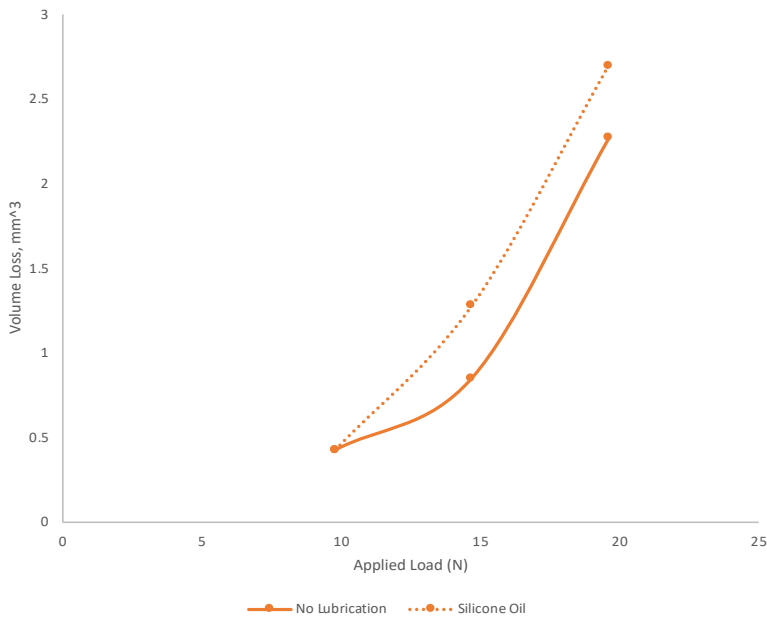

Figure 29. Comparison of volume loss under unlubricated and unlubricated conditions for stainless steel.

ii. Characterization of Wear by Coefficient of Kinetic Friction Force

The coefficient of kinetic friction is defined as the ratio of kinetic friction force to the normal force, or

$$\mu_k = F/P \qquad\qquad (39)$$

where

μ_k = kinetic friction coefficient

F = nominal, measured friction force during sliding, N

P = applied load (normal force), N

As indicated by the equation above, the normal load influences the value of friction coefficient. Apart from the normal load, existing studies have shown that surface conditions (surface roughness, mechanical properties and lubrication) and operating conditions (sliding velocity) can also affect friction coefficient (Menezes, Kishore, & Kailas, 2009). It should be noted that, as G. Salomon once pointed out, coefficient of friction is not a material property, but instead a convenience describing a friction system. In other words, it is a constant for a given pair of sliding materials and is dependent on the operating conditions, such as temperature, humidity, normal pressure and sliding velocity (Bhushan, 1996).

Table 3. Average sliding velocity v (m/s) and coefficient of kinetic friction μ_k for aluminum (AL), stainless steel (SS) and polyurethane (PU)

Material	Dry				Oil				Water			
	High		Low		High		Low		High		Low	
	v	μ_k	v	μ_k	v	μ_k	v	μ_k	v	μ_k	v	μ_k
AL	0.351	4.884	0.418	12.485	0.405	5.972	0.418	15.701	0.357	4.389	0.411	10.311
SS	0.379	5.184	0.419	10.002	0.369	8.811	0.418	16.085	NA	NA	NA	NA
PU	0.406	4.491	0.418	16.662	NA	NA	NA	NA	NA	NA	NA	NA

Note: High and low refers to high (19.6 N) and low (9.8 N) normal load.

Table 3 above summarizes coefficient of kinetic friction measured in the tests conducted in this study. Under low load (9.8 N), the sliding velocity for all materials and all lubrication conditions (dry, water and silicone oil) was approximately 0.418 m/s. At this load level, surface roughness (dependent on material type and lubrication) appeared to have no effect on the sliding velocity. In contrast, when the load was increased to 19.6 N, the sliding speed universally decreased, ranging from 2.9 % for dry polyurethane and 3.0% for oil-lubricated aluminum to 16% for dry aluminum.

Furthermore, regardless of material type and lubrication conditions, it can be seen that, in the range of normal load applied, higher load was associated with smaller coefficient of kinetic friction for the same materials. Other studies have reported similar observations (Chowdhury, Khalil, Nuruzzaman, & Rahaman, 2011). It was hypothesized that the hardness of a material that was severely deformed under a heavy load may be two or three times higher than it was before sliding began (Blau, 1996) and increased material hardness resulted in decrease in the coefficient of kinetic friction (Mikhin & Lyapin, 1972).

For aluminum under high load, μ_k was 4.884 without lubrication, which increased to 5.972 using silicone oil as the lubricant and decreased to 4.389 using water as the lubricant. For

Material	Dry				Oil				Water			
	High		Low		High		Low		High		Low	
	v	μ_k	v	μ_k	v	μ_k	v	μ_k	v	μ_k	v	μ_k
AL	0.351	4.884	0.418	12.485	0.405	5.972	0.418	15.701	0.357	4.389	0.411	10.311
SS	0.379	5.184	0.419	10.002	0.369	8.811	0.418	16.085	NA	NA	NA	NA
PU	0.406	4.491	0.418	16.662	NA	NA	NA	NA	NA	NA	NA	NA

aluminum under lower load, the trend remained the same, where $\mu_{k, oil} > \mu_{k, dry} > \mu_{k, water}$. For stainless steel under either load level, μ_k also increased when oil was used to lubricate the test plates.

To understand the above observations, it is important to discuss the different lubrication regimes determined by the relationship between mean lubricant film thickness and root-mean-square

(rms) roughness of the two contact surfaces. This relationship is defined by a parameter known as the lambda ratio, λ, defined as

$$\lambda = \frac{h}{\sqrt{R_{q_1}^2 + R_{q_2}^2}} \tag{40}$$

where h is lubricant film thickness and $R_{q_1}^2, R_{q_2}^2$ are the rms roughness values of the two contact surfaces. The lubricant film thickness was reported to be proportional to sliding velocity, lubricant viscosity and inversely proportional to the applied load (Menezes, Kishore, & Kailas, 2009). When $\lambda > 3$, the lubrication regime is full-film lubrication, in which surfaces are well separated by the lubricant. When $3 > \lambda > 1$, the lubrication regime is mixed lubrication and when $\lambda < 1$, dry lubrication occurs.

Under different lubrication regimes, the connection between μ_k and operating conditions can be predicted by the classic "Stribeck" curve, as shown below. In this study, it is known that at 25 °C, the viscosity of silicone oil and water is 10 cSt and 0.894 cSt, respectively. The average (n =3) arithmetic surface roughness (R_a) of aluminum and stainless steel was measured to be 0.10 μm and 0.13 μm, respectively. However, information on lubricant film thickness was not available. As a result, the lubrication regime the tests were conducted in cannot be determined from the Stribeck curve. Additionally, there were not sufficient data to develop a model to predict the correlation between coefficient of kinetic friction and experimental conditions.
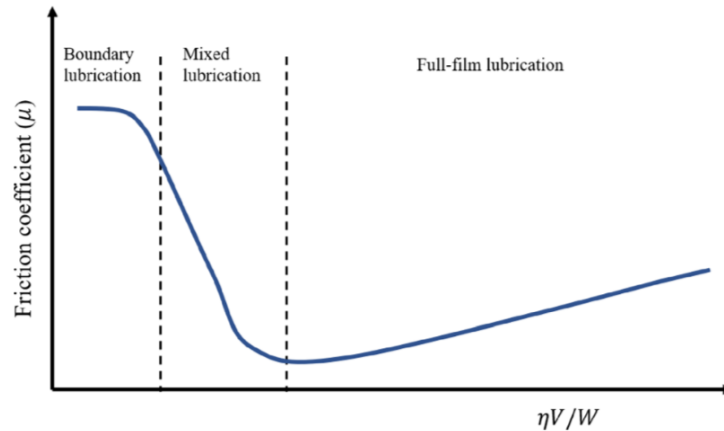
Figure 30. Stribeck curve showing correlation between friction coefficient μ and $\eta V/W$. η denotes viscosity; V denotes sliding velocity; and W denotes normal load (Feng, Borghesani, Smith, Randall, & Peng, 2020).

iii.   Characterization of Abrasive Wear by Acoustic Emission

Acoustic emission is a phenomenon of rapid release of transient elastic waves generated by the dynamic localized rearrangement of the internal structure of a material (Standard Terminology for Nondestructive Examinations, 1990). Abrasion is a source of AE signals. More specifically, abrasion results in material deformation, material removal which generates heat, audible noise and acoustic emission. The AE technique is a sensitive and nondestructive structural health monitoring technique. Normally, AE elastic waves are sampled through a data acquisition system with piezoelectric sensors and amplifiers, transferred into electrical waveforms and analyzed using digital signal processing methods (Feng, Borghesani, Smith, Randall, & Peng, 2020). In this study, two types of acoustic emission data were acquired, including high frequency (10 MHz) burst data files at 1-s intervals and low frequency (50 Hz) continuous data of 120 s for each test.

Since the 1980s, many researchers have considered using AE generated by interacting surfaces to monitor friction and wear of mechanical components in sliding contact. For example, Matsuoka (Matsuoka, Forrest, & Tse, 1993) established a correlation between the AE rms voltage and the square root of the material removal power for a test used to monitor wear of

magnetic recording head materials. Wear removal power was calculated as the product of Archard's wear coefficient, normal load and sliding velocity. The correlation can be expressed as

$$V_{rms} = \alpha(kNv)^{1/2} + \beta \tag{41}$$

where

V_{rms} = AE rms voltage (V)

k = coefficient of wear

N = normal load (N)

v = sliding velocity (m/s)

α, β = constants, determined empirically

Other experimental and theoretical AE models (Feng, Borghesani, Smith, Randall, & Peng, 2020) also demonstrated the dependency of AE on surface conditions (surface roughness and lubrication) and operating conditions (normal load and relative velocity). However, such correlations are application and case specific and, thus, cannot be directly applied to the ball-on-plate abrasion testing apparatus developed in this study to establish the relationship between wear rate and AE. The results acquired using the abrasion testing apparatus developed in this study are discussed in the next section.

1. Analysis of Continuous AE Data at 50 Hz

The acoustic emission data acquired at 50Hz for aluminum, stainless steel, and polyurethane were analyzed below.

a. AE Noise

Noise data was acquired by running the abrasion apparatus for 12 seconds with the loading system suspended so that the stainless steel ball was not in contact with the test plate. As can

be seen in Figure 31, the ambient noise levels were low compared to when the ball was sliding across the test plate and its impact on the AE signal acquisition can be ignored.
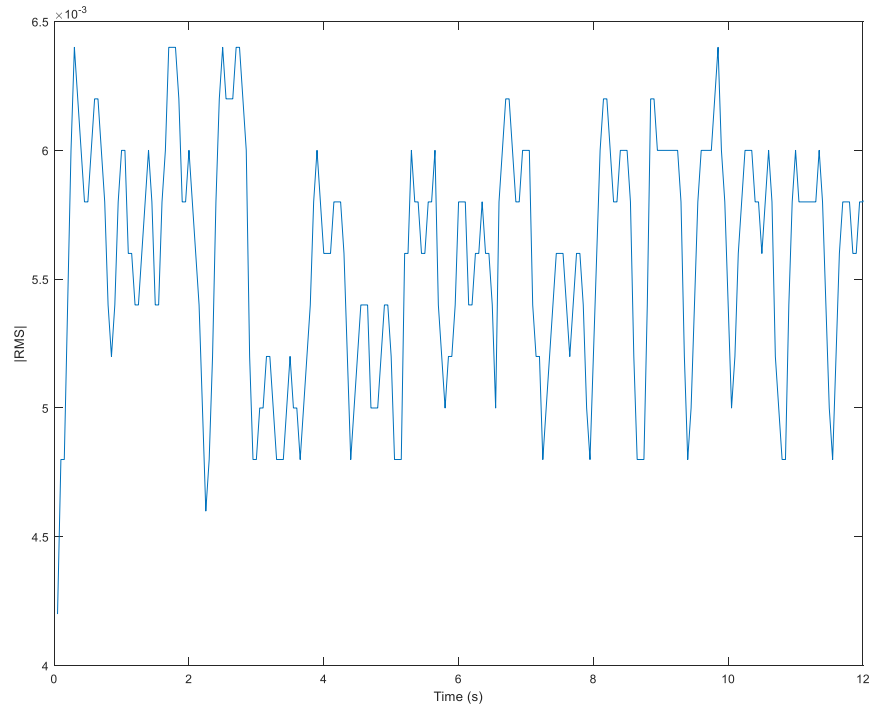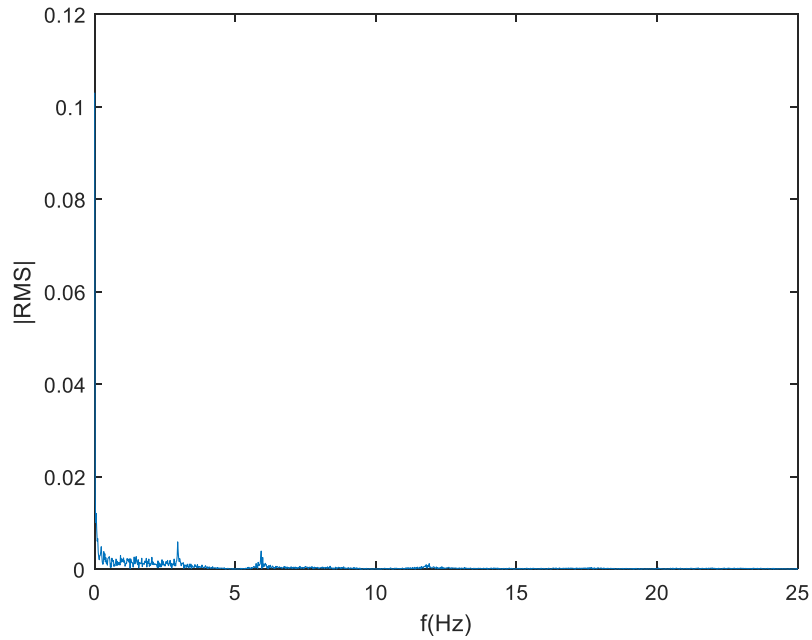
Figure 31. Acoustic emission root-mean-square (RMS) of noise (a) over time (b) frequency response.
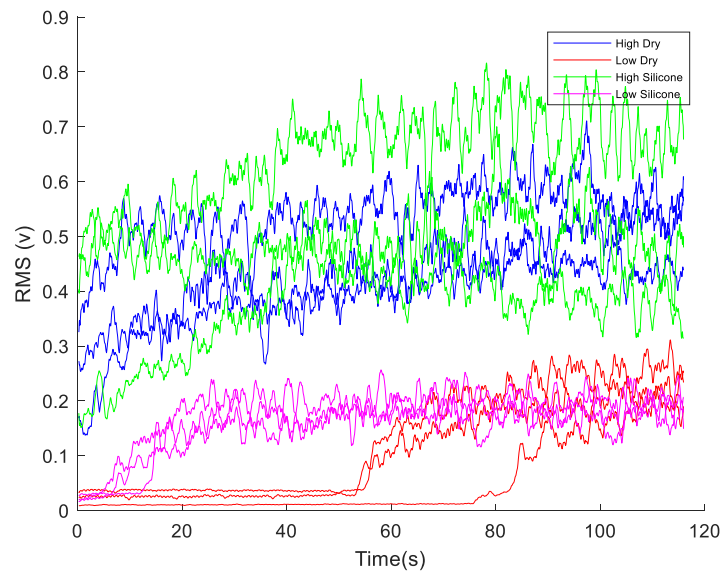
b. AE RMS signals
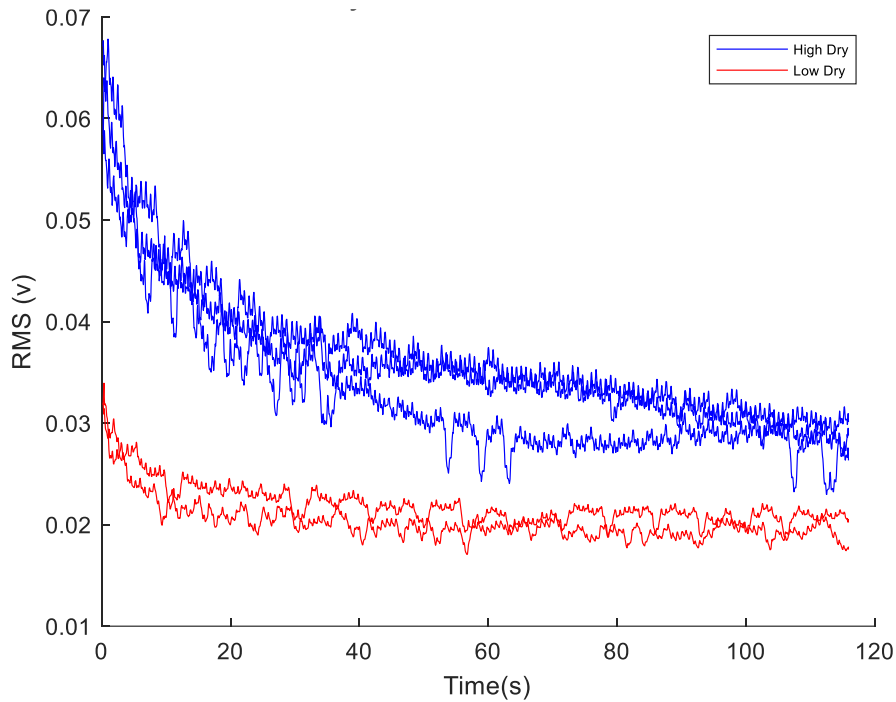
The RMS data set was processed at 50Hz below.

(a)
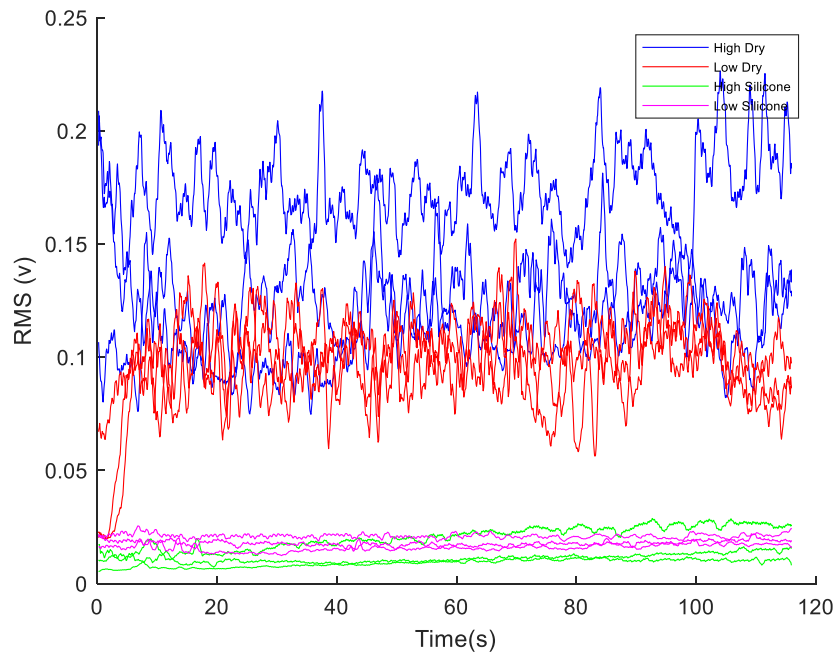
(b)
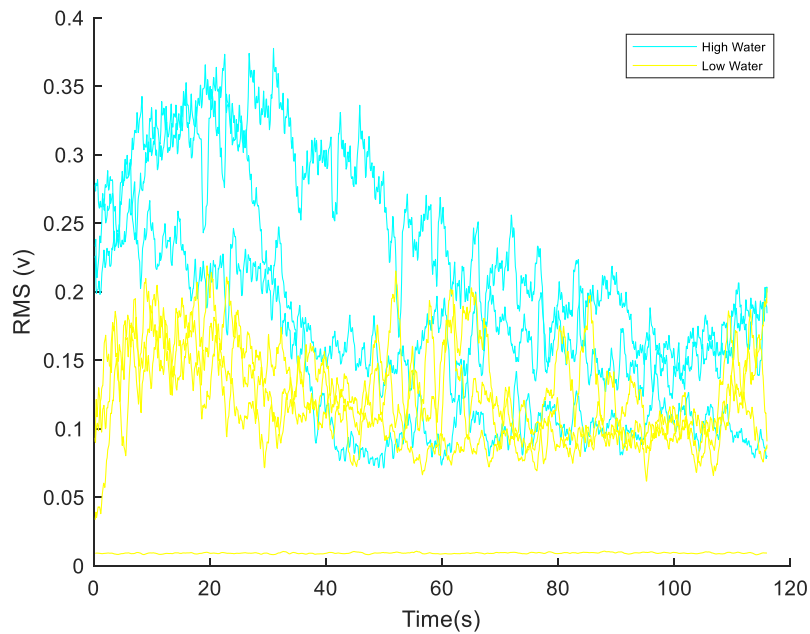
Figure 32. Acoustic emission root-mean-square (RMS) trend over time under various normal load and lubrication conditions for aluminum flat specimens. (a) dry and silicone lubrication; (b) water lubrication.

Figure 32 showed the change in AE RMS voltage over the test duration of 120 seconds for aluminum. Triplicate runs under each set of load and lubrication conditions were represented by three curves of the same color. It was observed that AE RMS voltage correlated with surface and operating conditions. The normal load was 19.6 N for high load and 9.8 N for low load. Silicone oil and water were used as lubricants in different trials.

For aluminum flat specimens under dry conditions (red and blue curves), RMS displayed a regular fluctuation of approximately 0.05 V over time in both high and low load, whereas the average amplitude stayed constant. The repeatability under low load appeared to be superior to that under high load. Overall, increased load resulted in an increase in RMS.

When silicone was used as the lubricant (green and pink curves), the ball-on-plate abrasion testing generated minimal acoustic emission signal, regardless of the load. In contrast, when water was used as the lubricant, the average RMS signals appeared to be higher in the first half than the second half of the testing under high load. Under low load, the average amplitude remained constant but fluctuated at 0.1 V over time. Compared to unlubricated specimens, aluminum immersed in water bath resulted in higher AE RMS. Increased load resulted in an increase in RMS.

Figure 33. Acoustic emission root-mean-square (RMS) trend over time under various normal load and lubrication conditions for stainless steel flat specimens.

Figure 33 showed the change in AE RMS voltage over the test duration of 120 seconds for stainless steel. Triplicate runs were represented by same-color curves. Only silicone was used as lubricant. Different from aluminum, the AE RMS signals generated by stainless steel gradually increased over time. Silicone lubrication appeared to have no AE RMS under either load, as indicted by the similarity between high dry (blue) and high silicone(green) curves, and low dry (red) and low silicone (purple) curves, respectively. Regardless of lubrication condition, RMS increased with load. In other words, normal load had a bigger influence on RMS level than lubrication. For dry, low load condition, the first 50 seconds of the testing generated minimal AE, the potential cause of which was analyzed in the next section.

Figure 34. Acoustic emission root-mean-square (RMS) trend over time under various normal load and lubrication conditions for polyurethane flat specimens.

As mentioned in the experimental section, polyurethane was only tested under unlubricated condition. Figure 34 showed the change in AE RMS voltage over the test duration of 120 seconds for stainless steel. Repeats of the same experimental conditions were graphed as same-color curves. Unlubricated polyurethane displayed an increase in RMS with increased load. Under high load, the signal was highest at the beginning of the testing and gradually decreased to approximately 50% of its amplitude at t = 0 over 40 s. The signal remained unchanged for the rest of the test. Under low load, RMS started slightly higher at 0.03 V, decreased to 0.02 V over 10 s and remained constant for the rest of the test. Overall, the RMS voltage of polyurethane was significantly lower than that of both aluminum and stainless steel. This is likely due to the fact that polyurethane elastomer is a viscoelastic material.

It can be concluded that, with the norm load range tested, higher load resulted in higher AE RMS for all three materials. Additionally, under unlubricated condition, harder materials generated higher RMS signals.

c. Correlation between AE RMS voltage and kinetic friction force

As seen above, in Figure 33, at a load of 9.8 N, unlubricated stainless-steel specimens generated very low RMS signal in the first 50 s of the test duration. The author decided to explore whether there existed a correlation between the kinetic friction force and the delayed onset of acoustic emission signal. Figure 35 confirmed that a positive connection existed. It was observed that AE RMS abruptly increased when the friction forced exceeded 100 N.

Figure 35. Correlation between AE RMS voltage of dry stainless steel and kinetic friction force. (9.8 N normal load).

The correlation between RMS and friction force held true for dry aluminum under low load (9.8 N), where the RMS increased abruptly and significantly when friction force exceeded 100 N, as shown in Figure 36 below.
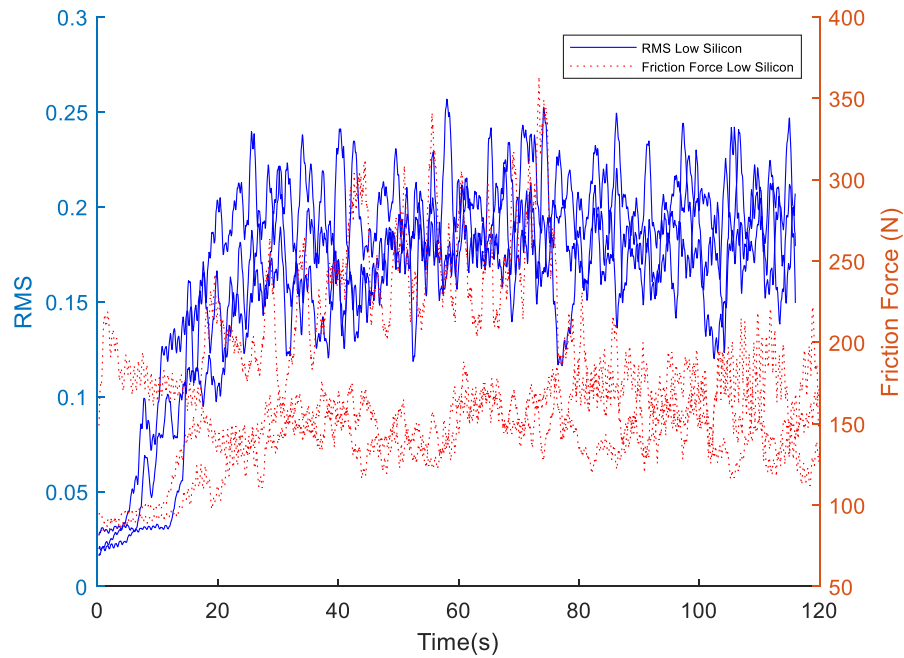
Figure 36. Correlation between AE RMS voltage of dry aluminum and kinetic friction force (9.8 N normal load).

d. Fast Fourier Transformed (FFT) AE RMS signals

The AE signals were analyzed using FFT to examine the frequency distribution of abrasive wear. The Nyquist frequency of 25 Hz was used to analyze the data. Overall, for all three types of materials, high intensity acoustic emission signals were detected below 10 Hz whereas lower intensity peaks were detected at 10 - 25 Hz.

- **Aluminum (Al)**
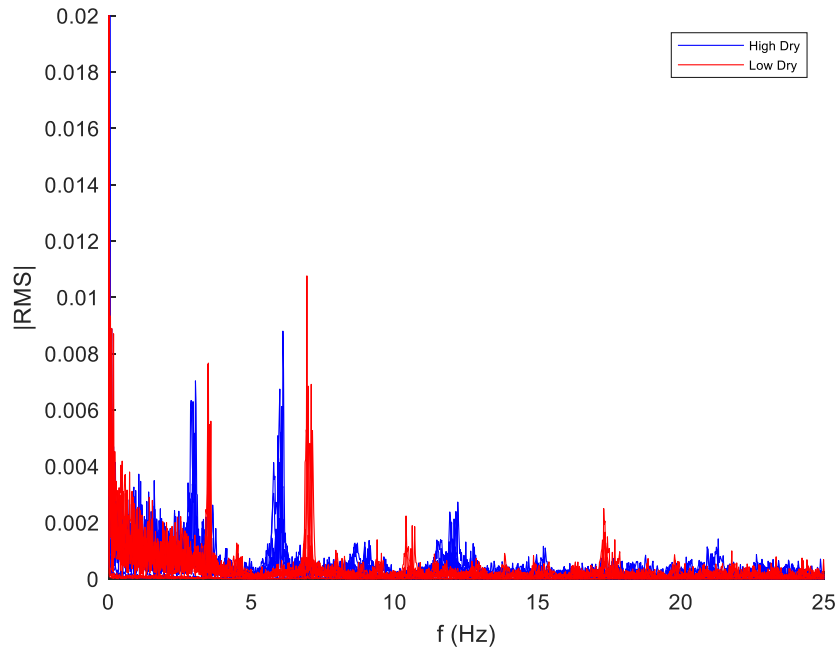
Figure 37. Frequency spectrum of AE signals for unlubricated aluminum (overlaid triplicate runs for each condition).

Figure 37 compares the frequency analysis results for dry aluminum under high and low load. Noise was observed in the infrasonic range. There were three dominant peaks at 1, 4 and 7 Hz, respectively, with the highest peak at 1 Hz with an RMS of 0.02 V for low load (check high load, blue). The peaks at 4 and 7 Hz for low load shifted to lower frequencies at approximately 3 and 6 Hz, respectively but remained of similar amplitude (RMS between 0.007 and 0.011 V) when the load increased.
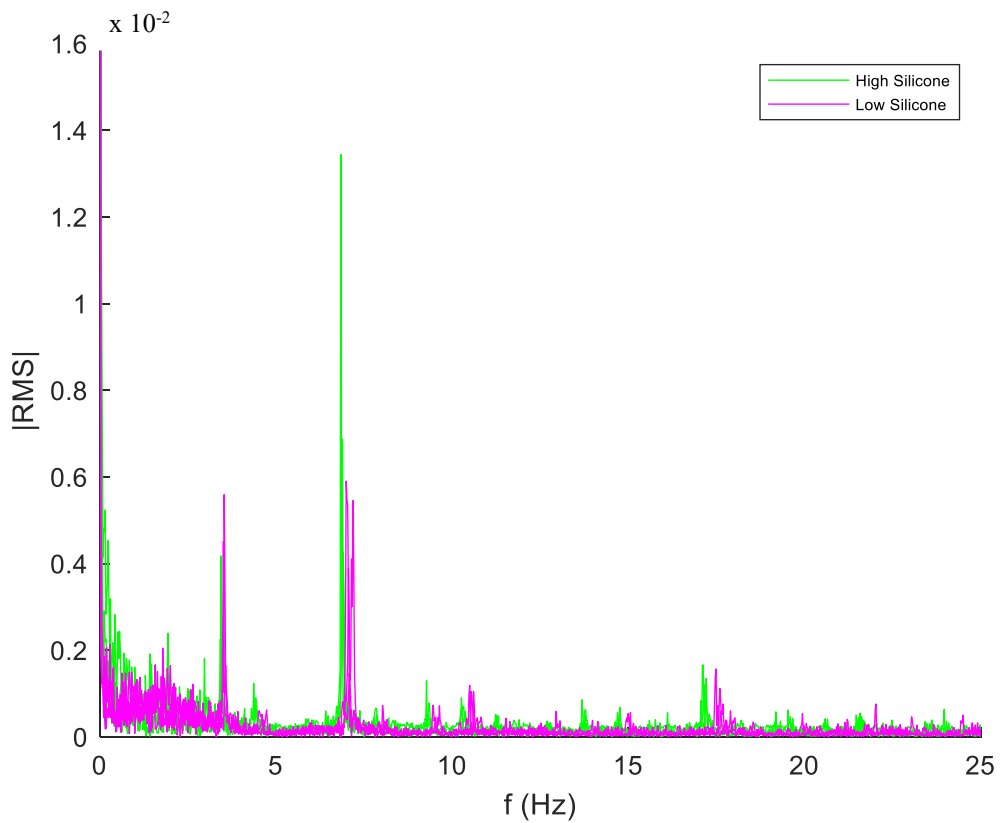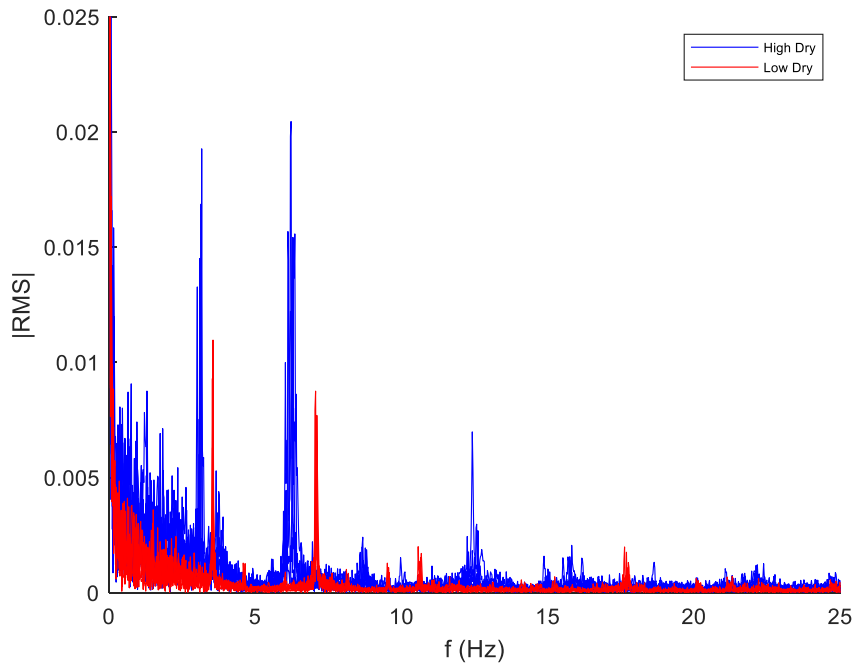
Figure 38. Frequency spectrum of AE signals for silicone-lubricated aluminum (overlaid triplicate runs for each condition).

Figure 38 compares the frequency analysis results for silicone-lubricated aluminum under high and low load. There were three dominant peaks at 1, 4 and 7 Hz, respectively, with the highest peak at 7 Hz. Unlike unlubricated condition, there was no discernable shift in the frequencies of the dominant peaks when the load changed. The peak amplitude was 0.2E-3 for low load and 0.5E-3 V high load. The peak amplitude at 4 Hz was 0.6E-3 for low load and 0.4E-3 V for high load. The peak amplitude at 7 Hz was 0.6E-3 V for low load and 1.35E-3 V for high load.
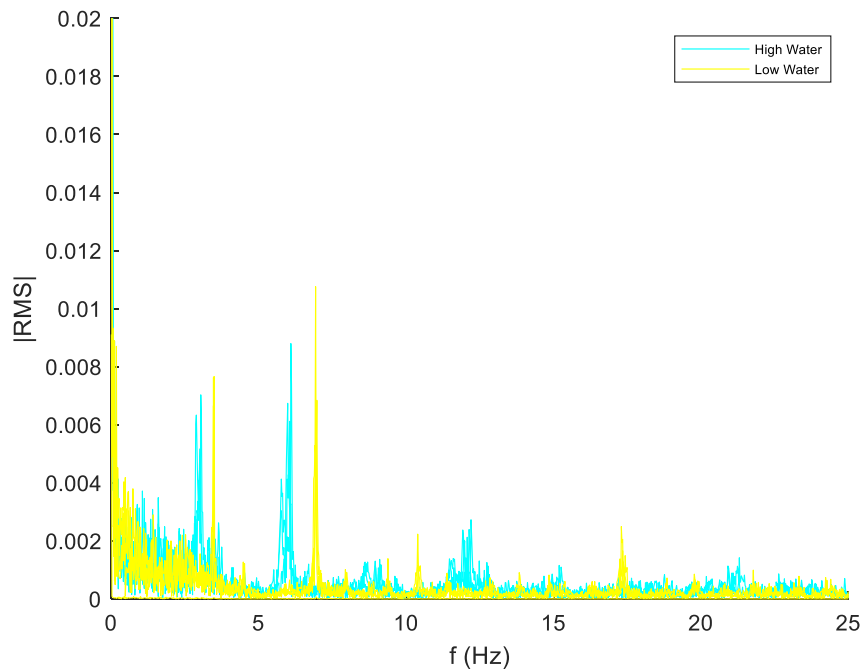
Figure 39. Frequency spectrum of AE signals for water-lubricated aluminum (overlaid triplicate runs for each condition).

The frequency analysis for AE signals acquired from water-lubricated aluminum was very similar to that for unlubricated aluminum. Figure 39 compares the frequency analysis results for water-lubricated aluminum under high and low load. Same as with dry aluminum, the peaks at approximately 4 and 7 Hz for low load shifted to lower frequencies at approximately 3 and 6 Hz, respectively but remained of similar amplitude (RMS between 0.007 and 0.011 V) when the load increased.

In summary, with increased load, AE signals increased for silicone-lubricated aluminum and decreased slightly for dry and water-lubricated aluminum. With dry and water-lubricated aluminum, the frequency analysis results were very similar (RMS between 0.007 and 0.011 V). With silicone-lubricated aluminum, the AE signal intensities for the two dominant peaks in the frequency region below 10 Hz were approximately 10 times lower for those corresponding to dry and water lubricated conditions. The author hypothesizes that the decrease in wear due to

86

lubrication resulted in increased particle movement, thereby causing the increase in acoustic emission.

- **Stainless steel (SS)**

Figure 40. Frequency spectrum of AE signals for unlubricated stainless steel (overlaid triplicate runs for each condition).

Figure 40 compares the frequency analysis results for dry stainless steel under high and low load. Same as with aluminum, two dominant peaks showed at 4 and 7 Hz under low load, which shifted to 3 and 6 Hz, respectively when the load increased. Their peak heights displayed a corresponding two-fold change from 0.01 to 0.02 V as the load increased from 9.8 to 19.6 N. An additional peak at 12.5 Hz was observed with an amplitude of 0.0075 V for high load.
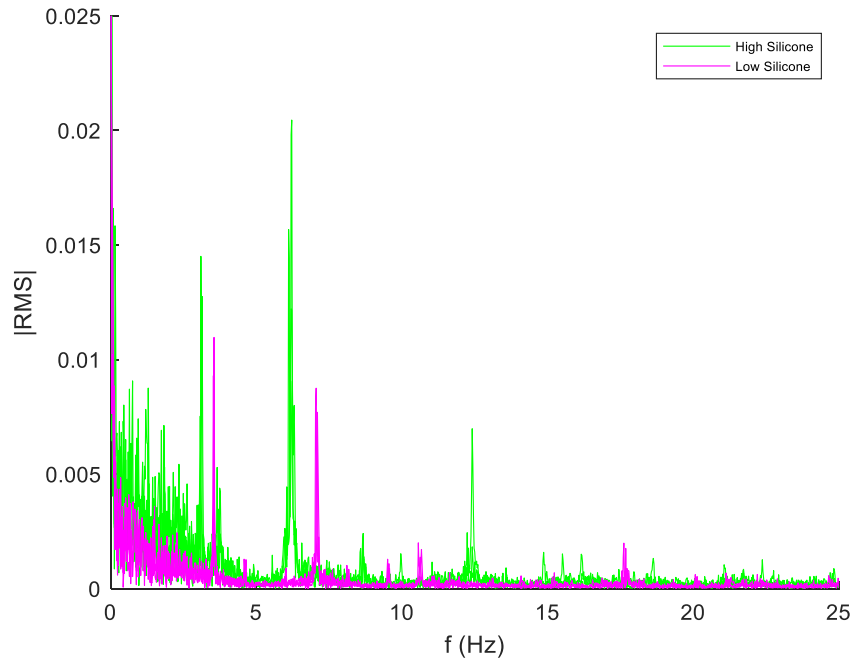
Figure 41. Frequency spectrum of AE signals for silicone-lubricated stainless steel (overlaid triplicate runs for each condition).

No apparent difference in the frequency analysis of the AE signals acquired from dry and silicone-lubricated stainless steel was observed (Figure 41). Similarly, two dominant peaks showed at 4 and 7 Hz under low load, which shifted to 3 and 6 Hz, respectively when the load increased. Their peak intensities doubled as the normal load increased by two folds. An additional peak at 12.5 Hz was observed with an amplitude of 0.0075 V for high load.

In summary, with an increased load, AE signals in the low frequency range (< 10 Hz) increased for stainless steel by approximately 30 -125%. Dry and silicone-lubricated conditions resulted in similar frequency analysis results. The amplitude of the peaks in under 10 Hz region were similar to dry and water-lubricated aluminum.

- **Polyurethane (PU)**
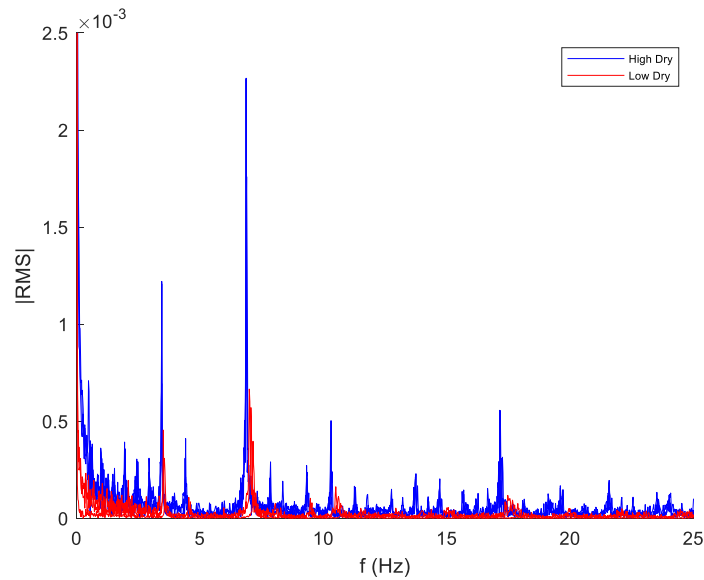
Figure 42. Frequency spectrum of AE signals for dry polyurethane (overlaid triplicate runs for each condition).

Dry polyurethane showed very low AE signals, similar in both peak distribution and intensity to silicone-lubricated aluminum. The characteristic peaks were at 4, 7, 11 and 17.5 Hz.

2. Analysis of 10 MHz AE Burst Data
a. Frequency analysis

Each burst data file was acquired for 0.7168 ms every second at a frequency of 10 MHz during the 120 s run time. In effect, each file consisted of 7168 data points. To extract the frequency components of the AE data, the burst files at 20 s intervals (20, 40, 60, 80 and 100 s) were Fourier transformed and their power spectrum was plotted against frequency. The results for each material were discussed separately. Below, amplitude was either expressed in volts or in decibels, which are related by the following equation:

$$dB = 20 \cdot log_{10}\left(\frac{V}{0.01}\right) + Gain \tag{42}$$

where gain is a linear boost in signal applied by the preamplifier during waveform acquisition.
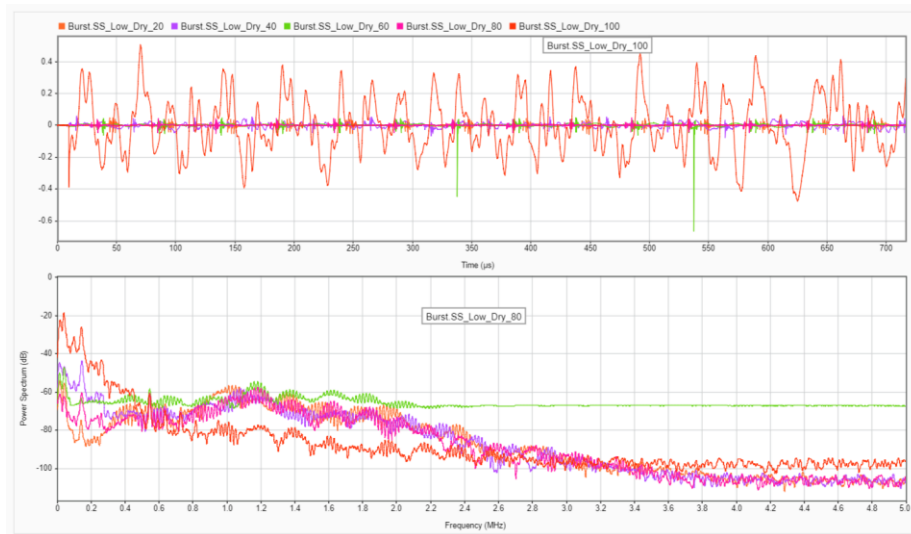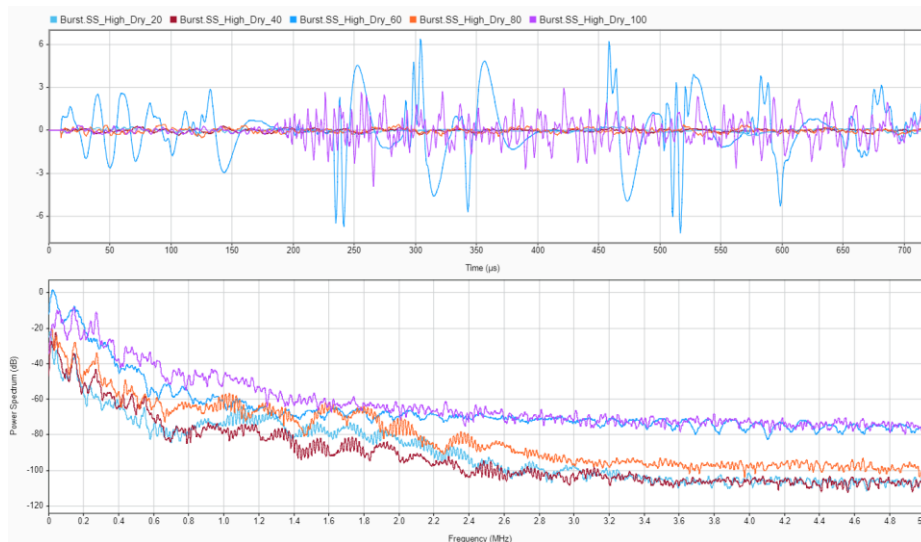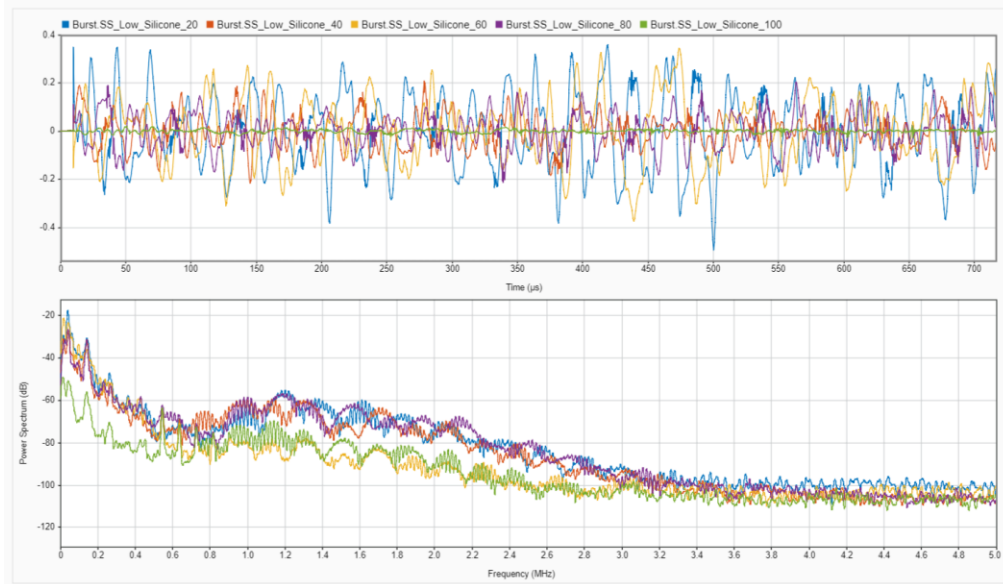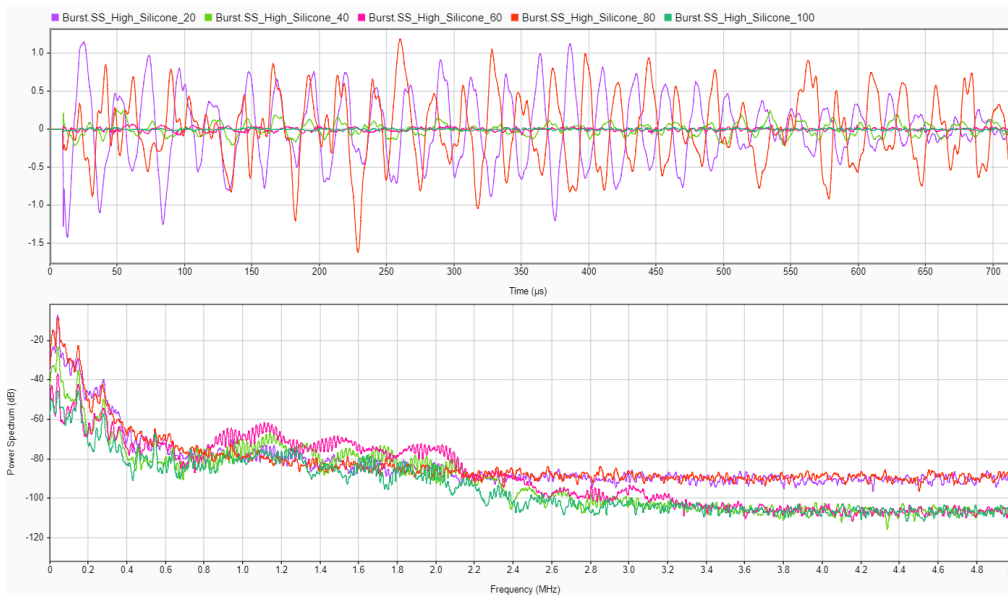
- **Aluminum**

(a)
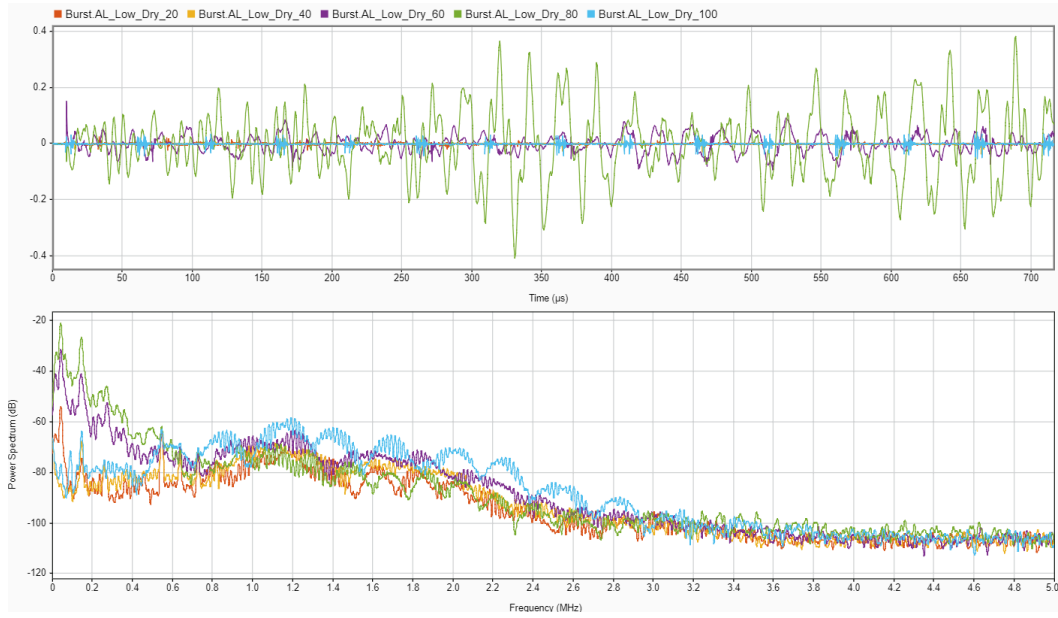
(b)
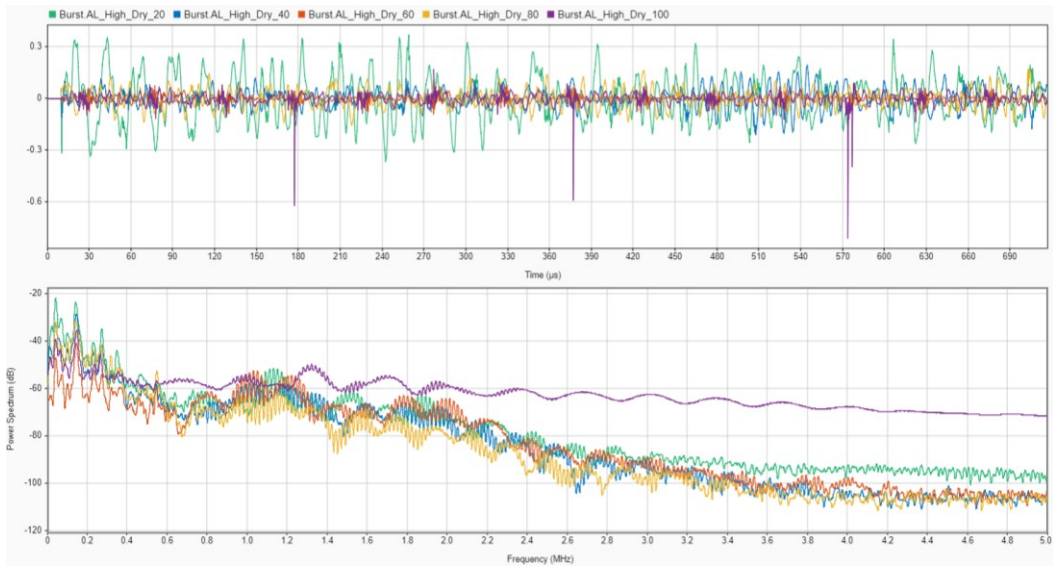
Figure 43. AE sensor output voltage (mV) vs. time (s) plot and FFT spectrum in dB scale for unlubricated aluminum in (a) low load and (b) high load.

Previously, in the discussion of mass loss section, it was demonstrated that the volume loss due to abrasion increased with normal load. The burst data showed that (Figure 43), under low load, AE signals remained unchanged over time. Under high load, AE signals in the higher frequency range (1-5 MHz) increased in power (dB) starting at 100 s.

(a)
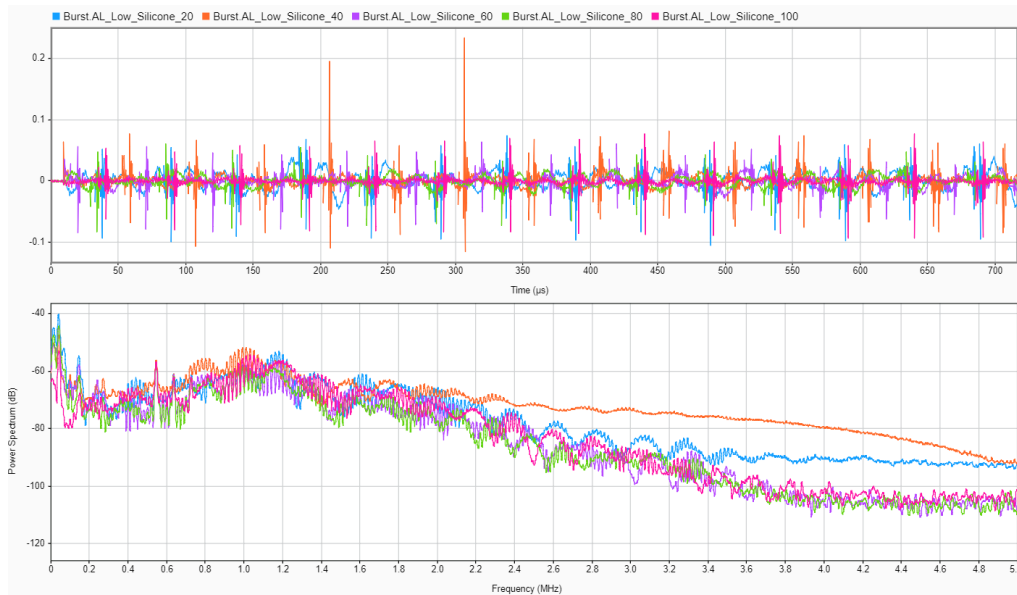
(b)
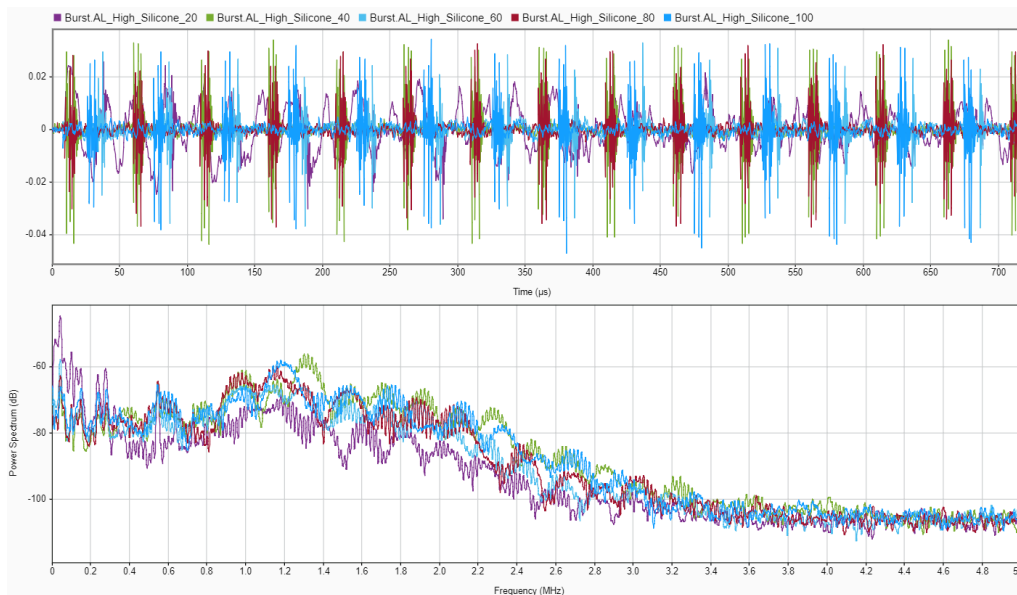
Figure 44. AE sensor output voltage (mV) vs. time (s) plot and FFT spectrum in dB scale for silicone-coated aluminum in (a) low load and (b) high load.

When silicone oil was employed as lubrication (Figure 44), under low load, 20 and 40 s AE signals were more intense that those at later times. In another word, with lubrication, AE decreased over time under a load of 10 N. Under high load, the AE signals appeared to be unchanged over time.

- **Stainless steel**

(a)

(b)

Figure 45.AE sensor output voltage (mV) vs. time (s) plot and FFT spectrum in dB scale for unlubricated stainless steel in (a) low load and (b) high load.

Similar to aluminum, the burst data of stainless steel (Figure 45) showed that, under low load, AE signals remained unchanged over time (the 60 s trace was believed to be an abnormal outlier). Under high load, AE signals in the 1-5 MHz range increased in power (dB) starting at 100 s.

(a)

(b)

Figure 46. AE sensor output voltage (mV) vs. time (s) plot and FFT spectrum in dB scale for silicone-coated stainless steel in (a) low load and (b) high load.

Under lubricated condition (Figure 46), the AE signals of SS remained constant under low load. Under high load, it appeared the AE signals in the 2-5 MHz ranged increased at 20 s and 80 s to the same level.

b. Hilbert-Huang Transform

The AE signals collected during wear processes are often mixed with a variety of interferential signals with different amplitude and frequency values, making them non-stationary and non-linear in nature (Nie, Dong, Chen, Li, & Gao, 2012). The Hilbert-Huang transform (HHT) (Huang Norden E., 1998) is a good approximation to the ringing of an underdamped mechanical system, and so it is reasonable to use it to detect propagation of stress waves released during an impact or a damage event. The analysis comprises of two steps: (1) empirical mode decomposition (EMD) and (2) Hilbert transformation (MathWorks, Inc., 2021). The objective of EMD is to break down the original signals $x(t)$ into a series of intrinsic mode functions (IMFs) $imf_i(t)$ and a residual $r_N(t)$ in an iterative process, expressed by

$$x(t) = \sum_{i=1}^{N} imf_i(t) + r_N(t) \tag{43}$$

To create a Hilbert spectrum using the IMF components obtained using EMD, a plot of frequency vs. time is created, containing information on energy.

Using MATLAB, the IMFs plots, Hilbert spectra in mesh plot format were obtained for the burst datasets (0.718 ms) acquired at 40 s for Al, SS and PU lined Al under various combinations of load and lubrication conditions. Distinguishing AE features were observed for different materials under different conditions. It is foreseen that with more extensive experimentation, AE data can be used to differentiate and characterize wear events. Specifically, it appeared that for Al without lubricant (Figure 47), Al lubricated with water (Figure 49) and SS without lubricant (Figure 50), low load condition resulted in one more IMF components than high load, suggesting the signal under low load had higher non-linear behavior. For all other conditions, the number of IMFs was the same between low load and high load.

Furthermore, the Hilbert spectra revealed that higher load/higher volume loss was mostly composed of higher instantaneous energy content. For instance, unlubricated Al generated 0.06 dB energy and 39.6 mm^3 volume loss under high load (Figure 53 (a)). In contrast, unlubricated Al generated 0.001 dB and 4.49 mm^3 volume loss under low load (Figure 53 (b)). The same correlation was observed for SS and PU. One exception to this observation was silicone oil lubricated Al, where high load resulted in a smaller energy of 0.0015 dB with a volume loss of 2.45 mm^3 (Figure 53 (c)). compared to low load at 0.03 dB with a volume loss of 0.816 mm^3 (Figure 53 (d)). Interestingly, for all three types of materials without lubrication, increased load resulted in increased volume loss and increased instantaneous energy content in the lower frequency ranges at 0 - 0.5 MHz for Al (Figure 53 (a)&(b)), 0 - 0.25 MHz for SS (Figure 54 (a)&(b)), and 0 - 0.5 MHz for PU-lined Al (Figure 55(a)&(b)), respectively.

(a)
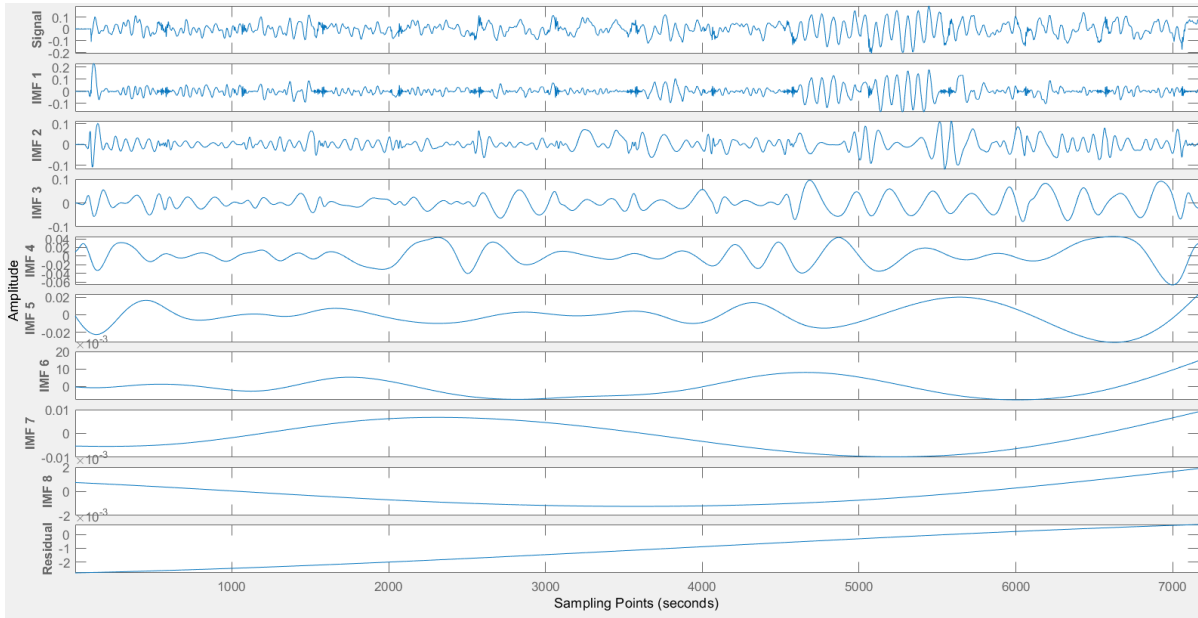
(b)
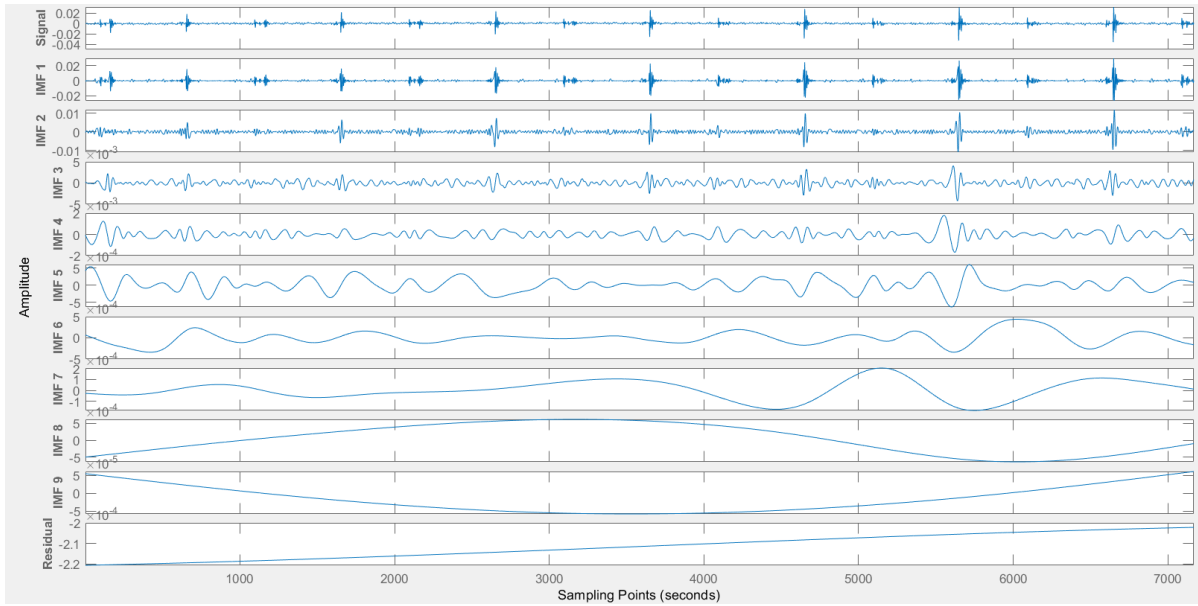
Figure 47. IMFs of unlubricated Al under high load (a) vs. low load (b).
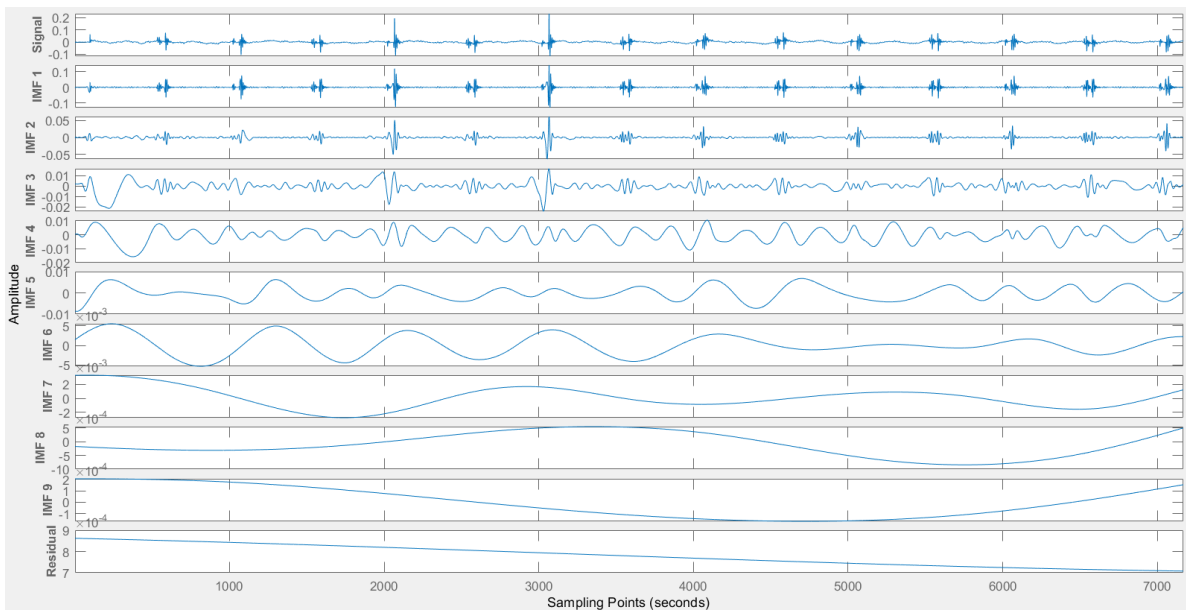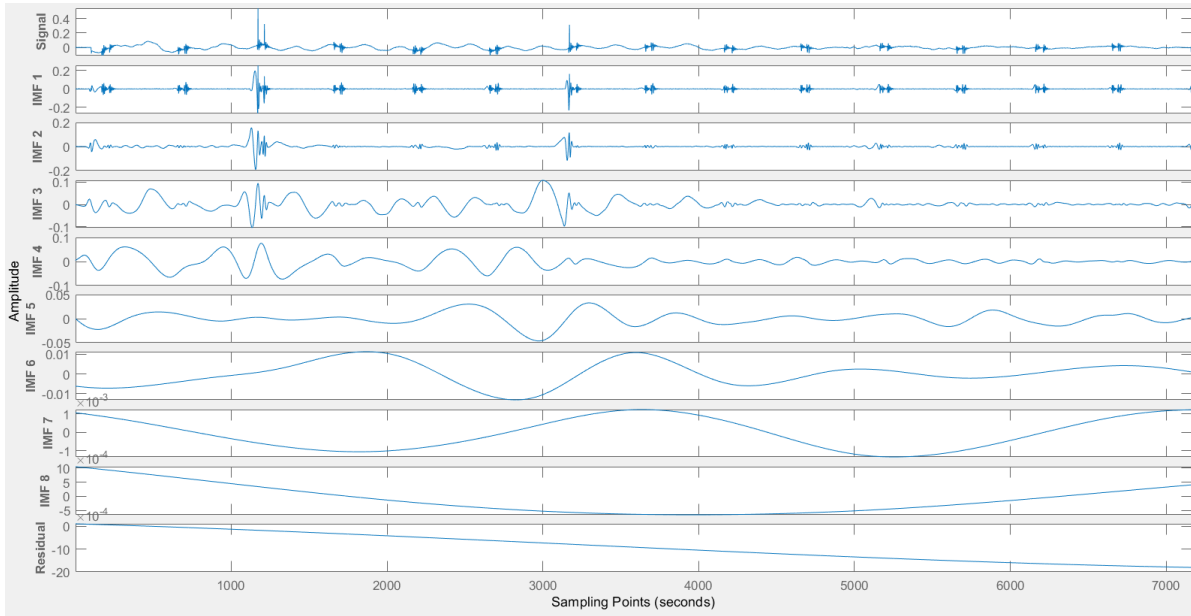
(a)
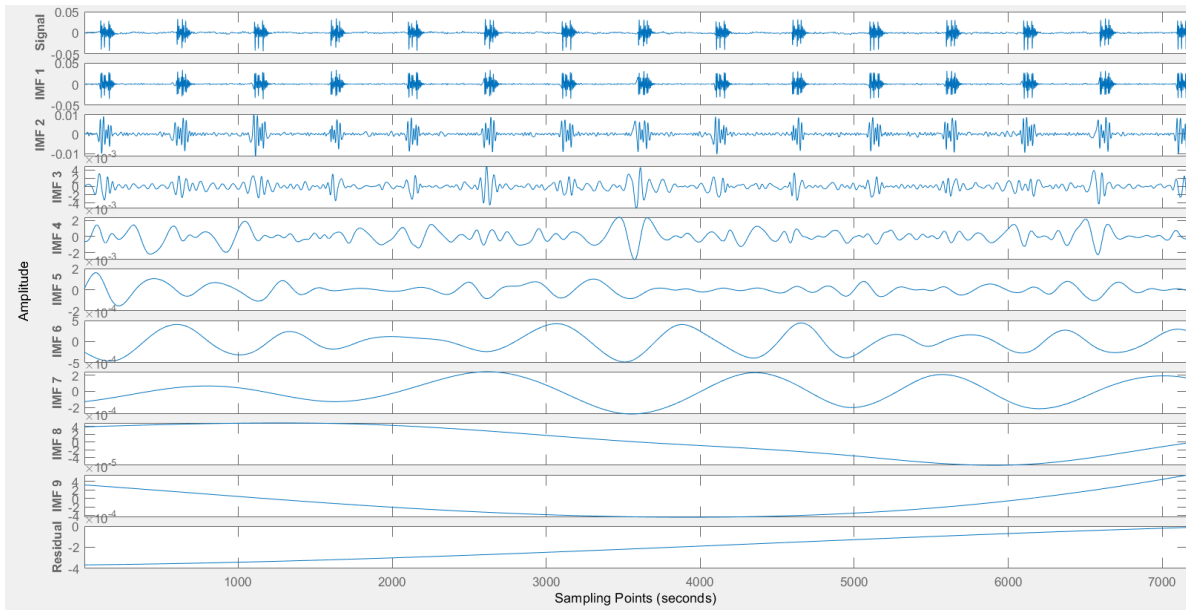
(b)

Figure 48. IMFs of silicone oil lubricated Al under high load (a) vs. low load (b).
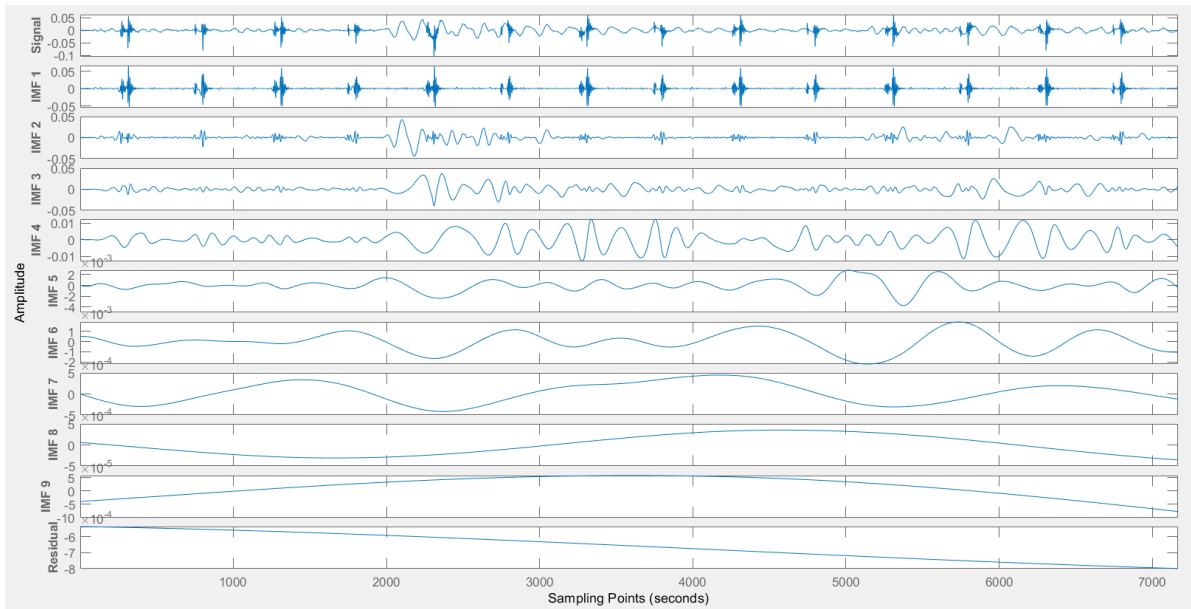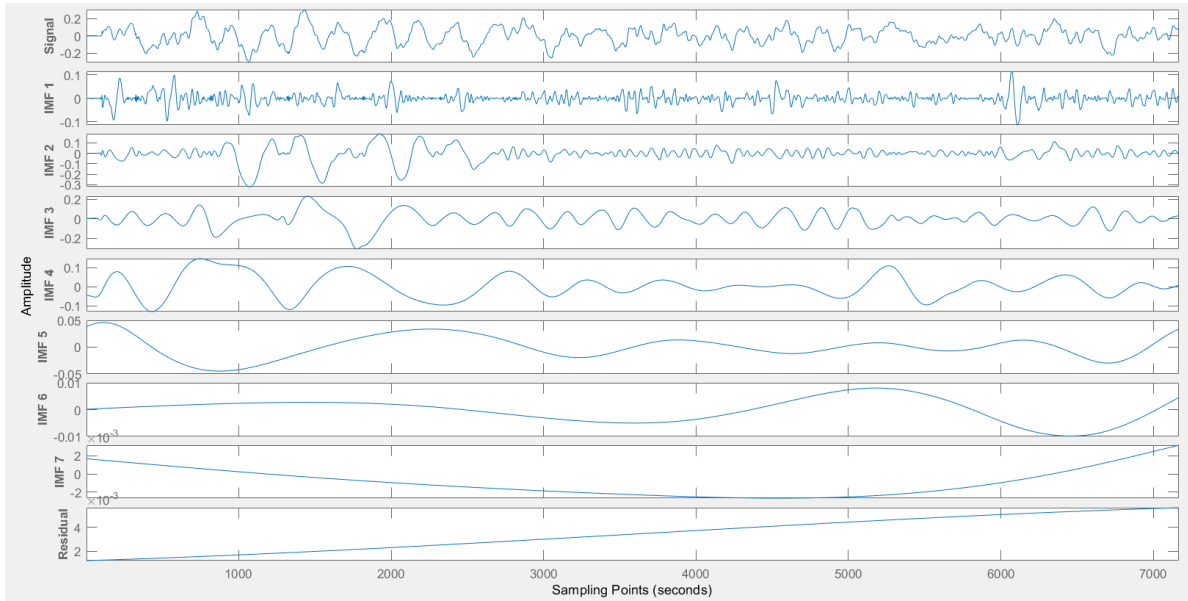
(a)

(b)

Figure 49. IMFs of water lubricated Al under high load (a) vs. low load (b).
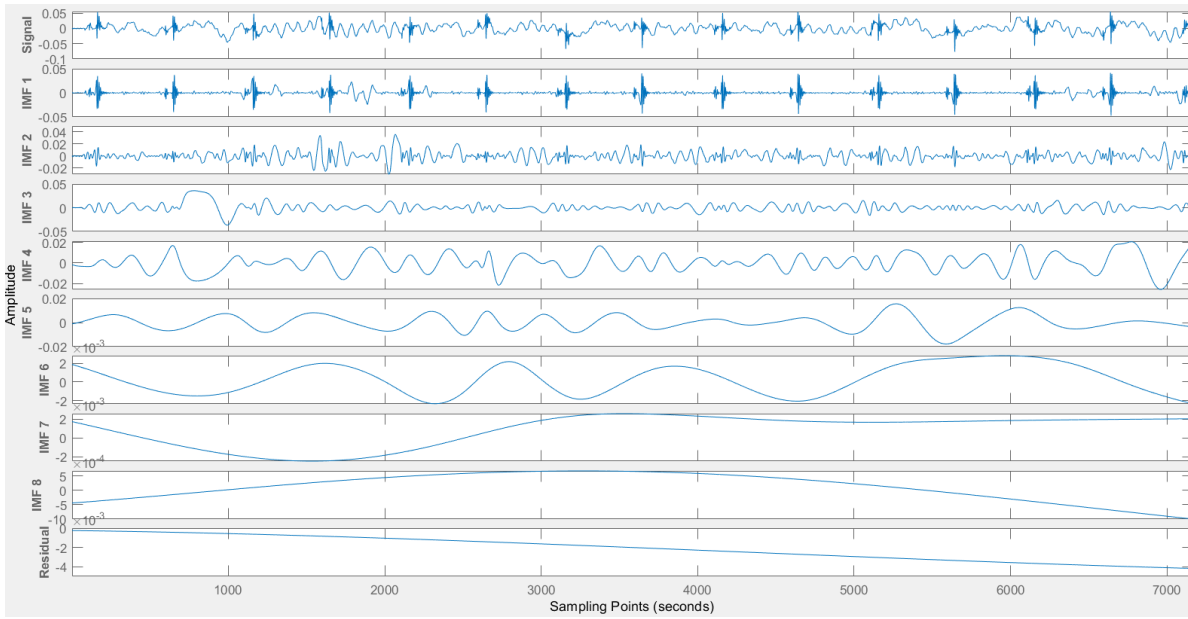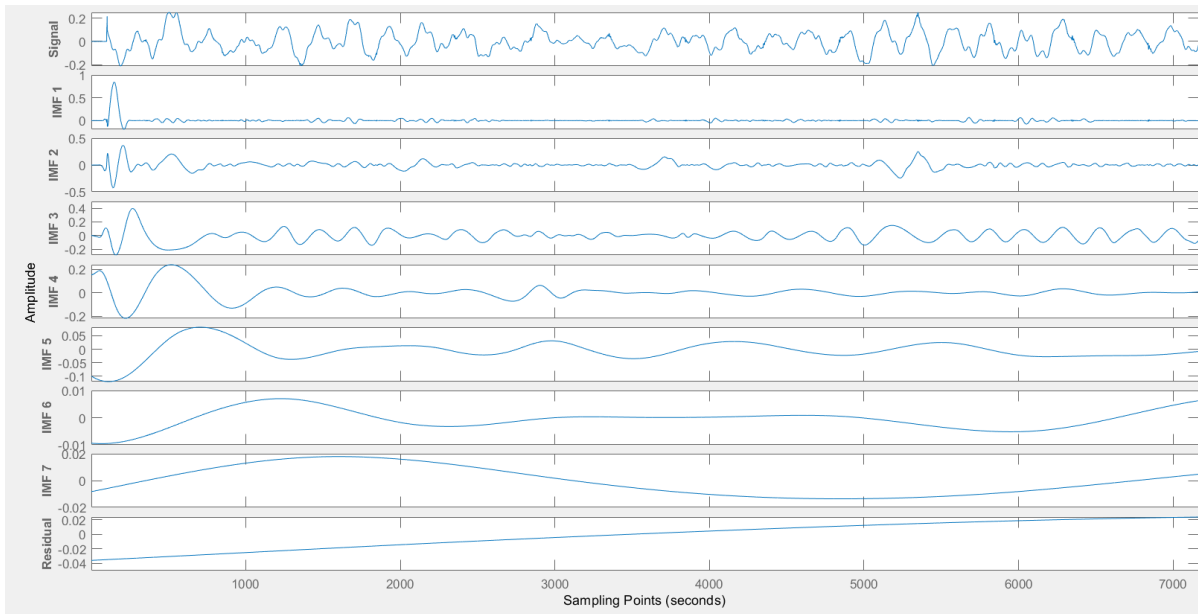
(a)

(b)

Figure 50. IMFs of unlubricated SS under high load (a) vs. low load (b).
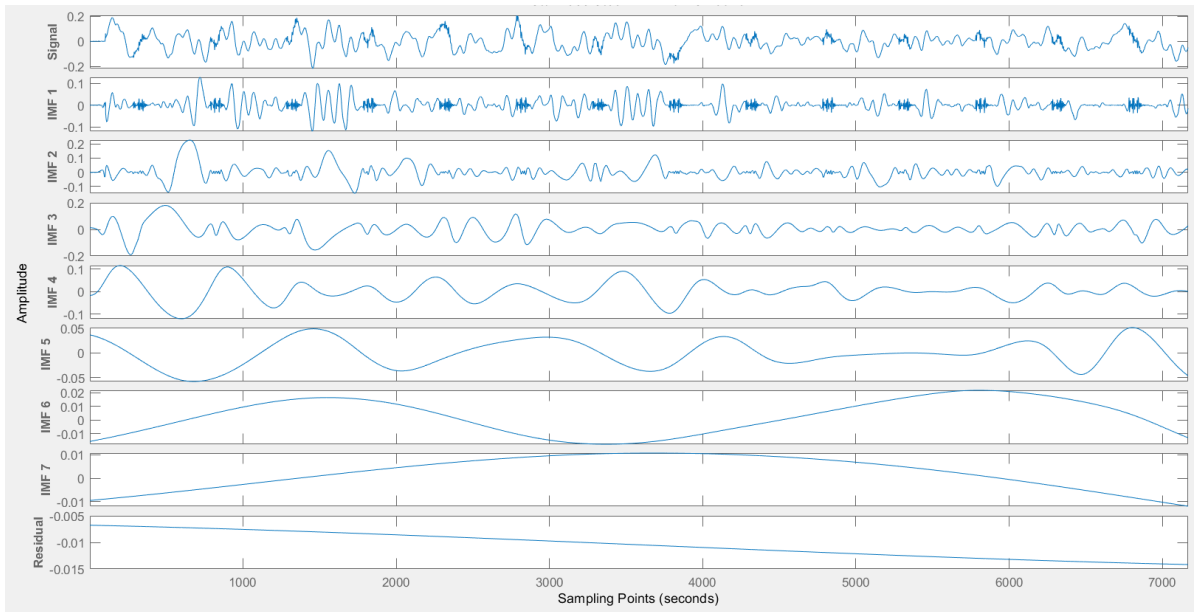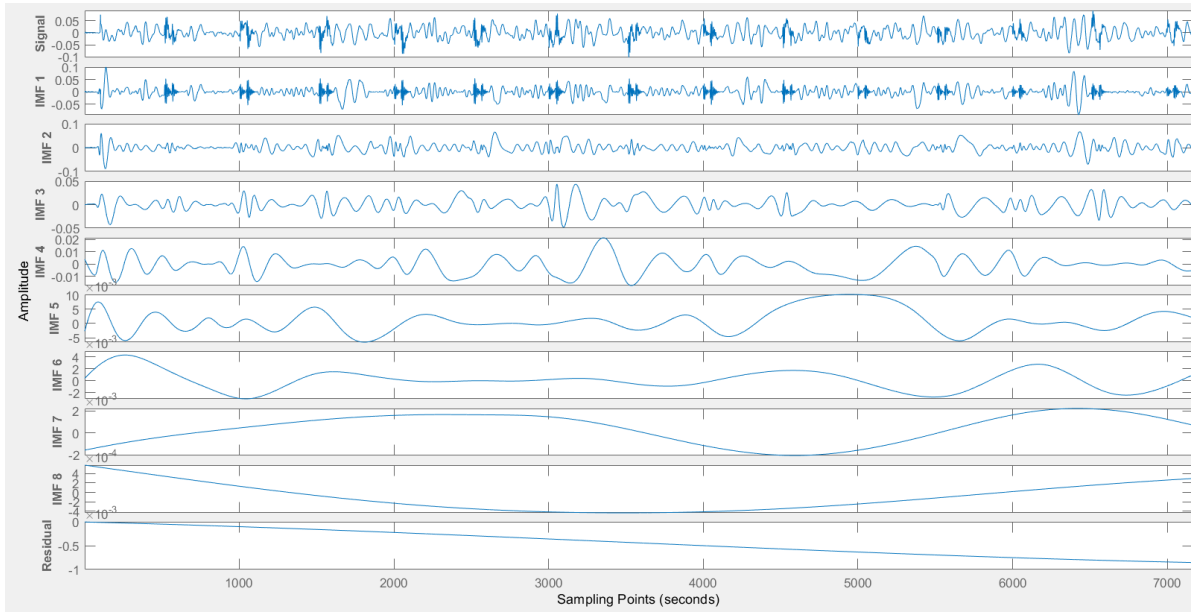
(a)

(b)

Figure 51. IMFs of silicone oil lubricated SS under high load (a) vs. low load (b).
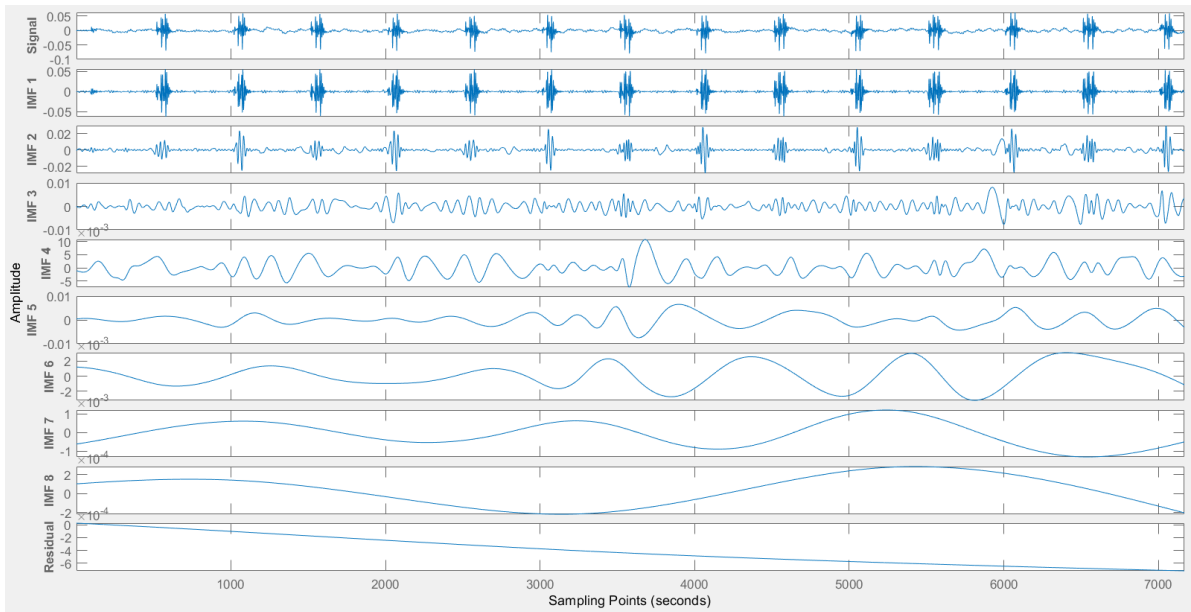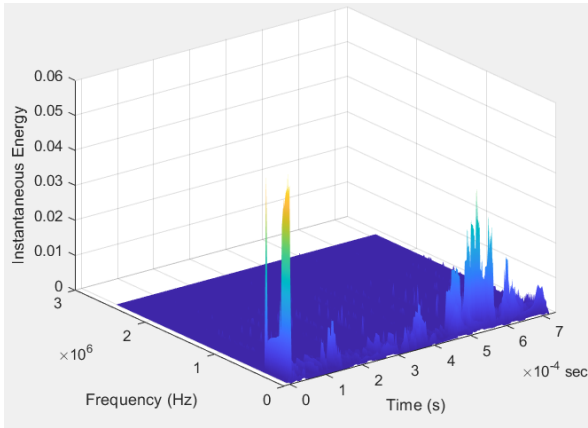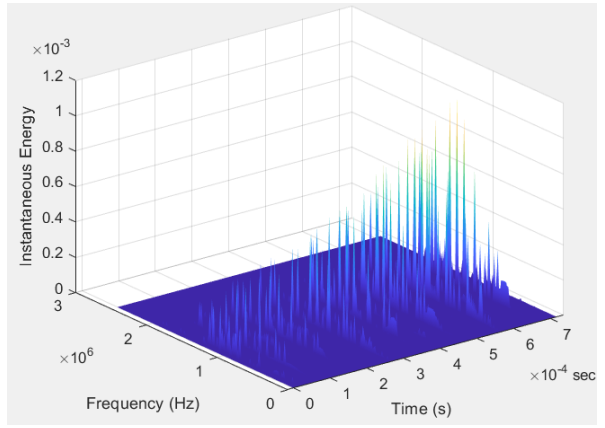
(a)

(b)

Figure 52. IMFs of unlubricated PU-lined Al under high load (a) vs. low load (b).
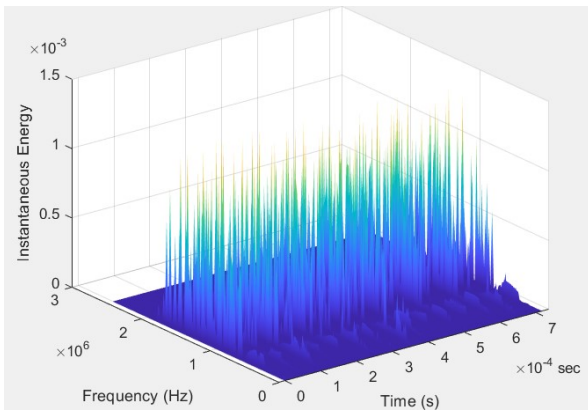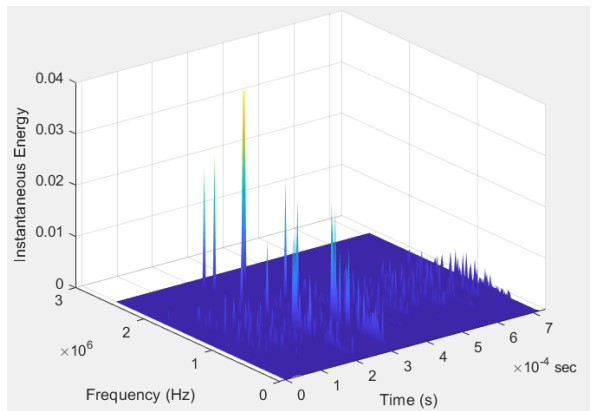
(a) Volume Loss: 39.6 *mm³*

(b) Volume Loss: 4.49 *mm³*

(c) Volume Loss: 2.45 *mm³*

(d) Volume Loss: 0.816 *mm³*

(e) Volume Loss: 25.7 *mm³*
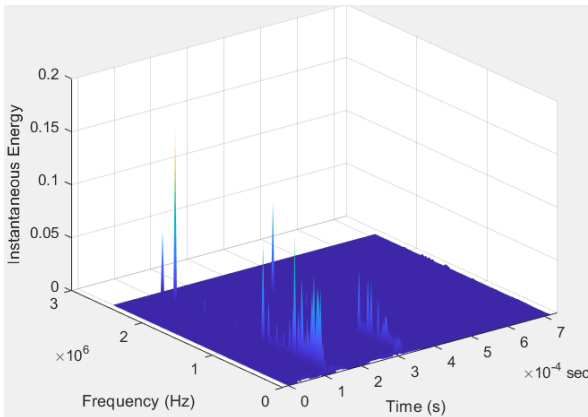
(f) Volume Loss: 3.27 *mm³*
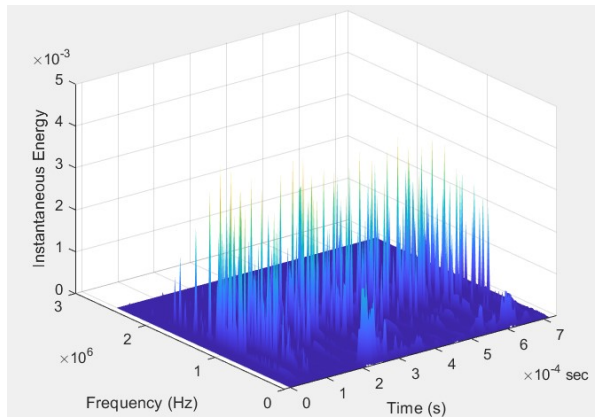
Figure 53. Mesh Hilbert spectra of Al under (a) high load/no lubricant; (b) low load/no lubricant; (c) high load/silicone oil; (d) low load/silicone oil; (e) high load/water and (f) low load/water.

(a) Volume Loss: 2.26 *mm³*   (b) Volume Loss: 0.425 *mm³*
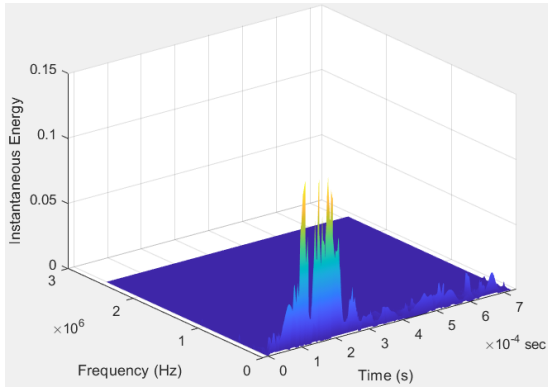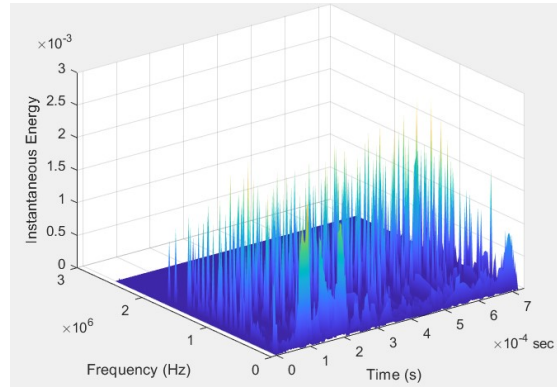
(c) Volume Loss: 2.69 *mm³*   (d) Volume Loss: 0.425 *mm³*
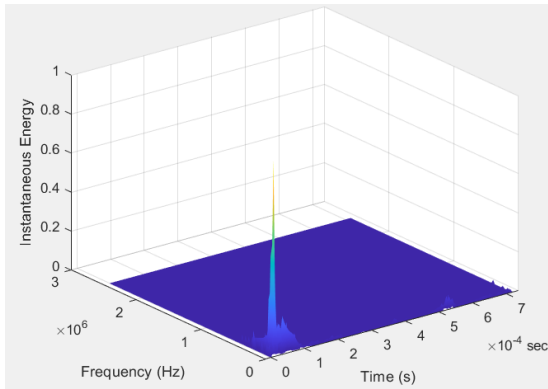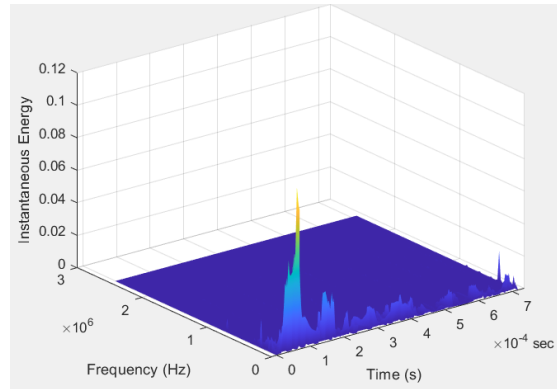
Figure 54. Mesh Hilbert spectra of SS under (a) high load/no lubricant; (b) low load/no lubricant; (c) high load/silicone oil and (d) low load/silicone oil.

(a) Volume Loss: 25.3 *mm³*   (b) Volume Loss: 3.79 *mm³*
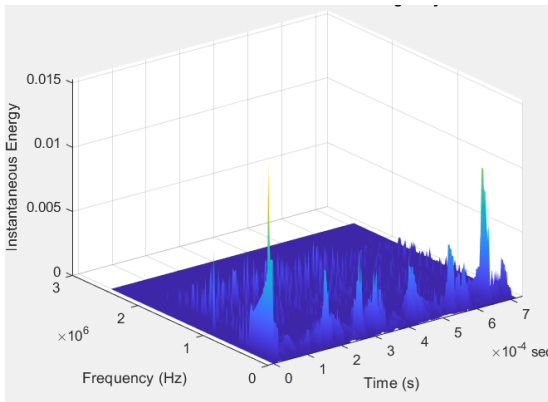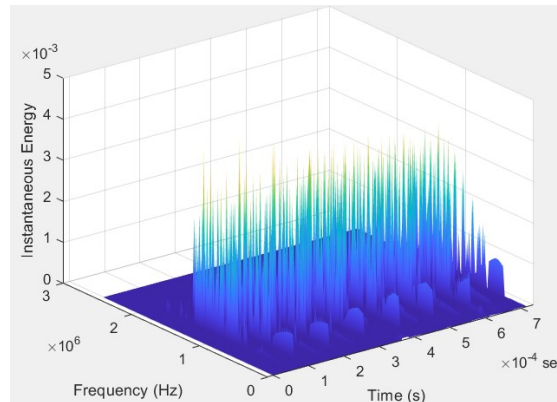
Figure 55. Mesh Hilbert spectra of PU-lined Al under (a) high load/no lubricant and (b) low load/no lubricant.

c. Statistical analysis

MATLAB was used to calculate variance, skewness, and kurtosis for the 10 MHz AE burst data on an assumed β distribution. Variance, skewness, and kurtosis were plotted against time. The plots below illustrated the difference in the AE RMS distribution for Al, SS and PU under various conditions.

(a)
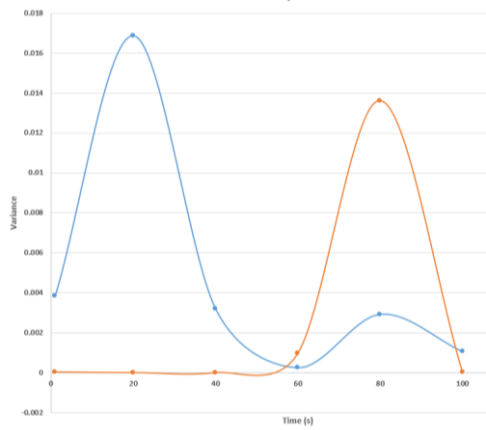
(b)
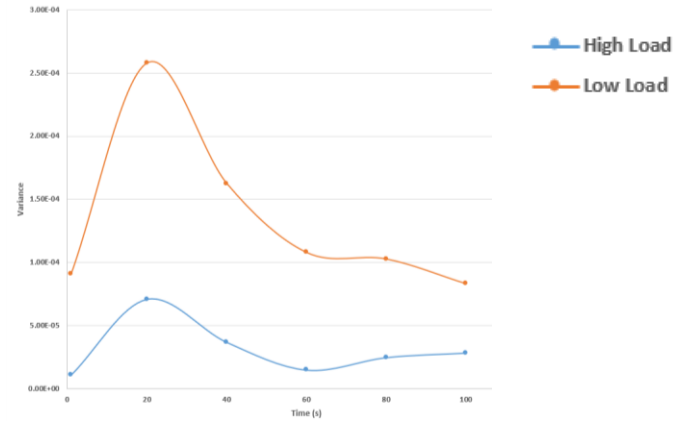
(c)
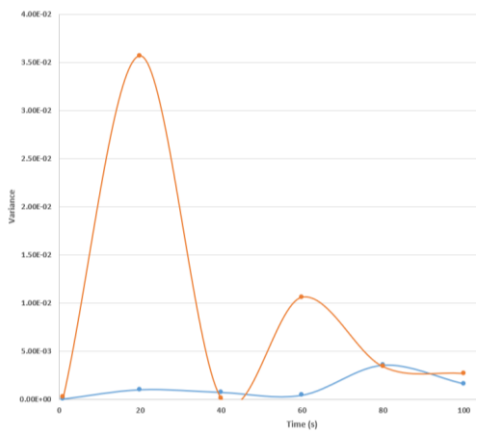
(d)
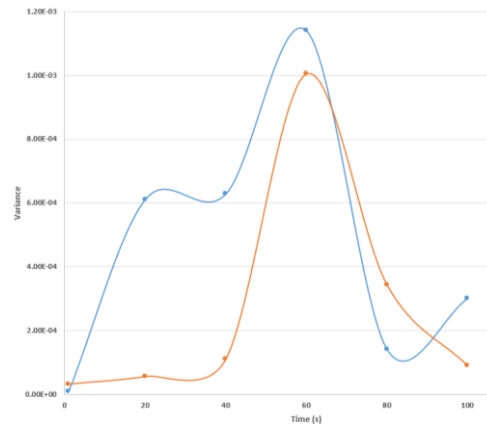
(e)
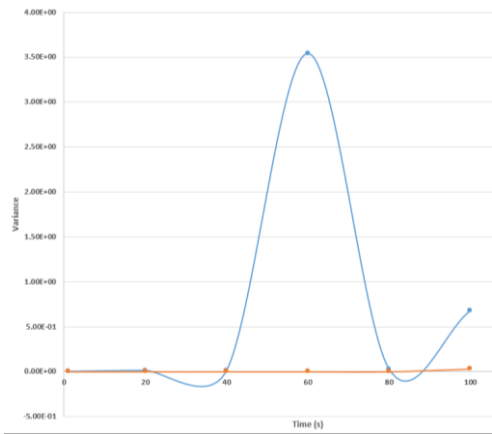
(f)
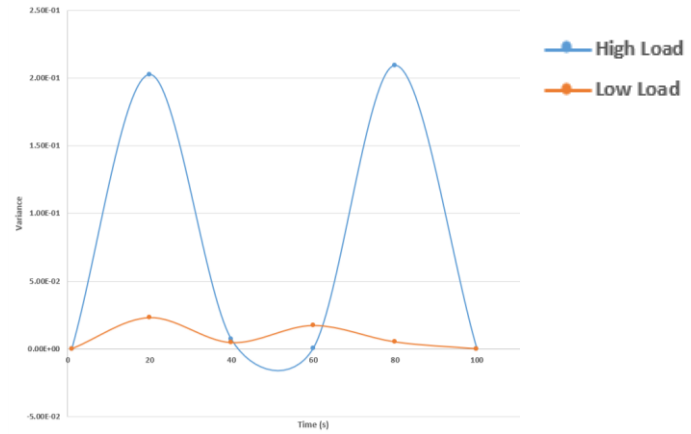
Figure 56.Variance as a function of sliding time for (a) dry Al; (b) silicone-coated Al; (c) water-coated Al; (d) dry PU; (e) dry SS; and (f) silicone-coated SS.

(a)

(b)

(c)

(d)

(e)

(f)
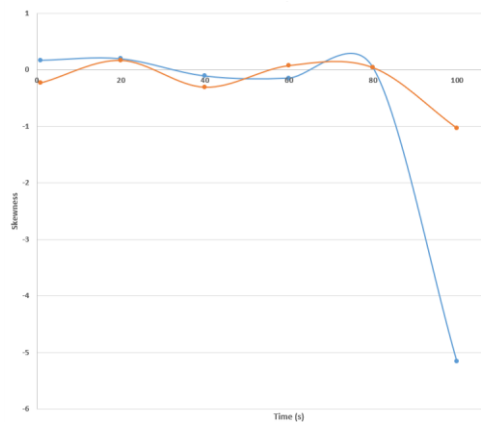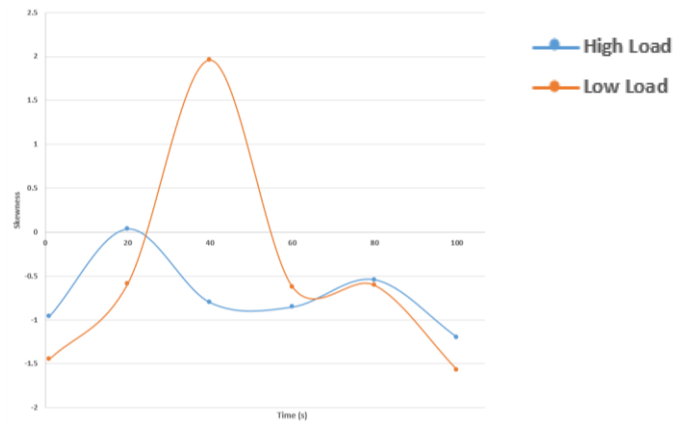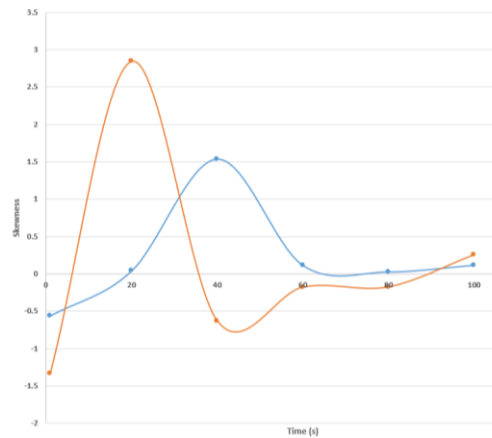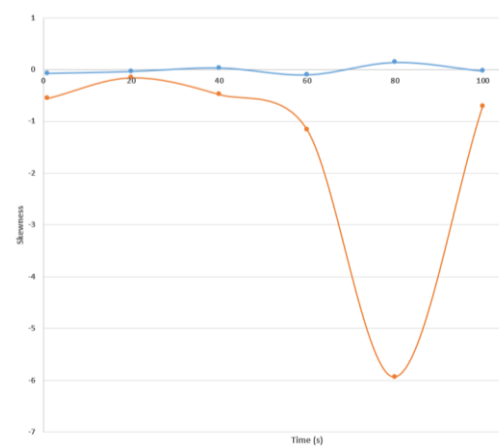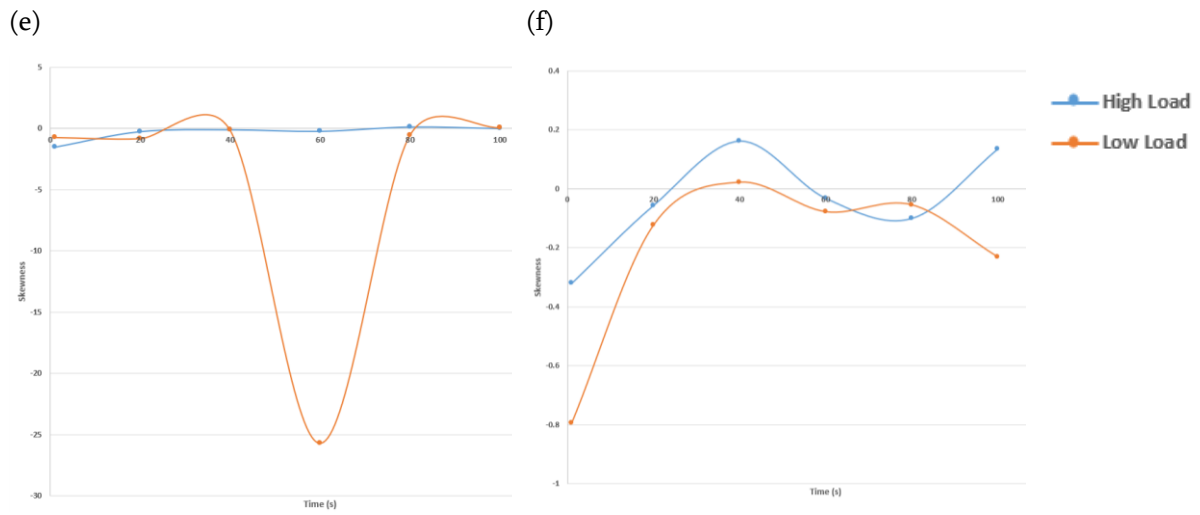
Figure 57.Variation of skewness as a function of sliding time for (a) dry Al; (b) silicone-coated Al; (c) water-coated Al; (d) dry PU; (e) dry SS; and (f) silicone-coated SS.

(a)

(b)
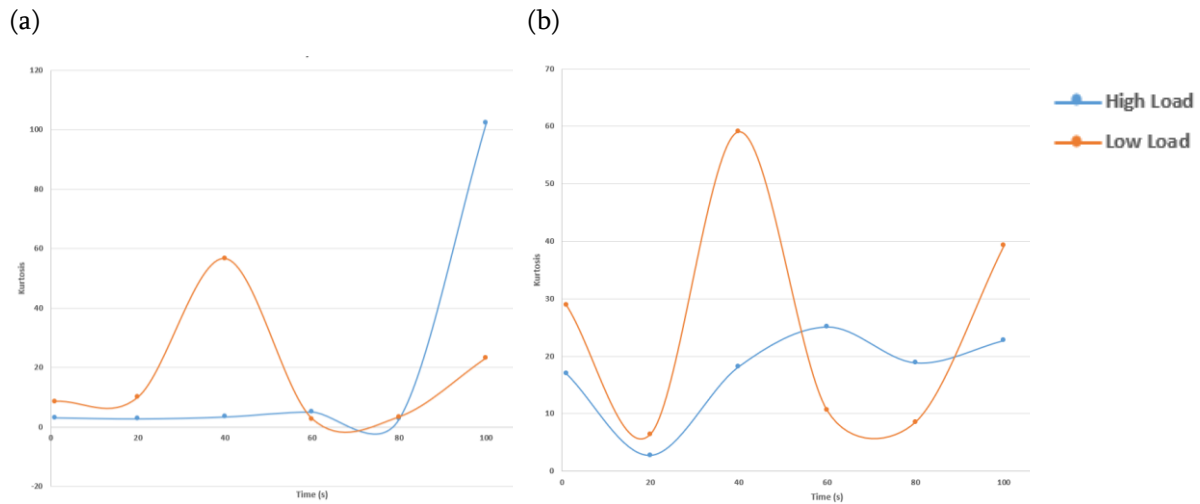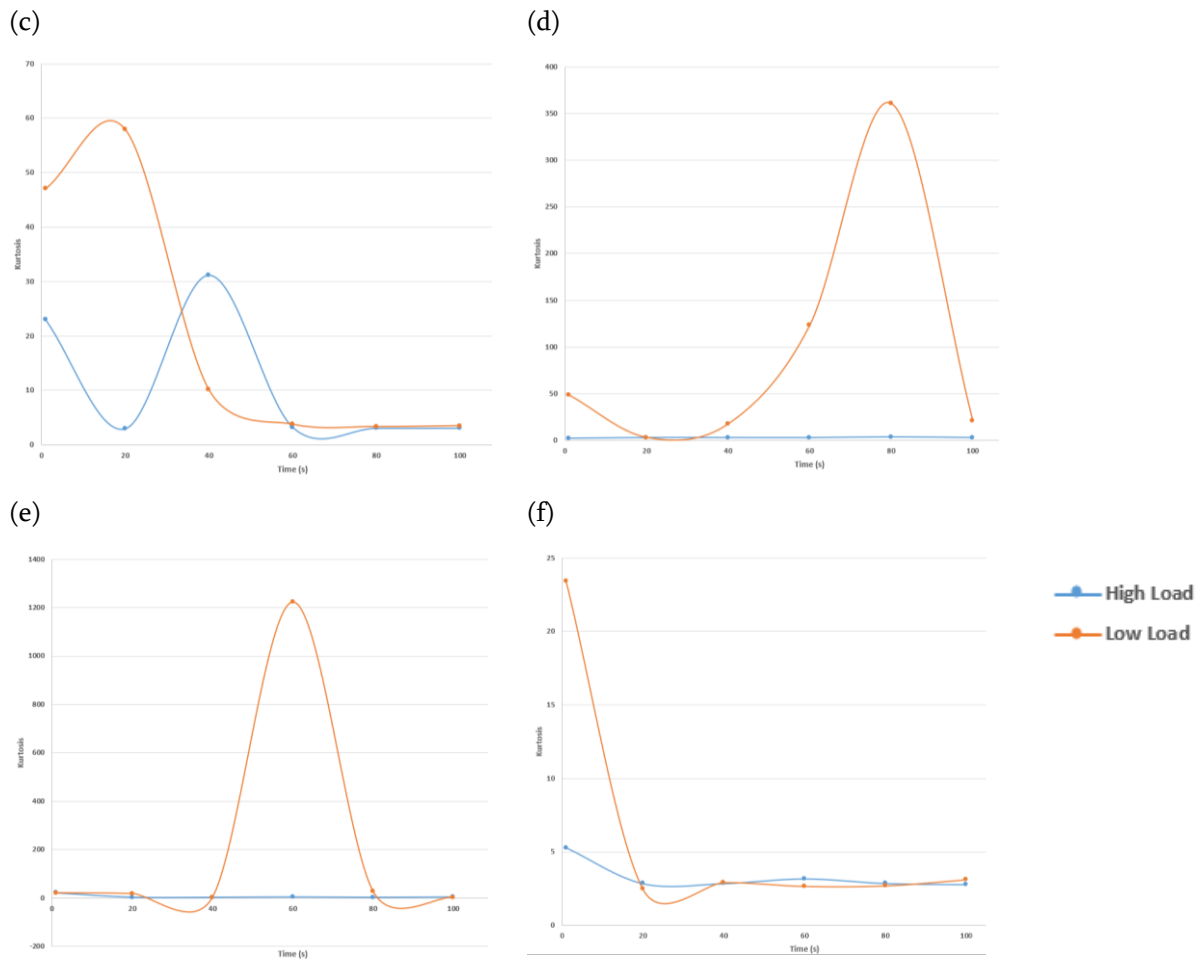
Figure 58. Variation of kurtosis as a function of sliding time for (a) dry Al; (b) silicone-coated Al; (c) water-coated Al; (d) dry PU; (e) dry SS; and (f) silicone-coated SS.

The S and K values were also correlated to the volume loss previously reported in the table below (Table 4). Under high load and without lubrication, Al experienced the most volume loss and this correlated with the highest K value and negative S value observed. On the other, unlubricated SS under low load resulted the least volume loss and it corresponded the lowest K value and positive S value observed.

Table 4. Values of skewness (S) and kurtosis (K) for different volume loss (V, mm3)

	Al						SS				PU	
	Dry		Silicone		Water		Dry		Silicone		Dry	
	H	L	H	L	H	L	H	L	H	L	H	L
$V\ (mm^3)$	39.6	4.49	2.45	0.816	25.7	3.27	2.26	0.425	2.69	0.425	25.3	3.79
S	-5.16	-1.03	-1.20	-1.57	0.116	0.255	-0.009	0.080	0.135	-0.232	-0.030	-0.705
K	102	23.2	22.7	39.3	3.06	3.50	4.45	2.65	2.79	3.12	3.10	20.9
K/V	2.6	5.2	9.3	48	0.14	1.1	2.0	6.2	1.0	1.2	0.12	5.5

d. Uncertainty analysis

Type A and type B uncertainties associated with the AE energy measurement were determined. The main source of error can arise from coupling the AE sensor to the test plates. The sensor was mounted after proper cleaning of the test plates and all experiments for the same type of materials were conducted by keeping the sensor at the same location. Therefore, any variation in AE signal due to mounting of the sensor was eliminated.

As described in the section above, the AE energy recorded in the burst data were assumed to follow a β distribution that was proportional to the integral of the square of the transducer output voltage (Wadley, Scruby, & Speak, 1980). For each volume loss, mean AE energy (at 100 s) was associated with a standard deviation. This is known as type A uncertainty:

$$u_c(E) = \frac{s}{\sqrt{c}} \tag{44}$$

where s is the estimated standard deviation and c is the number of measurements in the dataset. In this case, c is equal to 7168.

Type B uncertainty can arise from the signal analyzer of the AE sensor, and it is characterized by homogenous rectangular distribution (Keprt & Benes, 2009), which does not change with repeated measurements. It is determined by:

$$u_c(R) = \frac{a}{\sqrt{3}} \tag{45}$$

where a is the semi-range between the upper and lower limit of the rectangular distribution. The 1283 USB AE Node acquisition system has a resolution of 16 bit for the AE parametric input with a range of -10V to 10V. Therefore,

$$a = \frac{20}{65536} \tag{46}$$

The combined standard uncertainties were calculated through summation in quadrature using the following equation:

$$u_c(C) = \sqrt{u_c(E)^2 + u_c(R)^2} \tag{47}$$

The results are summarized in Table 5 below.

Table 5. Values of type A uc(E), type B uc(R) and combined uncertainties uc(C) for different volume loss.

| | Al | | | | | | SS | | | | PU | |
| | Dry | | Silicone | | Water | | Dry | | Silicone | | Dry | |
	H	L	H	L	H	L	H	L	H	L	H	L
V (mm^3)	39.6	4.49	2.45	0.816	25.7	3.27	2.26	0.425	2.69	0.425	25.3	3.79
$u_c(E)$	0.362	2.034	2.212	1.294	0.292	0.228	0.014	0.066	1.129	1.809	0.681	1.240
$u_c(R)$	0.0002	0.0002	0.0002	0.0002	0.0002	0.0002	0.0002	0.0002	0.0002	0.0002	0.0002	0.0002
$u_c(C)$	0.362	2.034	2.212	1.294	0.292	0.228	0.014	0.066	1.129	1.809	0.681	1.240

iv.   Limitations

This study has four main limitations. First, the continuous AE data was acquired by a 1283 AE node with a frequency of 10 MHz. According to the Nyquist-Shannon sampling theorem, such an acquisition frequency was only able to capture AE signals with a frequency up to 5 MHz and those that were emitted at a frequency above this threshold, if any, were not obtained. A

higher continuous acquisition frequency may provide additional insight about the wear processes.

Second, the duration of tests performed on the ball-on-plate device designed in this study was 120 s each. A longer test period would theoretically result in more severe wear and consequently, larger mass loss and volume loss, which should improve the accuracy of the wear characterization through mass loss. However, in practice, approximately 500 files with an average size of 500 MB each were acquired. The author had to limit the tests to 120 s due to the large file size and the computation speed of MATLAB.

Third, the scale used to weigh the test specimens had an accuracy of 0.01 g, close to the mass loss range for stainless steel. Small mass loss combined with insensitive measurement device consequentially entailed low precision in mass loss determination.

Lastly, since this abrasion test did not attempt to duplicate all of the conditions that may be experienced in service (for example, abrasive particle size, shape, hardness, speed, load, and presence of a corrosive environment for an oil sand pipeline), there is no assurance that this test method will predict the wear rate of a given material under conditions differing from those employed in this study.

V. Conclusions and Recommendations for Future Work

The present thesis developed an automated ball-on-plate abrasive wear tester and examined the material abrasion wear resistance by volume loss and their acoustic emission characteristics. The performance of three types of materials, including aluminum, polyurethane-coated aluminum and stainless steel, were investigated. Friction and wear testing were carried out under different experimental conditions. Three levels of normal load at approximately 20, 15 and 10 N and three types of lubrication conditions using water, silicone oil and no lubricant were tested. An average sliding velocity of 0.418 m/s and a test duration of 120 s were employed, achieving a total sliding distance of 50.2 m. Two types of acoustic emission data were acquired, including continuous data at 50 Hz and bursts data at 10 MHz.

The investigations found that the volume loss due to sliding abrasion for aluminum and stainless steel was inversely proportional to the hardness and proportional to the normal load, which is consistent with Archard's equation. Polyurethane, when used as a protective film on aluminum, reduced volume loss due to its high elastic deformability. Overall, stainless steel showed the least volume loss and, thus, the highest abrasion wear resistance. This was followed by polyurethane and aluminum with aluminum being the least wear resistant. In addition, AE RMS analysis, FFT transformation and correlation with friction force was performed for 50 Hz continuous data. For the 10 MHz burst data, FFT power spectra in dB scale, statistical analysis on an assumed β distribution and uncertainty analysis were demonstrated. Furthermore, HHT analysis was applied to the burst data acquired at 40 s, demonstrating distinguishing patterns in the Hilbert spectra characteristic of material type, normal load and lubrication conditions. These AE characteristics can potentially be used for abrasion wear monitoring. And examination of different types of materials, particle sizes and particle geometries would further our understanding of acoustic emission characteristic of abrasive wear.

The ball-on-plate testing developed in this thesis is simple, inexpensive to build and fully automated. This method is useful for screening materials for use in oil pipelines or machinery that are subjected to abrasion from coarse particles being transported or worked. It can be

primarily used to predict the relative ranking abrasion wear resistance of different materials and to characterize acoustic emission behaviors.

The idealized laboratory method presented here indicates that AE can be used for monitoring wear; but further tests are needed with more realistic contact scenarios to determine the efficacy of the method in industrial practice. As well, to apply the AE techniques developed here in an industrial setting, it is important to reduce the processing power and memory required to process and analyze the data so that it can be incorporated into an embedded system as an instrument. One way to achieve this would be to use analog filters (physical circuits composed of resistors, capacitors, inductors, and operational amplifiers) to preprocess the AE data in conjunction with an optimized AE processing technique. With this additional development and characterization, AE may be useful as a wear monitoring technique.

References

A.Maričić, M.Spasojević, A.Kalezić-Glišović, L.Ribić-Zelenović, S.Djukić, & N.Mitrović. (2012). The stress effect on electrical resistivity sensitivity of FeBSiC amorphous ribbon. *Sensors and Actuators A: Physical* , 103-106.

A.S.M. Handbook vol. 18. (1992). ASM International.

Affatato, S., & Brando, D. (2013). Introduction to wear phenomena of orthopaedic implants. In *Wear of Orthopaedic Implants and Artifical Joints.* Woodhead Publishing.

Affatato, S., & Brando, D. (2013). *Wear of Orthopaedic Implants and Artificial Joints.*

Affonso. (2006). 6. Wear. In *Machinery Failure Analysis Handbook* (pp. 55-82). Elsevier.

Amontons, G. (1706). De la resistance caus"ee dans les machines. *Mémoires de l'Académie Royale, A, Chez Gerard Kuyper*, 257–282.

Aravind, B., Jacob, P. R., & Mohamed, Y. J. (2017). Wear behaviour of Polyurethane Coated Aluminium Alloy (7075) with the influence of Multi-walled Carbon Nanotubes. *International Journal of Innovative Research in Science, Engineering and Technology*, 1622-1629.

Arnell, D. (2010). 2 - Mechanisms and laws of friction and wear. In H. Rahnejat, *Tribology and Dynamics of Engine and Powertrain* (pp. 41-72). Woodhead Publishing Limited.

Ashrafizadeh, H., McDonald, A., & Mertiny, P. (2017). Erosive and Abrasive Wear Resistance of Polyurethane Liners. IntechOpen.

Ashrafizadeh, H., McDonald, A., & Mertiny, P. (2017). Erosive and Abrasive Wear Resistance of Polyurethane Liners. In Yilmaz, & Faris, *Aspects of Polyurethanes.* IntechOpen.

Atkins, M. (2016). Chapter 5 - Velocity Field Measurement Using Particle Image Velocimetry (PIV). In T. Kim, T. J. Lu, & S. J. Song, *Application of Thermo-Fluidic Measurement Techniques* (pp. 125-166). Butterworth-Heinemann.

Bhushan, B. (1996). 4. Friction. In *Tribology and Mechanics of Magnetic Storage Devices* (pp. 232-365). Springer.

Birring, A., & Kwun, H. (1989). Ultrasonic measurement of wear. *Tribology International*, 33-37.

Blau, P. J. (1996). 4. Fundamentals of sliding friction. In *Friction Scient and technology: From Concepts to Applications.* New York: Marcel Dekker.

Bogdanovich, P., & Tkachuk, D. (2009). hermal and thermomechanical phenomena in sliding contact. *Wear*, 153-163.

Brunskill, H., Harper, P., & Lewis, R. (2015). The real-time measurement of wear using ultrasonic reflectometry. *Wear*, 332-333.

Budinski, K. G. (2011). Abrasive Wear Testing. In *Guide to Friction, Wear, and Erosion Testing: (MNL 56)* (pp. 33-44). ASTM International.

Budinski, K. G. (2011). Erosion Testing. In *Guide to Friction, Wear, and Erosion Testing: (MNL 56)* (pp. 86-94). ASTM International.

Chong, K. P., & Carino, N. J. (2003). Health monitoring of civil infra- structures. *Smart Materials and Structures*, 483-493.

Chong, K. P., & Liu, S. C. (2003). *Intelligent Structure.* London, New York.: Applied Science.

Chong, K. P., Dillon, O. W., Scalzi, J. B., & Spitzig, W. A. (1994). Engineering research in composite and smart structures. *Composites Engineering*, 829–852.

Chowdhury, M., Khalil, M., Nuruzzaman, D., & Rahaman, M. (2011). The Effect of Sliding Speed and Normal Load on Friction and Wear Property of Aluminum. *International Journal of Mechanical & Mechatronics Engineering*, 45-49.

Comparing Common File I/O and Data Storage Approaches. (2019, March 14). Retrieved from National Instruments: https://www.ni.com/en-us/innovations/white-papers/09/comparing-common-file-i-o-and-data-storage-approaches.html

Crosbya, S., Faya, R., Groarka, C., Kanib, A., Smithb, J. R., Sullivana, T., & Paviae, R. (2013). *Transporting Alberta Oil Sands Products: Defining the issues and assessing the risks.* NOAA Office of Response and Restoration.

Culshaw, B. (2006). Principles of fiber optic sensors. In B. P. Pal, *Guided Components and Devices* (pp. 371-387). Academic Press.

Curtis, J. S. (2008). Slurry Transport. In I. t. technology. Wiley.

Dakin, J., Pratt, D., Biddy, G., & Ross, J. (1988). Distributed optical fiber Raman temperature sensor using a semiconductor light source and detectors. *Electronics Letters*, 569–570.

Divakar, M., Agarwal, V., & Singh, S. (2005). Effect of the material surface hardness on the erosion of AISI316. *Wear*, 110-117.

Dyskin, A. V., Basarir, H., Doherty, J., Elchalakani, M., Joldes, G. R., Karrech, A., . . . Wittek, A. (2018). Computational monitoring in real time: review of methods and applications. *Geomechanics and Geophysics for Geo-Energy and Geo-Resources*, 235-271.

Feng, P., Borghesani, P., Smith, W., Randall, R., & Peng, Z. (2020). A Review on the Relationships Between Acoustic Emission, Friction and Wear in Mechanical Systems. *Applied Mechanis Review*, 020801-1 - 020801-17.

Figliola, R., & Beasley, D. (2011). *Theory and design for mechanical engineering, 5th ed.* John Wiley & Sons, Inc.

Freeman Manufacturing. (n.d.). Retrieved from https://www.freemansupply.com/tables/repro.htm

Hase, A. (2015). Acoustic emission during tribological processes. *Internatiaonl tribology conference*, (pp. 210-211). Tokyo.

Hase, A., Mishina, H., & Wada, M. (2016). Fundamental study on early detection of seizure in journal bearing by using acoustic emission technique. *Wear*, 346-347.

Hernández, H. H., Reynoso, A. M., González, J. C., Morán, C. O., Hernández, J. G., Ruiz, A. M., . . . Cruz, R. O. (2019). *Electrochemical Impedance Spectroscopy (EIS): A Review Study of Basic Aspects of the Corrosion Mechanism Applied to Steels.* IntechOpen. Retrieved from https://www.intechopen.com/books/electrochemical-impedance-spectroscopy/electrochemical-impedance-spectroscopy-eis-a-review-study-of-basic-aspects-of-the-corrosion-mechanis

Hokkirigawa, K., & Kato, K. (1988). An experimental and theoretical investigation of ploughing, cutting and wedge formation during abrasive wear. *Tribology International*, 51-57.

Holroyd, T. (2000). *The acoustic Emission & Ultrasonic Monitoring Handbook.* Oxford, UK: Coxmoor Publishing Company.

Horiguchi, T., Kurashima, T., & Tateda, M. (1990). Distributed temperature sens- ing using stimulated Brillouin scattering in optical silica fibers. *Optics Letters*, 1038–1040.

Huang Norden E., S. Z.-C. (1998). The empirical mode decomposition and the Hilbert spectrum for nonlinear and non-stationary time series analysis. *Proc. R. Soc. Lond. A.*, 903–995.

Hydrotranport Explained. (n.d.). Retrieved from oilsandsmagazine: www.oilsandsmagazine.com/technical/mining/hydrotransport

Jiménez, A. E., & Bermúdez, M. D. (2011). Friction and Wear. In J. P. Davim, *Tribology for Engineers A Practical Guide* (p. 56). Elsevier.

Jiménez, A., & Bermúdez, M. (2011). 2 - Friction and wear. In *Tribology for Engineers - A Practical Guide* (pp. 33-63). Woodhead Publishing.

Jiménez, A., & Bermúdez, M. (2011). 2 - Friction and wear. In *Tribology for Engineers - A Practical Guide* (pp. 33-63). Woodhead Publishing.

Kannatey-Asibu Jr, E., & Dornfield, D. A. (1982). A study of tool wear using statistical analysis of metal-cutting acoustic emission. *Wear*, 247-261.

Keprt, J., & Benes, P. (2009). Determination of uncertainty in calibratin of acoustic emission sensors. *International J. of Microstructure and Material Properties*, 85-103.

Kermani, B., & Smith, L. M. (1997). *A Working Party Report on CO2 Corrosion Control in Oil and Gas Production: Design Considerations.* Institutes of Materials.

Kersey, A. D., Davis, M. A., Patrick, H. J., Leblanc, M. J., Koo, K. P., Askins, C. G., . . . Friebele, E. J. (1997). Fiber grating sensors. *Journal of Lightwave Technology*, 1442-1463.

Magerstädt, D. M. (2013). Field Experience with Interior Pipe Coatings from High Performance Polyurethane Elastomers. *Pipeline Technology Conference 2013.* Berlin, Germany.

MathWorks, Inc. (2021, May 17). *Help Center emd*. Retrieved from The MathWorks, Inc.: https://www.mathworks.com/help/signal/ref/emd.html#:~:text=The%20empirical%20 mode%20decomposition%20(EMD,maxima%20of%20x(t)

Matsuoka, K., Forrest, D., & Tse, M. (1993). Online wear monitoring using acoustic emission. *Wear*, 605-610.

Menezes, P., Kishore, S., & Kailas. (2009). Influence of Surface Tex ture and Roughness Parameters on Friction and Transfer Layer Formation During Sliding of Aluminium Pin on Steel Plate. *Wear*, 1534-1549.

MEO, M. (2014). Acoustic emission sensors for assessing and monitoring civil infrastructures. In *Sensor technologies for civil infrastructures. Volume 1, Sensing hardware and data collection methods for performance assessment* (pp. 158-178). Cambridge U.K.; Waltham, Mass.: Woodhead.

Merriam-Webster. (n.d.). Retrieved from https://www.merriam-webster.com/dictionary/erode

Mikhin, N., & Lyapin, K. (1972). *Hardness dependence of coefficient of friction.* New York: Plenum Publishing Corporation.

Miller, J., & Schmidt, . (1987). The SAR Number for Slurry Abrasion Resistance.

Mukhopadhyay, C. K., Jayakumar, T., Baldev, R., & Venugopal, S. (2012). Statistical Analysis of Acoustic Emission Signals Generated During Turning of a Metal Matrix Composite. *J. of the Braz. Soc. of Mech. Sci. & Eng.* , 145-154.

Nair, A., & Cai, C. (2010). Acoustic emission monitoring of bridges: Review and case studies. *Engeering Structures*, 32(6): 1704-1714.

Neville, A., Reza, F., Chiovelli, S., & Revega, T. (2005). Erosion–corrosion behaviour of WC-based MMCs in liquid–solid slurries. *Wear*, 181-195.

Nie, P., Dong, H., Chen, Y. H., Li, Z., & Gao, H. (2012). Feature analysis of tool wear states based on best wavelet packet and hilbert-huang transform. *IEEE*, 2371-2365.

Niklès, M., Briffod, F., Burke, R., & Lyons, G. (2005). Greatly extended dis- tance pipeline monitoring using fibre optics,. *Proceedings of OMAE05 24th International Conference on Offshore Mechanics and Arctic Engineering.* Halkidiki, Greece.

Ojala, N., valtonen, K., Antikainen, A., Kemppainen, A., Minkkinen, J., Oja, O., & Kuokkala, V.-T. (2016). Wear performance of quenched wear resistant steels in abrasive slurry erosion. *Wear*, 354-355.

O'Keefe, C., Maron, R., Fernald, M., Bailey, T., & Van der Spek, A. (2009). New developments in velocity profile measurement and pipe wall wear monitoring for hydrotransport lines. *The 41. annual meeting of the Canadian Mineral Processors*, (pp. 459-475). Ottowa, ON (Canada).

Pagalthivarthi, K., & Helmly, F. (1992). Applications of materials wear testing to solids transport via centrifugal slurry pumps. In *Wear Testing of Advanced Materials* (pp. 114-126). Philadephia: American Society for Testing and Materials.

Papavinasam, S., Doiron, A., Attard, M., & Demoz, A. (2012). Non-intrusive techniques to monitor internal corrosion of oil and gas pipelines. *NACE Corrosion 2012*, (p. Paper No. 0001261).

Parent, L., & Li, D. (2013). Wear of hydrotransport lines in Athabasca oil sands. *Wear*, 477-482.

Peker, S. M., Helvaci, S. S., Yener, H. B., Ikizler, B., & Alparslan, A. (2008). *Solid-Liquid Two Phase Flow.* Elsevier Science.

Peters, K., & Inaudi, D. (2014). Fiber optic sensors for assessing and monitoring civil infrastructures. In *Sensor Technologies for Civil Infrastructures, Volume 1: Sensing Hardware and Data Collection Methods for Performance Assessment* (pp. 121-158). Woodhead Publishing.

Poursaee, A. (2014). Corrosion sensing for assessing and monitoring civil infrastructures. In *Sensor technologies for civil infrastructures* (pp. 357-382). Woodhead .

Powell, D. (2015). Internal corrosion monitoring using coupons and ER probes. In *Oil and Gas Pipelines: Integrity and Safety Handbook* (pp. 495-514). John Wiley & Sons.

Rahi, K. H. (2016). *Design and construction of a strain gauge.* Sylhet Agricultural University.

Ramadan, S., Gaillet, L., Tessier, C., & Idrissi, H. (2008). Assessment of the stress corrosion cracking in a chloride medium of cables used in prestressed concrete structures by the acoustic emission technique. *Meas. Sci. Technol.*, 115702.

Rastegaev, I., Merson, D., Rastegaeva, I., & Vinogradov, A. (2020). A Time-Frequency Based Approach for Acoustic Emission Assessment of Sliding Wear. *Lubricatns*, 8(5).

Rice, H. P., Peakall, J., Fairweather, M., & Hunter, T. N. (2020). Extending estimation of the critical deposition velocity in solid–liquid pipe flow to ideal and non-ideal particles at low and intermediate solid volume fractions. *Chemical Engineering Science*.

Roco, M., & Addie, G. (1987). Erosion wear in slurry pumps and pipes. *Powder Technology*, 35-46.

Ruud, C. (2002). Measurement of Residual Stresses. In *Handbook of residual stress and deformation of steel* (pp. 99-117). ASM International.

Sadighian, A. (2016). *Investigating Key Parameters Affecting Slurry Pipeline Erosion.* Edmonton: University of Alberta.

Scully, J. R. (2000). Polarization resistance method for determination of instantaneous corrosion rates. *Corrosion*, 199-218.

Stachowiak, G. W. (2005). *Wear - Materials, Mechanisms and Practice.* John Wiley & Sons, Ltd.

Stachowiak, G. W., & Batchelor, A. W. (2014). *Engineering Tribology.* Butterworth-Heinemann.

Standard Terminology for Nondestructive Examinations. (1990). West Conshohocken: ASTM.

Stern, M., & Geary, A. (1957). Electrochemical polarisation: I. A theoretical analysis of the shape of polarisation curves. *Journal of The Electrochemical Society*, 56-63.

Takeuchi, K. (2001). Nonparametric Statistics: Asymptotics. *International Encyclopedia of the Social & Behavioral Sciences*, 10667-10673.

The Engineering Toolbox. (n.d.). Retrieved from https://www.engineeringtoolbox.com/linear-expansion-coefficients-d_95.html

Tian, H., Addie, G., & Barsh, E. (2007). A new impact erosion testing setup through Corriolis approash. *Wear*, 289-294.

Tsai, W.-h., Humphrey, J. A., Cornet, I., & Levy, A. V. (1981). Experimental measurement of accelerated erosion in a slurry pot tester. *Wear*, 289-303.

Tscheliesnig, P., Lackner, G., & Jagenbrein, A. (2016). Corrosion Detection by means of Acoustic Emission (AE) Monitoring. *19th Wolrd Conference on Non-Destructive Testing* (pp. 13-17). Munich: WCNDT.

Tuzson, J. (1984). Laboratory slurry erosion tests and pump wear calculations. *J. Fluids Eng.*, 135-140.

Tuzson, J., & Scheibe-Powell, K. (1984). Slurry erosion tests with centrifugal erosion tester. *Liquid-Solid Flows and Erosion Wear in Industrial Equipment*, 84-87.

Wadley, H. N., Scruby, C. B., & Speak, J. H. (1980). Acoustic Emission for Physical Examination of Metals. *Int. Metals Rev.*, 41-64.

Wang, M. L., & Sohn, H. (2004). Introduction to sensing for structural performance assessment and health monitoring. In *Thumbnail Sensor technologies for civil infrastructures. Volume 1, Sensing hardware and data collection methods for performance assessment* (pp. 1-22). Cambridge, UK; Waltham, US: Woodhead.

Webster, J., Dong, W., & Lindsay, R. (1996). Raw Acoustic Emission Signal Analysis of Grinding Process. *Center for Grinding Research and Development*.

Whitehouse, D. (1978). Beta functions for surface typology. *Ann CIRP*, 491-497.

Yang, G., Tsai, K., Serate, D., & Wu, M. (2018). *Wear Modeling of Dense Slurry Flow in Oil Sands Coarse Tailings (CT) Pipelines.* NACE International.

Ye, X. W., Su, Y. H., & Han, J. P. (2014). Structural Health Monitoring of Civil Infrastructure Using Optical Fiber Sensing Technology: A Comprehensive Review . *The Scientific World Journal*, 1-11.

Yu, B., Li, D., & Grondin, A. (2013). Effects ofthedissolvedoxygenandslurryvelocityonerosion–corrosion. *Wear*, 1609-1614.

Zhang, J., Kang, J., Fan, J., & Gao, J. (2016). Study on erosion wear of fracturing pipeline under the action of multiphase flow in oil & gas industry. *Journal of Natural Gas Science and Engineering*, 334-346.

Appendix I

Mass Loss Tables

Table 6. Mass loss by test material

Material	Min	1st Quantile	Median	Mean	3rd Quantile	Max
AL	-0.03333	-0.00667	0.00000	0.01833	0.02917	0.13667
SS	-0.03000	-0.00250	0.00500	0.00722	0.02000	0.03333
URAL	0.00000	0.00333	0.00333	0.01296	0.02000	0.04000

Table 7. Mass loss by lubrication

Lubrication	Min	1st Quantile	Median	Mean	3rd Quantile	Max
Dry	-0.03000	-0.00083	0.00500	0.01881	0.02750	0.13667
Silicon lubricant	-0.02000	-0.00333	0.00333	0.00482	0.01250	0.03333
Water	-0.03333	-0.01333	0.00000	0.01630	0.03667	0.09000

Table 8. Mass loss by normal force

Normal Force	Min	1st Quantile	Median	Mean	3rd Quantile	Max
High	-0.03000	-0.01000	0.03000	0.03772	0.0667	0.13667
Low	-0.03333	-0.00333	0.00333	0.00074	0.00333	0.02667
Medium	-0.02000	-0.00667	0.00000	0.00167	0.00667	0.03667

Appendix II

LabWindows code examples

2.1 Normal strain acquisition control

```
DAQmxErrChk( DAQmxCreateAIStrainGageChan( gTaskHandle, data[i].channel,
data[i].name, -0.0002, 0.0002, DAQmx_Val_Strain, DAQmx_Val_FullBridgeIII,
DAQmx_Val_Internal, 10.0, 2.17, 0.0, 350.0, 0.30, 0.0, "" ) ); //poisson ration SS .30 ,
aluminum 0.35
```

2.2 Shear strain acquisition control

```
DAQmxErrChk( DAQmxCreateAIStrainGageChan( gTaskHandle, data[i].channel,
data[i].name, -0.01, 0.01, DAQmx_Val_Strain, DAQmx_Val_FullBridgeI,
DAQmx_Val_Internal, 10.0, 2.17, 0.0, 350.0, 0.35, 0.0, "" ) ); //poisson ration SS .30 ,
aluminum 0.35
```

2.3 Potentiometer acquisition control

```
DAQmxErrChk( DAQmxCreateAIVoltageChan( gTaskHandle, data[i].channel, data[i].name,
DAQmx_Val_Cfg_Default, -20, 20, DAQmx_Val_Volts, "" ) ); //set aiadc timing
DAQmxErrChk(DAQmxSetAIADCTimingMode( gTaskHandle, data[i].channel,
DAQmx_Val_HighSpeed));
```

Appendix III

List of rights and permissions

Figure 3 – Permission granted from Rights and permission ELS

Figures 4, 5, 6, 7, 8, 10, 11, 12, 14 – Permission granted from RightsLink

Figures 9, 13 - Open access